LAMINAR SWEPT AND CROSS SHOCKWAVE/BOUNDARY-LAYER INTERACTIONS

by

JISS JACOB SEBASTIAN

DISSERTATION

Presented to the Faculty of the Graduate School of

The University of Texas at Arlington in Partial Fulfillment

of the Requirements

for the Degree of

DOCTOR OF PHILOSOPHY

THE UNIVERSITY OF TEXAS AT ARLINGTON

August 2021

Doctoral Dissertation Committee

Frank K. Lu, Ph.D.

Professor

Department of Mechanical and Aerospace Engineering

Committee Chairman

Brian H. Dennis, Ph.D.

Professor

Department of Mechanical and Aerospace Engineering

Committee Member

Guojun G. Liao, Ph.D.

Professor

Department of Mathematics

Committee Member

Donald R. Wilson, Ph.D.

Professor

Department of Mechanical and Aerospace Engineering

Committee Member

Liwei Zhang, Ph.D.

Assistant Professor

Department of Mechanical and Aerospace Engineering

Committee Member

To my parents,

who have raised me to be the person I am today.

ACKNOWLEDGEMENTS

First, I would like to thank my esteemed supervisor, Dr. Frank Lu, for his invaluable supervision, continuous support, and patience during the course of my doctoral studies. I learned significantly from him and was always fascinated to listen to his life experiences. His immense knowledge and ample experience have encouraged me in my academic research and daily life. As an advisor, he trusted me and was always there for me.

I am highly indebted to Dr. Brian Dennis, Dr. Guojun Liao, Dr. Donald Wilson, and Dr. Liwei Zhang for their interest in my research and for taking the time to serve on my dissertation committee. Also, I acknowledge the support of Dr. Liwei Zhang for allowing me to use TecPlot® software that really helped me in my research for post-processing the computational results. I would like to extend my sincere thanks to Dr. Luca Maddalena for his insightful comments and suggestions. I would like to thank my graduate advisor, Dr. Kamesh Subbarao, for his guidance and advice during my time at UTA. I would also like to show gratitude to Dr. Dragos Dancila, with whom I worked as a Graduate Teaching Assistant for several semesters.

I thankfully acknowledge the contributions of Mr. David Carter that really helped me during my research at the Aerodynamics Research Center (ARC). Also, I would like to offer my special thanks to Ms. Lanie Gordon, Ms. Ayesha Fatima, and Ms. Wendy Ryan for taking care of all the administrative matters. I would like to express my profound gratitude to the Texas Advanced Computing Center (TACC) for providing access to their high-performance computing facility and Pointwise® for providing the meshing software.

I extend my sincere appreciation to Dr. Abhilash Suryan for encouraging and inspiring me to pursue my Ph.D. degree. I am grateful to all the teachers who taught me during the years I spent in school, first in India and then in the United States. I am also thankful to my colleagues at ARC for their frequent help and support.

Getting through my dissertation required more than academic support, and I have many, many people to thank for listening to and, at times, having to tolerate me over the past four years. I am forever grateful to my aunt Ms. Tessy J Kanayinkal, for being supportive to me all the time, emotionally and financially. Her belief in me and the constant motivation helped me a lot throughout my journey. Additionally, I am thankful to her family for their support that has made my study and life in the USA a wonderful time.

To my friends and roommates, thank you for listening, offering me advice, and supporting me through this entire process. Special thanks go to Mr. Sandeep Eldho James and Dr. Jees Augustine–thank you for your friendship and the time we spent together. My appreciation also goes out to my relatives for their encouragement all through my studies. I would like to offer my special thanks to Sr. Celine MMS, Ms. Babitha Joseph and her family, Mr. Ani Abraham and his family, and Ms. Bijitha Joseph and her family.

Finally, I am grateful to God Almighty and my family. I would like to express my gratitude to my parents Ms. Lillykutty Sebastian and Mr. P M Sebastian, for their sacrifice, understanding, encouragement, and patience. This journey would not have been possible without their support. Thanks to my brother Mr. Jais M Sebastian, and his wife, Ms. Iyrin Tom, for their unwavering support.

July 21, 2021

ABSTRACT

LAMINAR SWEPT AND CROSS SHOCKWAVE/BOUNDARY-LAYER INTERACTIONS

Jiss Jacob Sebastian, Ph.D.

The University of Texas at Arlington, 2021

Supervising Professor: Frank K. Lu

Shockwave/boundary-layer interactions are considered one of the most complex problems in high-speed gas dynamics, and numerous studies have been carried out for more than eighty years to understand the fundamental physics. A numerical study was performed using fin-plate configurations to study the three-dimensional swept and cross shockwave/ laminar boundary-layer interactions. All the interactions studied were strong enough for the boundary layer to separate. In the first part, swept shock interactions between a laminar boundary layer and the shockwave induced by a sharp fin mounted perpendicularly on a flat plate were studied. Different flow conditions were investigated at freestream Mach numbers of 2.64, 2.95, 3.44, and 3.93, and the fin angles of 10, 13, 16, and 19 deg. Surface flow features pertinent to fin-induced interactions such as the upstream influence, separation, and attachment lines were identified, and the presence of multiple flow separations in the interaction region was studied. Quasiconical symmetry, as previously observed for turbulent interactions, was established in laminar fin-induced interactions from the results of surface topology and surface pressure distribution. Further examination revealed that there is an

inception zone near the fin apex followed by a farfield zone that appears to radiate from a virtual conical origin, bounded by the flow features and the inviscid shock trace. A new upstream-influence scaling law was proposed for laminar interactions that is different from turbulent ones and verified for a combination of M_∞, α_f, and Re_δ. An extension of two-dimensional free interaction theory was developed and confirmed in three-dimensional laminar fin-induced shockwave/boundary-layer interactions. Next, the separated flowfield associated with a crossing shockwave/laminar boundary-layer interactions at Mach 4 was studied. The crossing shocks were generated by a pair of symmetric, opposing fins placed on a flat plate at 7, 9, 11 and 13 deg angle of attack. The separated flowfield was found to constitute a pair of open separated counter-rotating vortical structures moving downstream. The large extent of the upstream influence in laminar interactions resulted in the deviation from quasiconical symmetry observed in single fin-induced interactions due to the relative narrow gap between the fins. The flow structures were qualitatively compared with the turbulent crossing shock interaction studies to identify and discuss the separated flow regimes. The spanwise surface pressure distributions were studied at different streamwise locations to interpret the nature of the separated flowfield and various topological features identified.

NOMENCLATURE

A	Attachment
a	Power of Re_δ in the Dolling–Settles–Bogdonoff scaling law (see Eq. (4.6))
b	Power of Re_δ in the Dolling–Settles–Bogdonoff scaling law (see Eq. (4.7))
BL	Separated boundary layer
C	Chapman–Rubesin parameter
CFD	Computational fluid dynamics
CFL	Courant–Friedrich–Lewis (CFL) condition
CS	Centerplane separated region
CV	Centerline vortical structure
EF	Entrainment flow
e	Relative error in solution between grids
F	Universal correlation function
FVM	Finite volume method
g	flow property considered for grid independence study
GCI	Grid convergence index
GIS	Grid independence study
K_β	Similarity parameter used in the scaling of upstream influence
k	Thermal conductivity
L	Length of the flat plate
l	Length measured from virtual conical origin
M	Mach number
N	Node

P	Order of convergence in GIS
p	Pressure
R	Radius
Re	Reynolds number
r	Grid refinement ratio
S	Separation
SBLI	Shockwave/boundary-layer interaction
SEF	Side entrainment flow
SP	Saddle point
SS	Secondary separated vortical structure
T	Temperature
TML	Throat middle line
t	Time
U	Upstream influence
u_ϕ	Velocity along β direction
$\mathbf{u}$	Velocity
VI	Vortex interaction
(x, y, z)	Cartesian coordinate system
$\bar{x}$	$\frac{x - x_U}{x_S - x_U}$, normalized length used in free interaction theory
VCO	Virtual conical origin
α	Leading-edge angle
β	Angle made by surface flow features with respect to the incoming freestream direction
β_0	Angle made by the inviscid shockwave trace on the flat plate surface with respect to the incoming freestream direction

$\bar{\beta}$	$\frac{\beta - \beta_U}{\beta_S - \beta_U}$, normalized β used in free interaction theory
β^*	$\frac{\beta - \beta_0}{\beta_U - \beta_0}$, normalized β used in plotting surface pressure distribution
$\bar{\chi}$	Viscous-interaction similarity parameter
δ	Undisturbed boundary-layer thickness at fin apex
δ^*	Undisturbed boundary-layer displacement thickness at fin apex
μ	Dynamic viscosity
ϕ	Angle between the velocity u_ϕ and incoming freestream direction
ρ	Density
τ	Shear stress
(ξ, ζ)	Shockwave-based coordinate system

Subscripts

A	Attachment
c	Converging section
e	Boundary-layer edge
f	Fin
i	Incipient
N	Node
$plat$	Plateau
r	Ramp
S	Separation
U	Upstream influence
v	Virtual conical origin
w	Wall
0	Stagnation conditions
$1, 2, 3$	Primary, secondary, tertiary

∞ Incoming freestream conditions

Superscripts

$\hat{(\,)}$ scaled coordinates according to upstream-influence scaling law (see Eqs. (4.6) and (4.7))

$\tilde{(\,)}$ scaled coordinates according to upstream-influence scaling law (see Eqs. (4.2) and (4.3))

TABLE OF CONTENTS

LIST OF ILLUSTRATIONS

LIST OF TABLES

CHAPTER 1

INTRODUCTION

1.1 Shockwave/Boundary-Layer Interactions

The interaction between shockwaves and boundary layers is a class of viscous–inviscid interactions in high-speed flows. It is one of the most confounding subjects in gas dynamics because of the complex physics involved and its adverse effects on high-speed aerospace vehicles. In a two-dimensional flow, mutual interaction of the shockwave impinging on the boundary layer where viscous effects are dominant modifies the step pressure rise in the inviscid freestream to an adverse pressure gradient. The adverse pressure gradient may be strong enough to result in boundary-layer separation, leading to significant changes in the associated flowfield [8, 9, 10]. The drastic flowfield distortion by boundary-layer separation was observed by Ferri [8] in wind-tunnel tests. Oswatitsch and Wieghardt [11] showed in detail the occurrence of a shockwave/boundary-layer interaction (SBLI) at supersonic speeds and the local increase in pressure and the corresponding thickening of the boundary layer. This phenomenon will be discussed in detail in the later sections. Shockwaves and boundary layers can be found in almost every practical supersonic flow, and thus SBLIs are critical in designing high-speed vehicles. There are many locations on a high-speed aircraft where SBLIs can occur as shown in Fig. 1.1 [1]. Such locations include the intersection of two surfaces, such as compression corners in supersonic inlets and wing–fuselage junctions.

Shockwave/boundary-layer interactions tend to have adverse consequences, particularly when the interaction results in boundary-layer separation. Separated flows

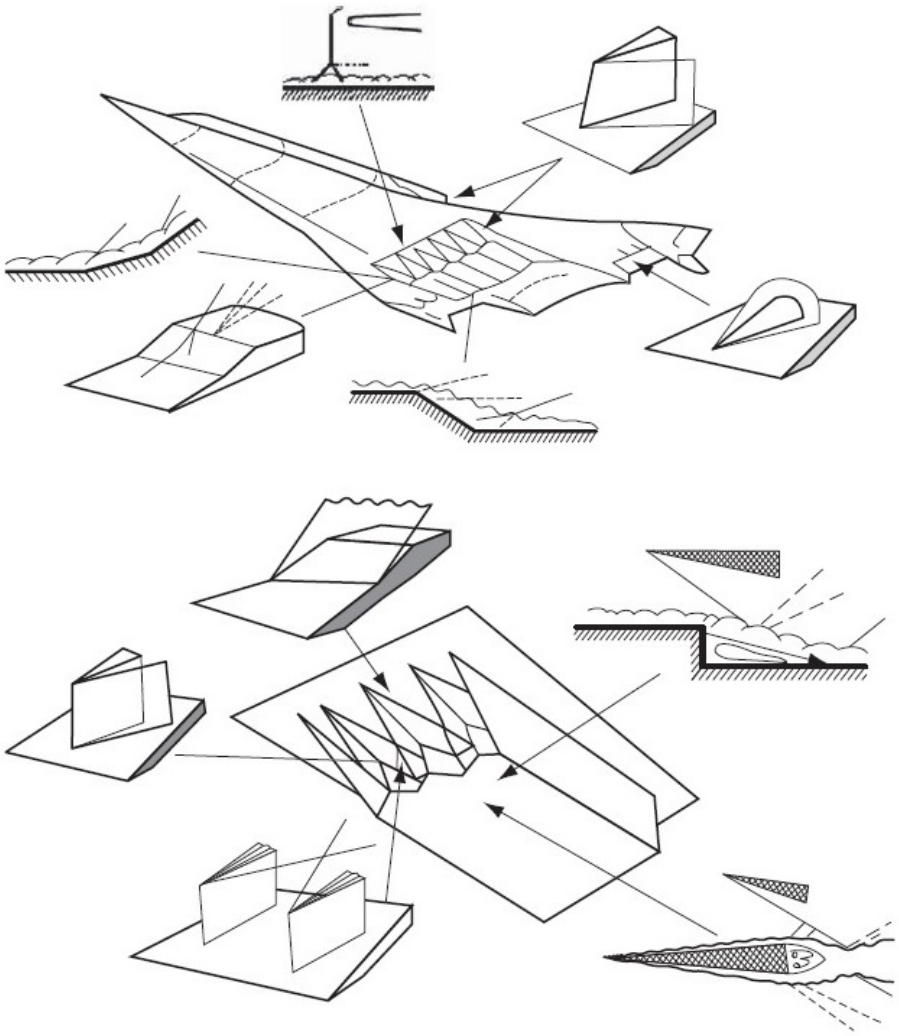

Figure 1.1: Locations where SBLIs can be found in the vicinity of a high-speed vehicle [1]

degrade the aerodynamic performance of high-speed vehicles due to increased drag and heating [12] such as in hypersonic flight. Further, they can lead to unsteadiness resulting in adverse structural response [13], a particularly pertinent example being shock-induced trailing edge separation in transonic flight. These types of interactions continue to demand practical mitigation methods.

Instead of studying interactions on practical shapes, fundamental studies focus on simple, building-block interactions to draw physical understanding. These are

conveniently classified as either two-dimensional or three-dimensional based on the geometry. These simple configurations have been studied extensively. Fundamental interactions in two-dimensional supersonic flows include the flow past a ramp mounted on a flat plate, impinging-reflecting oblique shockwave on a flat plate, a forward-facing step, and a rearward-facing step [7]. Three-dimensional configurations that are characterized by sweep can yield distinctly different boundary-layer separation characteristics from two-dimensional ones.

1.2 Boundary-Layer Separation

Flow separation, or more precisely, boundary-layer separation, is the detachment of a boundary layer from a surface due to a sufficiently adverse pressure gradient. As mentioned earlier, the canonical configurations used for fundamental studies are classified as two- or three-dimensional based on the geometry. Separation induced by a two-dimensional SBLI is typically characterized by a closed recirculation bubble. A ramp-induced SBLI is considered here to understand the flow structure in a two-dimensional separation. A ramp with an angle α_r is mounted on a flat plate as shown in Fig. 1.2. The incoming boundary layer has a thickness δ, and the flow is at a freestream Mach number M_∞.

The flow is deflected at an angle α_r resulting in the formation of an attached oblique shockwave in the absence of viscosity. While a sudden increase in pressure occurs in the inviscid shockwave, the impingement of shockwave with the boundary layer establishes a mutual interaction that yields an adverse pressure gradient [14]. Should the adverse pressure gradient be sufficiently large, the skin friction will vanish at a surface location, leading to a condition known as incipient separation. For the same incoming flow, a small increase in the shock strength will prompt the boundary layer to separate. In the present case, the shock strength exceeds the capacity of the

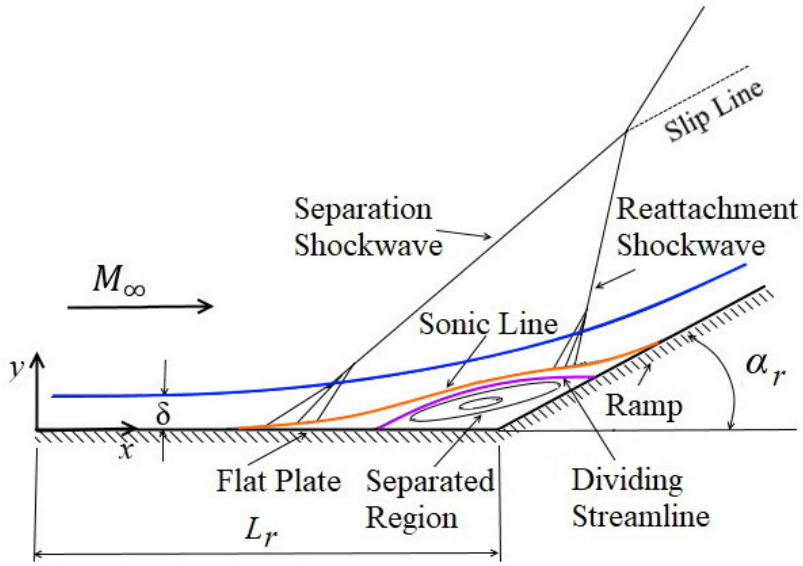

Figure 1.2: Schematic of a ramp-induced shockwave/boundary-layer interaction with flow separation

boundary layer to withstand the compression. This highly localized adverse pressure gradient leads to the separation of the boundary layer upstream of the ramp apex. In such a two-dimensional interaction, this results in a closed separated region near the ramp apex with a slow-moving flow in the reverse direction. A closed separation means that the streamline lifting off at the separation point on the surface reattaches to the rear and encloses the separated region. This concept is relevant as the inviscid flowfield will be distorted because of this separation bubble comparing to the flow that existed before separation. Figure 1.2 shows a separation shockwave formed as a result of the flow deflection due to the separation bubble. The flow is subsonic below the sonic line. The beginning and end of the dividing streamline represent separation and reattachment, respectively. The reattachment of the flow on the ramp causes the formation of a reattachment shockwave, also known as the rear shockwave, which then merges with the separation shockwave, as shown in Fig. 1.2. High pressure and

localized heating can occur at the reattachment location due to the creation of an impinging jet leading to a local flowfield similar to the Edney type IV interaction [15]. The separation shockwave and the reattachment shockwave together form the typical lambda shock pattern. A schematic of the surface pressure distribution normalized by the incoming freestream pressure in the case of a ramp-induced SBLI is shown in Fig. 1.3. The figure shows that the surface pressure starts to rise ahead of the inviscid impingment location. The location where this surface pressure rise occurs is known as the upstream influence L_U which is the subject of great theoretical interest [16, 17].

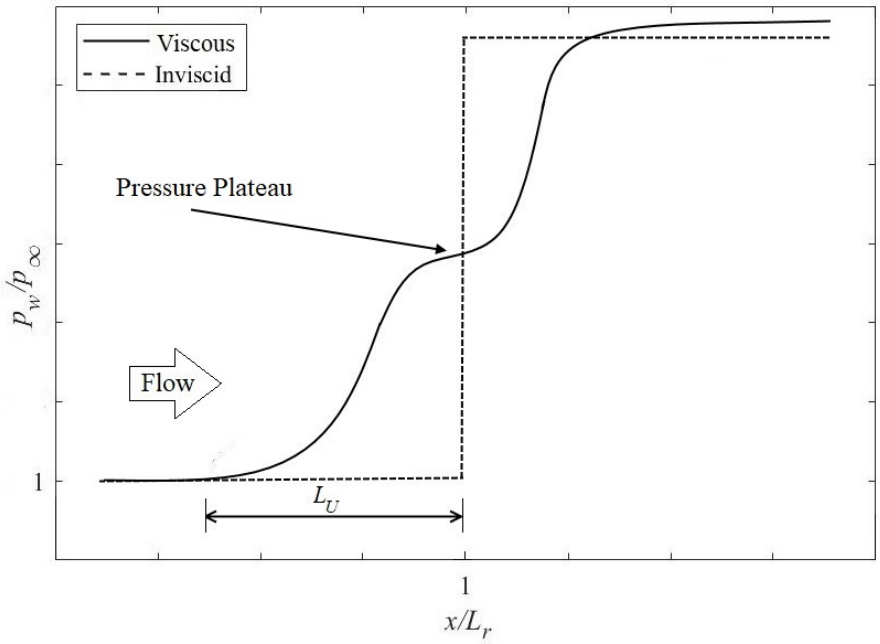

Figure 1.3: Schematic of surface pressure distribution for ramp-induced SBLI

The pressure plot shows a plateau typical of largely separated flows. It is evident from the figure that the pressure rise caused by the shockwave is felt upstream of the theoretical impingement location of the inviscid shockwave on the surface. This

pressure rise is transmitted upstream through the subsonic part of the boundary layer. The onset of interaction, known as the point of upstream influence, is a salient feature of all SBLIs, and L_U denotes the upstream influence length. The thickness of the subsonic layer, which is below the sonic line, depends on the velocity profile at that point. It would be thinner for the turbulent boundary layer because of the fuller velocity profile comparing to the laminar case. Thus, the closer proximity of the sonic line to the flat plate surface in turbulent flows will result in a lesser upstream extent than for laminar interactions.

For two-dimensional separated interactions, Chapman et al. [18] found that the flow evolving towards separation does not depend on the geometry that induced the shockwave for strongly separated flows. In other words, there are no essential differences between the separations caused by an incident shockwave, a normal shockwave, or a ramp, and the boundary layer behaves in the same way to a given rise in pressure independent of the cause in all cases. Instead, the separated region depends on the freestream Mach number, the boundary-layer characteristics ahead of the interaction, and the wall temperature condition. Such flows that are free from the direct influence of downstream geometry are termed "free interactions."

Most flows of practical interest are three-dimensional. Three-dimensional separated interactions are, in fact, rich in topological features [19] compared to two-dimensional ones. In reality, two-dimensional interactions are confined mostly to axisymmetric flows [20]. A transverse pressure gradient occurs in three-dimensional boundary layer and would impart a transverse velocity to the flow. The slow-moving fluid close to the surface will be deflected more than the fluid further away because of this transverse pressure gradient and gives rise to crossflows [21]. When the distance from the surface tends to zero, the streamlines parallel the skin-friction lines and are called "limiting streamlines." The concept of limiting streamlines was introduced by

Sears [22] while studying the laminar boundary layer on an infinite yawed cylinder. Brown [23] proposed that the convergence of limiting streamlines can identify the line of separation in three-dimensional studies. Moreover, the line of attachment is where the limiting streamlines diverge. However, Legendre [24] found that the limiting streamlines considerably increase their distance normal to the surface close to the line of separation. Lighthill [25] considered skin-friction lines instead of limiting streamlines to form the desired continuous vector field for topological analysis. Thus, the lines of separation and attachment can be confirmed by the convergence and divergence of skin-friction lines, respectively [19].

It is already discussed that two-dimensional separation is generally characterized by a closed recirculation bubble. However, three-dimensional separated interactions can either be a bubble type or a free-shear layer type [26]. A bubble-type separation appears similar to a two-dimensional closed separation. Nevertheless, in the latter type of separation, the flow accumulating at the line of separation leaves the surface as a free-shear layer and rolls up to form a vortical structure moving downstream. Instead, a different stream surface attaches. The flow in such an "open separated region" is fast [27], in contrast to a closed separation.

Most of the studies in three-dimensional interactions involve building-block configurations that are characterized by sweep. Such configurations can yield distinctly different boundary-layer separation characteristics. An example of such a configuration is a compression corner with a small sweep angle to the incoming flow, mounted on a flat plate. When the sweep angle is zero, the configuration corresponds to a two-dimensional interaction. By progressively increasing the sweep angle from zero, the flowfield develops from a quasi-two-dimensional to a highly-swept three-dimensional one.

Another example that is of interest in the present research is a sharp, unswept fin placed perpendicularly on a flat plate at a given distance from the leading edge, as shown in Fig. 1.4. An oblique shockwave is generated by the fin with leading-edge angle α_f and interacts with the flat plate boundary layer. The details shown in Fig. 1.4 will be discussed later in Chapter 3.

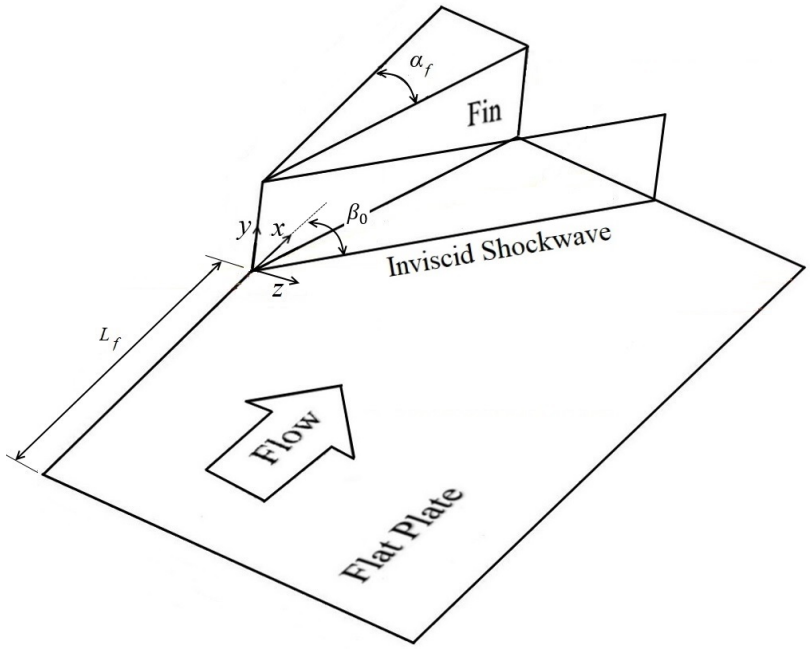

Figure 1.4: An example of a three-dimensional configuration in which a single fin is mounted on a flat plate

The fin-generated oblique shockwave interacts with the flat plate boundary layer, and the pressure rise causes a disturbed flow pattern. When the shock strength is sufficiently large to cause a separation, the flow topology alters significantly, leading to an open separation. The transition from closed to open separation occurs in certain three-dimensional configurations but apparently does not occur in fin-induced interactions. It was mentioned earlier that in two-dimensional studies, the disturbance due to the adverse pressure gradient is first detected at the point of upstream

influence. More conveniently, in three-dimensional swept interactions, upstream influence is identified from the surface topology by the beginning of flow deflection as they approach the fin and is termed as the line of upstream influence. Detailed studies of interactions generated by a swept ramp showed that detecting the upstream influence in the aforementioned manner is equivalent to locating the rise in the surface pressure distribution [28]. The upstream influence was the source of theoretical difficulties which was successfully addressed by Lighthill [16, 17]. The line of primary separation is in the downstream of the line of upstream influence and the line of primary attachment is close to the fin. The terminology includes "primary" because for even stronger interactions, additional separations and attachments develop within the primary separated region. A schematic of fin-induced shockwave/boundary layer interaction in which a secondary separation region is imbedded within the primary separation region is shown in Fig. 1.5.

The surface flow features in the separated region can be extrapolated to a point upstream of the fin apex, termed as the virtual conical origin (VCO) [29]. This quasiconical interaction region can be conveniently split into an inception zone near the VCO that evolves into a farfield [30, 31, 32, 33, 34]. The conical symmetry only existed in the farfield as shown in Fig. 1.5. These features can be confirmed by surface pressure distribution in addition to surface flow visualization discussed above. A schematic of the surface pressure distribution normalized by the incoming freestream pressure is shown in Fig. 1.6. The variation was plotted normal to the inviscid shockwave in the farfield of the interaction region against an angle β subtended by the surface flow features with respect to the incoming freestream direction.

The surface pressure starts to rise at upstream influence and reaches a plateau typical of separation. The pressure rises to a maximum at the primary attachment before dropping to a lower value at the fin surface. The dip in pressure and a small

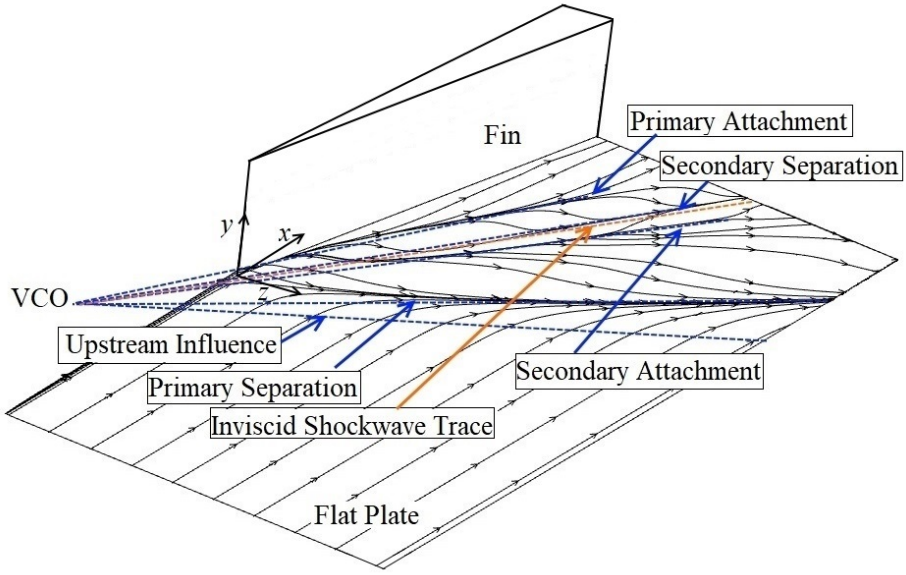

Figure 1.5: Schematic of a fin-induced SBLI and quasiconical similarity

peak detected between the plateau and the maximum are due to the secondary separation and attachment. Quasiconical symmetry will be discussed in more detail in the context of the present research in Chapter 4. Of particular note, free interaction theory that is well established in two-dimensional flows is still unexplored in three-dimensional, swept interactions. It is hypothesized that two-dimensional, free interaction theory can be extended to three-dimensional flows through a suitable transformation. The success of a three-dimensional free interaction theory is important from a theoretical standpoint, similar to its importance in two-dimensional interactions.

Another configuration of interest in the present study is a pair of swept shockwaves of an opposite family crossing a boundary layer. Such configurations are called "double fin configurations" or "crossing shock configurations" (see Fig. 1.7). This

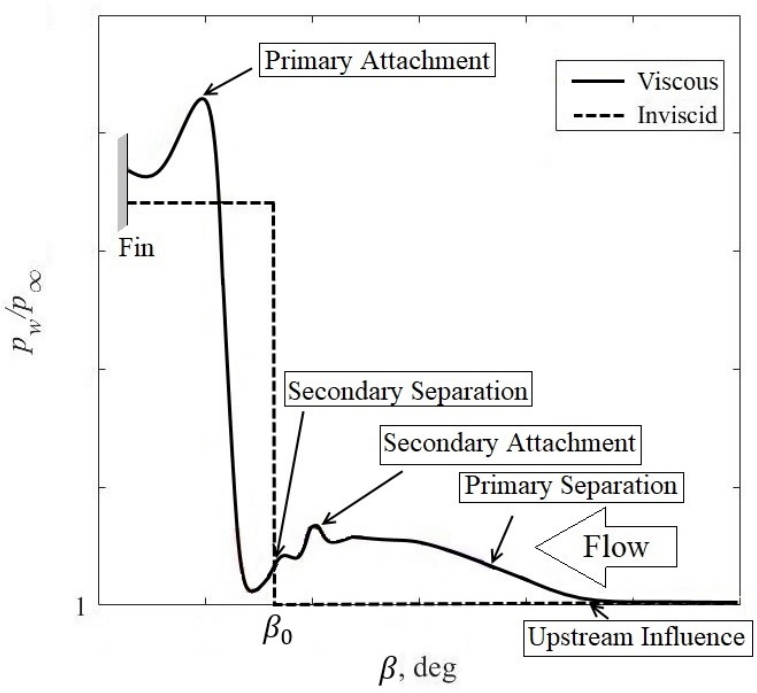

Figure 1.6: Schematic of surface pressure distribution in a fin-induced SBLI

geometry is a natural extension of the single fin mounted on a surface [35]. More discussion on the configuration shown in the figure will be made in Chapter 3. The study of crossing shock interactions is critical as the phenomenon occurs in a variety of situations in aerodynamics and propulsion. Subject to the strength of the shock-waves, a variety of complex interaction phenomena ensue, including flow separation and the generation of vortical structures [36]. An example of where cross SBLI can occur is in high-speed inlets and can lead to large-scale flow separation. Depending on the strength of interaction, the separation might lead to the unstart of inlets. Further, crossing shock configurations are either symmetrical or asymmetrical based on the deflection angle of the fins. The symmetrical configuration involves a pair of fins with the same leading-edge angles mounted on a flat plate as shown in Fig. 1.7. When

the fin leading-edge angles are different, the configuration is asymmetrical. However, the current research focuses on symmetrical crossing shock interactions.

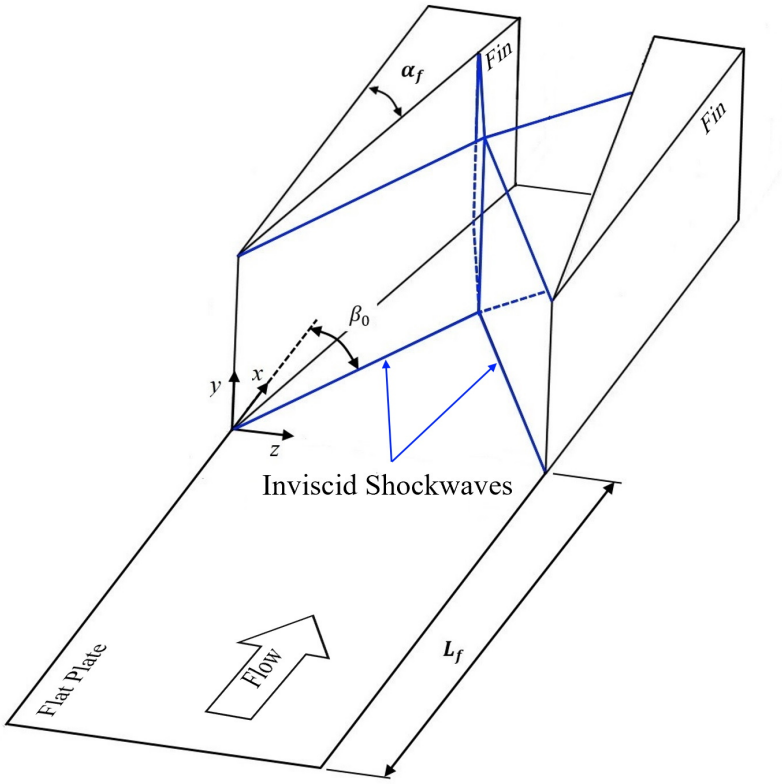

Figure 1.7: An example of a three-dimensional configuration in which a pair of fins are mounted on a flat plate

The oblique shockwaves generated by the opposing fins intersect at the plane of symmetry and interact with the flat plate boundary layer. Experimental and computational studies on the separated turbulent cross SBLIs show that there are certain parameters that can seriously alter the resulting flowfield [35, 37, 38]. These parameters include the freestream Mach and Reynolds numbers, the incoming boundary layer, the fin leading-edge angles, the distance between the fin tips, and the minimum distance between the fins (throat width).

Crossing shockwave/boundary-layer interactions induce open separation depending on the interaction strength. Some of the key flow features of the single fin-induced interactions, namely, the lines of upstream influence and primary separation, are present in cross SBLIs as well and are generated by the individual single fins. The flow accumulating at the lines of separation leaves the surface as a free-shear layer and rolls up to form two primary vortical structures moving downstream as shown in Fig. 1.8. These counter-rotating vortical structures generated by the two fins are considered as the principal feature of cross SBLI flowfield [2, 35, 39, 40].

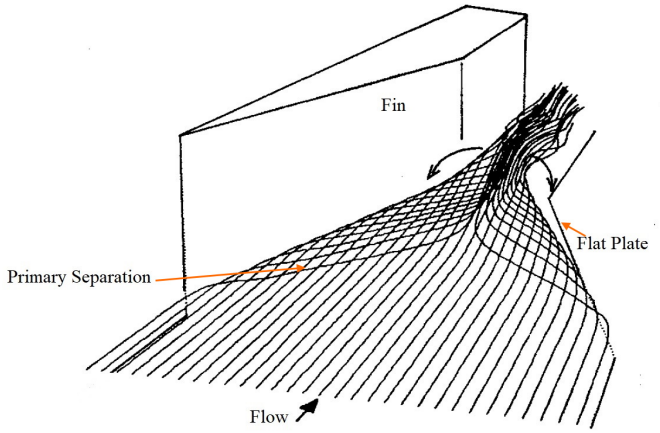

(a) Front view

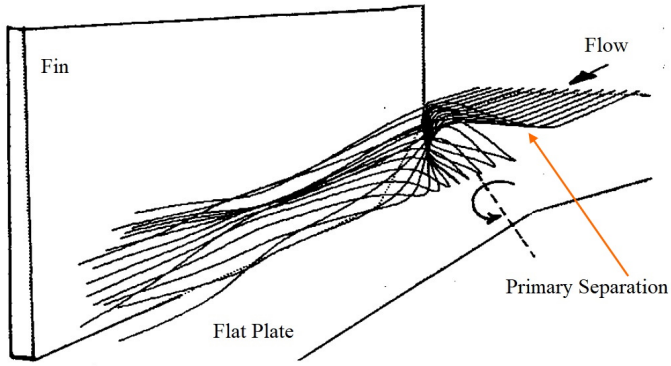

(b) Reverse view

Figure 1.8: Visualization of the vortical structures formed in separated cross shockwave/ turbulent boundary-layer interaction at $M_\infty = 8.3$ and $\alpha_f = 15$ deg (only one of the vortices is shown in the reverse view) [2]

The variation of surface pressure can be used to identify the location of upstream influence where the interaction is first felt. The lines of primary separation are downstream of the upstream influence lines corresponding to each fin. As previously discussed in the case of open separated flows, a different stream surface attaches at the primary attachment lines close to fin surfaces. The fluid structures in such separated interactions exhibit a high degree of complexity, and the physics of the problem has relevance in several applications. The flowfield structure associated with the interaction of symmetric crossing shockwaves and a flat plate laminar boundary layer will be discussed in the context of the present research in Chapter 5.

CHAPTER 2

LITERATURE REVIEW

2.1 Two-Dimensional Shockwave/Boundary-Layer Interactions

Considerable work has been performed in two-dimensional SBLI yielding a good physical understanding. There are five fundamental interactions in two-dimensional flows that can occur between a shockwave and a boundary layer. Such interactions occur in impinging-reflecting oblique shockwaves on a surface, flow past a ramp, a normal shockwave, an imposed pressure jump like at the exit of an over-expanded nozzle, an oblique shockwave induced by a forward-facing step. Basic configurations involving two-dimensional interactions, except the normal shock interaction, are represented schematically in Fig. 2.1 where separation and attachment are denoted by S and A, respectively.

A detailed theoretical explanation of the propagation of a shockwave in a boundary layer and the resulting wave system was given by Henderson [41] for the case of impinging-reflecting oblique shockwaves on a surface. Sturek and Danberg [42, 43] studied turbulent interactions over an isentropic compression ramp and are considered a few among the early experimental works. Detailed surveys of pressure and temperature were performed by them at a nominal Mach number of 3.5.

The structure of the separated region in the supersonic flow past a ramp at different deflection angles was studied by Spaid and Frishett [44]. The study confirmed a double-shock system consisting of separation shockwave and reattachment shockwave for separated interactions. The concept of upstream influence is significant in SBLIs [45] and can be determined from surface pressure distribution and surface flow

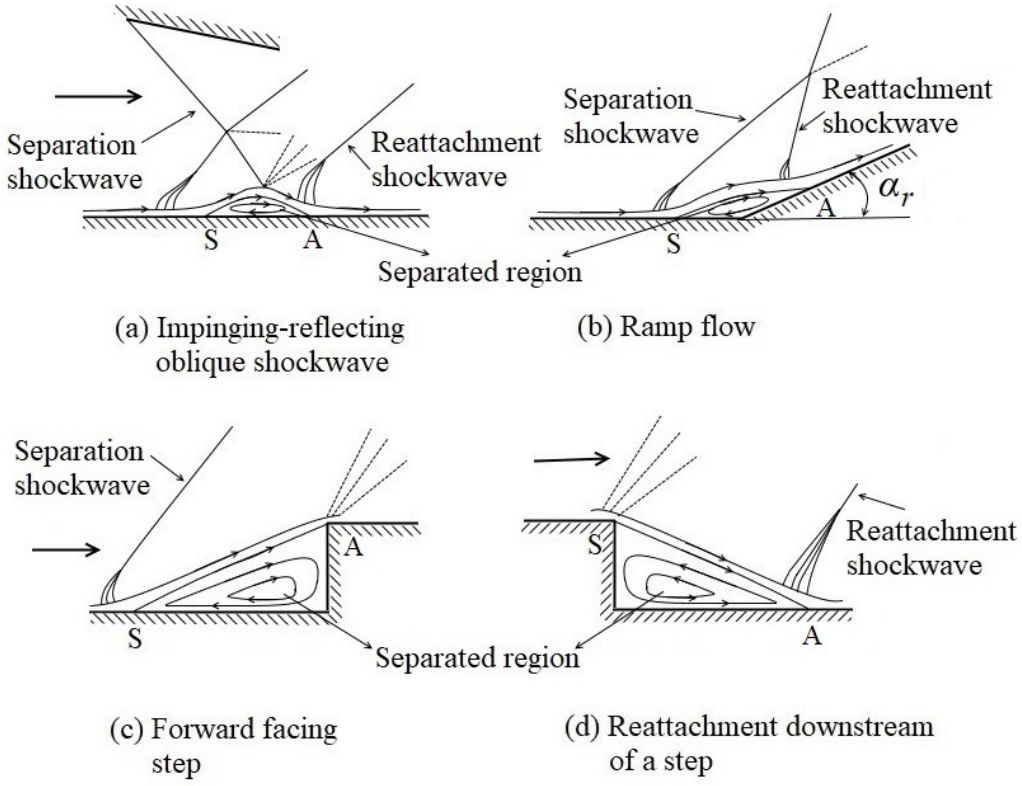

Figure 2.1: Schematic of basic configurations involving two-dimensional SBLI

visualization [27, 46]. Délery and Le Balleur [47] studied the supersonic flow past a forward facing step and the interaction was characterized by the existence of a large recirculation bubble. The size of this separation bubble was found to be roughly proportional to the height of the step. An investigation of the supersonic reattachment downstream of a step was done by Délery [48] and the schematic of flow structure is shown in Fig. 2.1. The supersonic laminar boundary-layer separation through a free interaction was first studied by Stewartson and Williams [49] and Neiland [50] separately. Comprehensive reviews by Délery and Marvin [7], Adamson and Messiter [14], Hankey and Holden [51] and Délery [52] covered a wide range of fundamental two-dimensional SBLI studies.

2.2 Three-Dimensional Shockwave/Boundary-Layer Interactions

Two-dimensional separated SBLIs are insufficient to achieve a proper understanding of the complex topology of three-dimensional separated flows and to explain the physics involved. Studies have enhanced the understanding of three-dimensional separation by focusing on fundamental geometries based on the shape of the shockwave generator [53, 54]. A key geometrical parameter is the sweep that can yield distinctly different boundary-layer separation characteristics. Examples of such building-block, three-dimensional configurations are sharp unswept and swept fins, semi cones, swept compression ramps, blunt fins, and double sharp unswept fins (crossing shockwaves configuration). A few of these configurations are shown in Fig. 2.2.

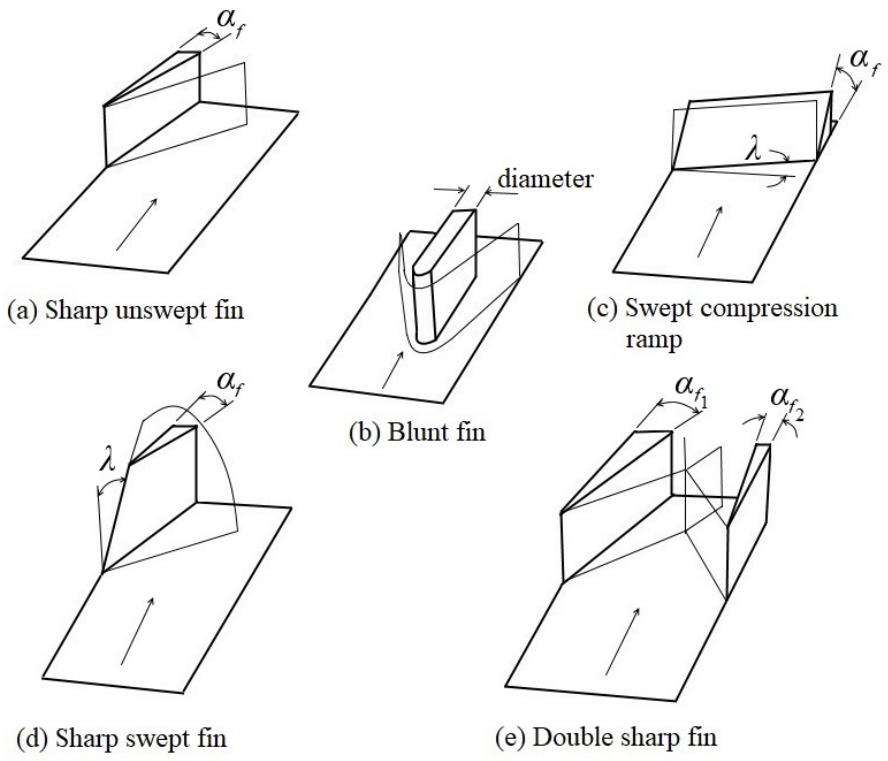

Figure 2.2: Schematic of basic swept shockwave generator configurations

Settles and Dolling [53] classified three-dimensional interactions into two categories: semi-infinite and non-semi infinite interactions. The interactions are called semi-infinite when the shockwave generator has an overall size sufficiently large compared to the boundary-layer thickness such that any further increase in size does not change the interaction flowfield [53]. Furthermore, the category of semi-infinite interactions is subdivided as dimensional and dimensionless depending on the effect of geometry. When shockwave generators impose no length scale on the interactions, they are called dimensionless interactions [53]. Sharp fin-induced interactions exhibit features common to dimensionless interactions. An example of dimensional interaction is that induced by a blunt fin whose nose diameter influences the flowfield. Dolling [55] performed a comparison between sharp- and blunt-fin induced interactions. He found that sufficiently far from a blunt fin, the interaction generated by the blunt fin-induced shockwave appears to be similar to that induced by a sharp fin at the same deflection angle. Comprehensive reviews of fundamental three-dimensional SBLI studies can be found in Délery and Marvin [7], Gaitonde [13], and Panaras [21].

2.3 Sharp Unswept Fin-Induced Shockwave/Boundary-Layer Interactions

A simple shockwave generator configuration that generates a three-dimensional interaction is a sharp unswept fin mounted perpendicularly on a flat plate at an angle to the incoming freestream direction. A schematic of this configuration is shown in Fig. 1.4. This configuration exhibits a semi-infinite dimensionless interaction [27] and is extensively studied because of its practical importance, being a simplified rendition of a wing/fuselage junction for example. Early experimental observations revealed that such interactions are quasiconical in nature [30]. Fundamental studies focused more on turbulent interactions. Hence, in this section, the laminar boundary layer interactions will be reviewed only after a brief discussion on turbulent interactions.

Gadd [56] performed an experiment on fin-induced unseparated interactions at an incoming freestream Mach number $M_\infty = 1.4$ and examined the surface pressure distributions far from the fin apex. The pressure data from Gadd's experiment collapsed well and showed that the pressure distributions are radiating from an origin when plotted in conical coordinates. The better collapse of data confirms the interaction to be conically symmetric. Another useful technique to study conical symmetry is surface flow visualization, as briefly reviewed in Chapter 1.

Another early experimental study was performed by McCabe [57] at $M_\infty = 1.96$ and 2.94. Fin-induced shockwaves for different fin angles $\alpha_f = 2.5$–20 deg interacted with turbulent boundary layers. McCabe found that incipient separation occurs at $\alpha_f = 8.5$ and 5.5 deg for $M_\infty = 1.96$ and 2.94 respectively. He was the first investigator to apply the concept of a separation line as an envelope of surface streamlines in such interactions. Korkegi [58] also studied incipient separation in three-dimensional interactions and found that for $M_\infty > 1.6$, the fin angle at which incipient separation occurs is given by the correlation based on McCabe's data

$$\alpha_i = \frac{0.364}{M_\infty} \text{ radians} \tag{2.1}$$

A better agreement with experimental results was obtained by empirically adding vorticity to the interaction yielding

$$\alpha_i = \frac{0.3}{M_\infty} \text{ radians} \tag{2.2}$$

The analytical and experimental studies by Lowrie [59] concentrated on weak interactions at $\alpha_f = 4$–8 deg, and the resulting shockwave angles did not vary by more than a few degrees. Later experimental studies by Lu et al. [60] revealed that the shockwave angle β_0 is an important parameter to be considered. Miller and Redeker [61] studied interactions at $M_\infty = 2.9$ and fin angles $\alpha_f = 5.7$ and 13 deg and

visualized the skin-friction lines. They found that the fin-generated interaction has lower separation and plateau pressures and a longer interaction length compared to two-dimensional interactions induced by the same shock strength, although strictly as a dimensionless three-dimensional interaction, the conical interaction length increases with span. The spanwise increase of the interaction was studied by Zubin and Ostapenko [62] who found that the surface features appear to radiate from the fin apex except for the region close to the apex itself. This region close to the apex or, in other words, the non-conical inception zone, is found to be inversely dependent on the Reynolds number. The experimental study by Settles and Teng [63] confirmed that the interaction possesses an inception zone followed by a farfield conical region. Later Lu and Settles [32] found that the inception zone is weakly dependent on Mach number but depends strongly on the shock sweep. Also, schlieren photographs revealed a "lambda-foot" shockwave pattern within the separation region. A schematic of the lambda shockwave structure is shown in Fig. 2.3. Such a structure visualized normal to the inviscid shockwave trace is composed of a main shockwave, a separation shockwave, and a rear quasi-normal shockwave. The separation shockwave is formed by the coalescence of compression waves caused by the geometry of the separated region. More discussion on the shock structure in the light of the present research will be made in Chapter 4. Zheltovodov et al. [64] studied the appearance of a secondary separation line in fin-induced interactions. Zheltovodov studied interactions in a wide range of shock strengths and found a correlation for the occurrence of secondary separation.

$$\alpha_{2i} = \frac{0.6}{M_\infty} \text{ radians} \tag{2.3}$$

According to Zheltovodov, the secondary separation line first appears in the farfield region only after the interaction achieves a certain strength.

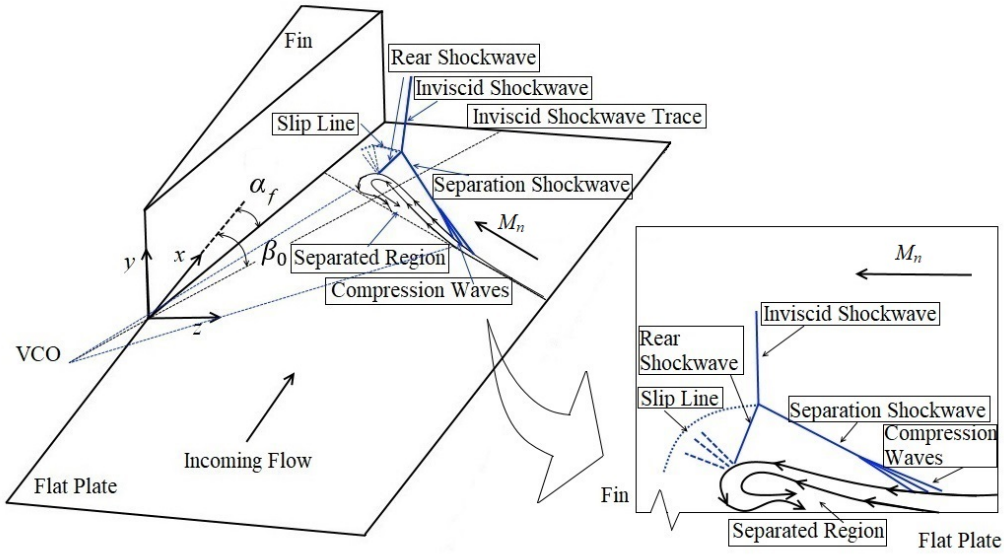

Figure 2.3: Schematic of the shock-structure in fin-induced interactions

Settles and Kimmel [29] introduced the concept of "conical free interaction" by examining the upstream-influence angle, and this concept was reinforced by observing the collapse of surface pressure distributions when plotted against an angle β from the VCO. The study of turbulent fin-generated SBLI by Lu [27] extended the results of Kimmel to a range of Mach numbers of $2.5 < M_\infty < 4$. A normalization procedure was used in [27] to plot a universal surface pressure distribution, which confirmed conical free interaction. All of the surface pressure plots possessed the characteristic plateau and dip typical of largely separated flows [33, 65, 66, 67, 68, 69]. A few other experimental studies on three-dimensional fin-induced interactions include Settles and Lu [30], Kimmel and Bogdonoff [70], Kim and Settles [71], Kubota and Stollery [72], Law [73], and Zheltovodov et al. [74].

The theoretical analysis by Inger [31] reformulated the boundary-layer equations using conical arc-length coordinates centered at the fin apex. He found that shear stress, heat conduction, and velocity and density profiles, in general, do not

exhibit conical symmetry. Further, he confirmed the inception zone's length to be proportional to $\cot \beta_0$, as previously determined by Settles.

Many computational investigations were carried out in the area of fin-induced interactions, mostly involving turbulent boundary layers. Extensive computational studies at $M_\infty = 3$ were performed by Knight et al. [69], Horstman and Hung [75], Horstman [76], and successfully compared the pressure distributions with the experimental results. Horstman and Hung were the first to use the computed streamlines to visualize flow near the line of separation in a turbulent interaction. The computed surface shear-stress distribution showed good agreement with the experimental oil-flow visualization.

Knight [77] studied the turbulent boundary-layer interaction at $M_\infty = 4$ and $\alpha_f = 16$ deg numerically using the three-dimensional compressible Navier-Stokes equations. The computational results showed the characteristic large vortical structure in the separated region of the interaction. Panaras [78] also observed that the separated flow was dominated by a large vortical structure, and the core had a conical shape with a flattened elliptical cross-section. The density contours displayed the lambda-shockwave structure composed of a separation shockwave and a rear quasi-normal shockwave as previously described, Fig. 2.3. The separation shockwave was formed by the coalescence of compression waves caused by the geometry of the separation zone. Knight et al. [79] presented numerical simulations based on the test case of Alvi and Settles [80] and the lambda-shock structure was evident in various contour plots. Panaras and Stanewsky [81] conducted numerical simulations to study the appearance of secondary separation in turbulent interactions. The results showed a secondary separation line. However, the grid used was not fine enough to capture the secondary attachment line.

Most SBLI studies are of turbulent flows due to their practical importance, with few laminar studies. The first investigation of fin-induced laminar interaction was apparently done by Cooper and Hankey [82]. They studied experimentally in a laminar flow at $M_\infty = 12.5$ and $\alpha_f = 15$ deg. Based on surface flow visualizations and surface pressure distributions, they confirmed open separation in fin-induced interactions where the separation streamline is not the same streamline that attaches. Korkegi [83] studied fin-induced interactions in laminar and turbulent flows. The surface flow visualizations obtained by Korkegi were a significant development in understanding the flowfield. At the test conditions considered, secondary reattachment was found to be visible only in laminar interactions. This is because the shock intensities required for separation in turbulent interactions are much larger than laminar ones. In other words, the laminar boundary layers are less able to overcome an adverse pressure gradient, and hence are more susceptible to separation than turbulent boundary layers. Zubin and Ostapenko [62] found that the secondary separation region in laminar interactions is larger than those found in turbulent interactions.

Of specific note are the experimental and computational studies by Degrez [84, 85, 86]. The experimental results at $M_\infty = 2.25$ and fin angles of $\alpha_f = 4$, 6 and 8 deg included surface flow visualizations and surface pressure distributions. The presence of an extended separation was revealed even for the smallest fin angle, in contrast to turbulent boundary-layer interactions. Degrez visualized only the flow upstream of the primary separation, with critical information missing on possible flow separations downstream. Also, the fin angles considered were relatively limited.

The surface pressure distributions showed the rise in pressure at upstream influence followed by plateau pressure corresponding to the separation and a peak pressure at attachment. The schematic of such a distribution was discussed in Chapter 1, see Fig. 1.6. The pressure distributions were found to agree reasonably well with the con-

cept of quasiconical interaction. Another important outcome of Degrez's results was that the upstream pressure distribution depends very little on the fin angle α_f. The computational studies [85, 86] confirmed the quasiconical symmetry of the interaction at $M_\infty = 2.25$ and $\alpha_f = 6$ deg.

In addition to the results discussed so far, the understanding of shockwave structure is critical in fin-induced interactions. Based on the results from the experimental and computational studies performed, Degrez believed that the compression upstream of the inviscid shockwave in laminar interaction is more likely to be spread in a "compression fan" than a separation shockwave. The reason for the claim was that the thickening and separation of laminar boundary layers is a gentler phenomenon than of turbulent interactions. This compression fan's interaction with the inviscid shockwave produces a region of varying entropy instead of a slip line as in a turbulent shockwave structure. Another important finding was that the vortical structure beneath the shock leg is much more elongated than for turbulent interactions because of the greater extent of laminar separation.

2.4 Cross Shockwave/Boundary-Layer Interactions

Three-dimensional crossing shockwave/boundary-layer interactions also form one of the most complex problems of gas dynamics. These interactions are observed both in an external supersonic flow around various elements of high-speed aerial vehicles and in internal flows, for example, in supersonic inlets. Double fin or crossing shock configuration is considered to be a natural extension of the single fin mounted on a surface [35]. The double fin plate configuration shown in Fig. 1.7 consists of two unswept fins with sharp leading edges mounted on a flat plate. Such configurations resemble high-speed inlets and can be classified as symmetrical or asymmetrical based on the fin leading-edge angles. The separated crossing shockwave/boundary-layer in-

teractions can cause an unstart of the inlet depending on the interaction strength [87]. A large number of experimental and computational studies have been carried out on these configurations. As for single fin interactions, the majority of such investigations involved turbulent boundary layers. Hence, a brief review of laminar crossing shock interactions will be made in this section after discussing the advancements in turbulent interactions.

Mee et al. [88] conducted one of the first investigations in crossing shockwave/ boundary-layer interactions. The experimental observations at Mach 1.85 concluded that the intersecting oblique shockwaves might be capable of producing a given rise in pressure with less possibility of separation as opposed to a single strong shock. A numerical study of the crossing shock problem was performed by Gaitonde and Knight [89] for weak and unseparated symmetric interactions based on the experimental studies performed by Mee et al. Two configurations with fin leading-edge angles of 4 and 8 deg were studied at $M_\infty = 2.95$. The results included the visualization of surface streamlines and the surface pressure distributions. However, no solid conclusions regarding the flow structure were made.

Subsequently, Batcho et al. [90] studied experimentally the flow past symmetric and asymmetric fin pairs at Mach 3. They visualized the surface flow topology and measured the flat plate surface pressure. Two of these configurations were numerically studied by Narayanswami et al. [39] at fin angles of 9 and 11 deg. The interactions were symmetrical. The computed results showed general agreement with the surface pressure and surface flow patterns obtained experimentally. A subsequent numerical study was carried out by Narayanswami et al. [2] at $M_\infty = 8.3$ for symmetric 15 deg fins. The results revealed two counter-rotating helical vortices formed by the streamlines originating in the upstream boundary layer, see Fig. 1.8. This vortical structure is considered as a principal feature of the crossing shock interactions [35].

A detailed flowfield visualization was performed experimentally by Garrison and Settles [3, 91] using a planar laser scattering (PLS) method on symmetric crossing shock interactions at freestream Mach numbers of $M_\infty = 3$ and 4 for a range of fin leading-edge angles of 7–15 deg. The resulting flowfield structure at $M_\infty = 3$ was found to agree well with the computed results of Narayanswami et al. [39, 92] and quantitative comparisons were carried out in [93, 94]. A three-dimensional perspective view of the flowfield structure was developed by Garrison and Settles on the basis of PLS images and is shown in Fig. 2.4. Schematic images of the interaction structure at $M_\infty = 4$ and $\alpha_f = 15$ deg at some specific cross-sections (I–III) are also shown in the figure. Based on the symmetry, only half of the interaction is shown in the figure. The fin surface is denoted by F. The sharp fin is mounted on the flat plate marked as p, and r represents the reflection plane. The shock structures shown in the figure will be explained using the cross-sections at the specific locations. As discussed previously, a lambda-foot shockwave pattern can be found in the case of single fin-induced interactions. Cross-section I, which is in the upstream of the intersection of the two single fin interactions, represents two separate lambda-foot patterns. The separation shockwave is marked as 1, followed by a rear shockwave 2 and the main shockwave 3. The slip line is shown as 4 in the cross-section, and the separated region denoted by 5 is visible beneath the shock system.

Cross-section II is in the downstream of the intersection of the two separation shockwaves, as shown in Fig. 2.4. It can be seen that the intersecting separation shockwaves result in a Mach reflection connected by a straight shock segment called the Mach stem 7. More discussion on Mach stem can be found in [95]. The reflected portion of the separation shock wave is marked as 6, and a newly formed triple point is denoted as 10. As shown in the figure, the location of cross-section III is downstream of shock intersection. Two additional shock segments (12 and 13) are formed due to

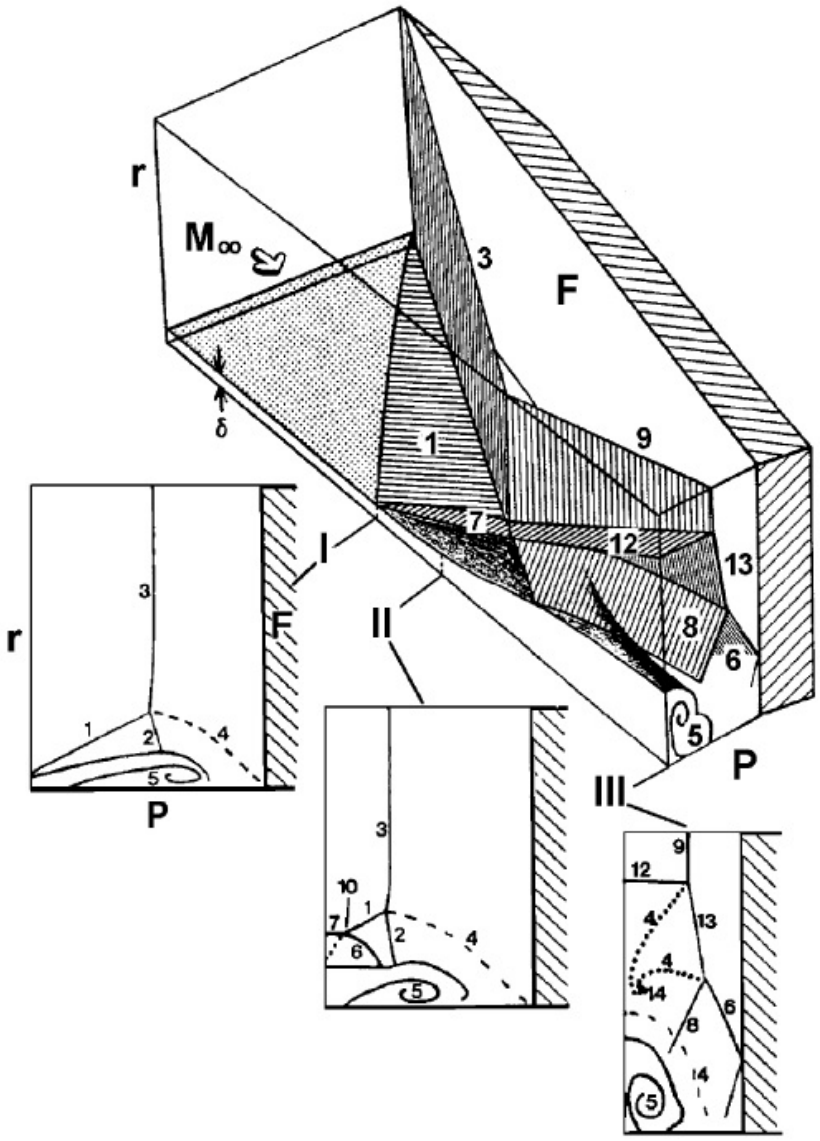

Figure 2.4: Perspective view of the crossing shock flow developed by Garrison and Settles at $M_\infty = 4$ and $\alpha_f = 15$ deg [3]

the crossing shock interaction. A centerline shock segment identified as 12 spans the interaction between the reflected main shockwave (9) and r. The second "bridge" shock segment marked as 13 connects the reflected main shockwave 9 to the reflected separation 6 and rear 8 shockwaves. The separated region 5 is also shown in the figure.

A numerical study of a symmetric double fin-plate configuration with $\alpha_f = 15$ deg was conducted by Gaitonde et al. [4] to study turbulent crossing shock interactions at $M_\infty = 8.3$. They examined the separated flow structure in detail. The computed mean flow structures were identified as "flow regimes" and are shown in Fig. 2.5. These regimes were categorized by Gaitonde et al. as separated boundary layer, vortex interaction, centerline vortices, and entrainment flow. Gaitonde and Shang [37] visualized these flow regimes in turbulent crossing shock interactions using the same 15 deg fin configuration at a different Mach number $M_\infty = 4$. The

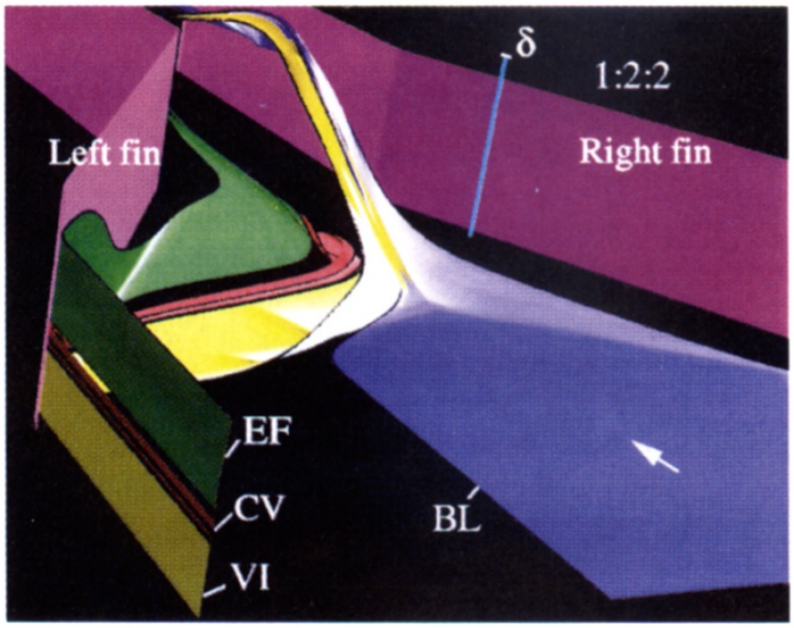

Figure 2.5: Separated flow structure in turbulent crossing shock interactions developed by Gaitonde et al. [4] at $M_\infty = 8.3$ and $\alpha_f = 15$ deg. Stream ribbons are provided to show the separated boundary layer (BL), vortex interaction (VI), centerline vortex (CV), and entrainment flow (EF)

separated boundary layer (marked BL) lifts off from the flat plate surface, as shown in the figure. This regime does not reattach but, instead, forms an open structure with no confined fluid. The region of flow below this separated layer is occupied by

the movement of fluid near the fin leading edge towards the throat centerplane. The flow attaching in the immediate downstream of the separated boundary layer exhibit a vortex interaction (marked VI) on the centerline symmetry plane. The flow from slightly higher locations in the boundary layer near the fin (shown as CV) also moves spanwise to the symmetry plane. The two streams from each fin are subsequently turned in the streamwise direction to form centerline counter-rotating vortical structures. Fluid attaching further downstream forms the entrainment flow (marked EF) and occupies the region below the separated boundary layer and the vortex interaction. This entrainment flow brings high-speed fluid near the wall.

Experiments were conducted by Zheltovodov et al. [38, 96, 97] to study symmetric and asymmetric crossing shock interactions at $M_\infty = 3$ and 3.9. Different combinations were studied using sharp fins with $\alpha_f = 7$, 11 and 15 deg. Asymmetric configurations were considered to extend the study of the evolution of flow regimes with asymmetry. The structure of the limiting streamlines, surface pressure, and heat transfer distributions were obtained and compared with computational results [98]. Further, Zheltovodov et al. [99] studied strong interactions at $M_\infty = 5$ and fin angles 18 and 23. The topological features were examined in great detail, and a systematic comparison of experimental and numerical results was made. A close agreement was observed in weak interaction cases; however, moderate to significant discrepancies were observed in strong interactions in predicting the topological features. In addition, a secondary separated vortex pair was observed experimentally. Numerical studies performed by Schmisseur and Gaitonde [36] at Mach 5 with of symmetric configurations of fins at 18 and 23 deg showed good agreement with experimental surface pressure distributions.

A computational study was performed by Salin et al. [5] at Mach 3.92 on a symmetric configuration with a 15 deg fin angle. They successfully reproduced the

secondary separation phenomenon observed in experiments [99]. The evolution of three-dimensional streamline trace and the four flow regimes in a similar manner as that described by Gaitonde and Shang [37] are shown in Fig. 2.6. The secondary separation is denoted as SS in the figure. Due to the strong adverse pressure gradient

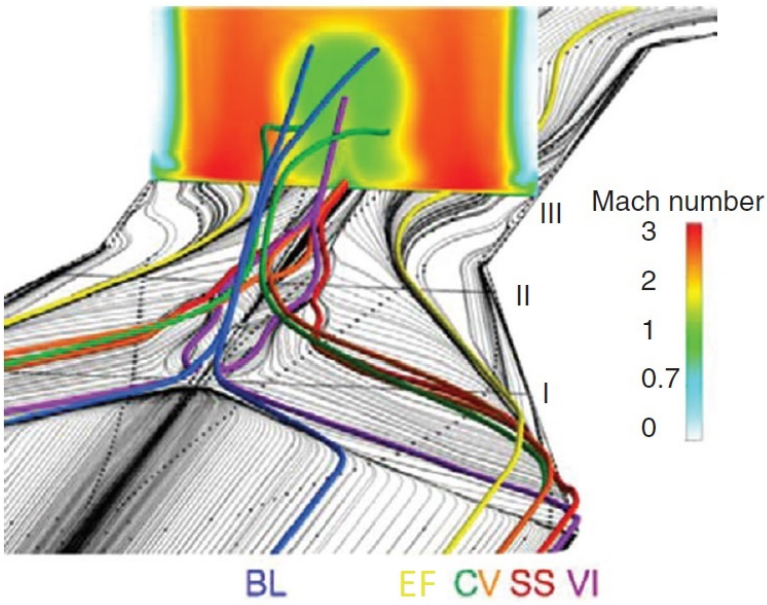

Figure 2.6: Computed flow regimes and streamline trace identified by Salin et al. [5] at $M_\infty = 3.92$ and $\alpha_f = 15$ deg

generated by the crossing shockwaves, the fluid lifts up along the primary separation lines without reattaching to the wall throughout the domain, as previously discussed. The centerline counter-rotating vortex pair (CV) is represented by green and orange colored streamlines. Additionally, the secondary separation (SS) is located below the CV regime, as shown in the figure. Three locations identified as I, II, and III are shown in Fig. 2.6 to compare with the surface flow pattern shown in Fig. 2.7. The lines of separation and attachment were identified by Salin et al. by the convergence and divergence of limiting streamlines, respectively. The experimental oil-flow visu-

alization and the computed surface flow pattern were found to be qualitatively in agreement. Salin et al. used the notations S and R to recognize the separation

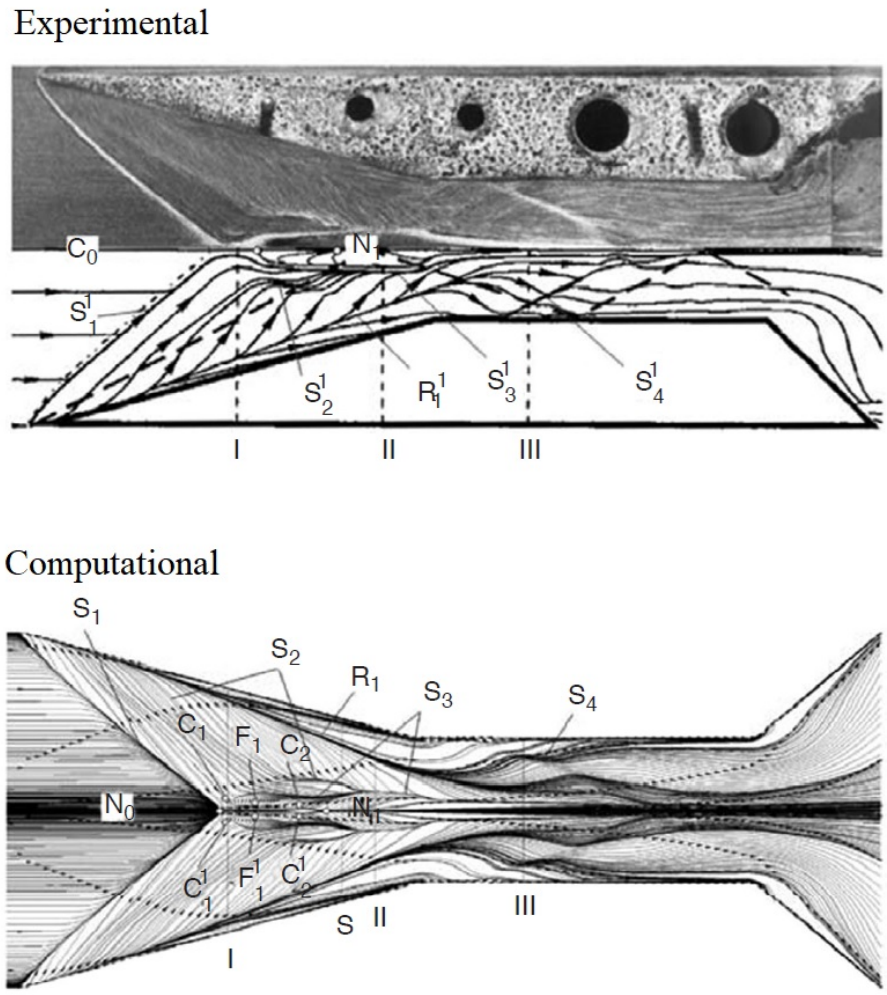

Figure 2.7: Experimental and computational visualization of surface flow patterns at $M_\infty = 3.92$ and $\alpha_f = 15$ deg [5]

and attachment, respectively. Further, singular points such as saddles and nodes are denoted by C and N respectively, as shown in Fig. 2.7. The symmetric counterpart of the flow features in the lower half of the images was identified with a superscript 1, and the flow direction is shown by the arrows. More discussion on the surface flow

visualization will be made in Chapter 5 in the context of the present research. Salin et al. [100] further extended the study to include wall heat transfer prediction at fin angles 7 and 15 deg and $M_\infty = 3.92$.

Quantitative comparisons with experiments were made by Bhagwandin [101] for hypersonic flow at Mach 8.3 involving a symmetric, double-fin configuration with 10 deg fin leading-edge angle. The shock structure between the fins and the separated region was comparable with the experimental flowfield plots. Nonetheless, several attempts have been made in studying crossing shock interactions; a majority of the studies are focused on turbulent boundary layers. A detailed review of the advances in numerical prediction of shockwave/turbulent boundary-layer interactions was made by Knight et al. [102] for symmetric and asymmetric configurations. Zuber et al. [103] conducted experimental and numerical studies on crossing shockwave/laminar boundary-layer interaction at $M_\infty = 6$ using 10 deg sharp fins. They varied the fin thickness to study the effect of throat width or the minimum distance between the fins on the interaction flowfield. The results included surface pressure distribution, experimental oil-flow visualization, computed surface flow visualization, and computed streamlines showing separated structures. The resulting flowfield was found to be primarily composed of the centerline vortex and a separated boundary layer. However, more detailed investigations are required to understand the physics of laminar crossing shock interactions.

2.5 Motivation and Outline of the Present Study

As can be seen from the discussions above, there have been numerous studies of fin-generated swept and cross shockwave/turbulent boundary-layer interactions. Despite the lack of practicality, laminar studies are essential in improving the understanding of the interplay of viscous and inviscid parameters while not involving

themselves with the complications arising from turbulence and turbulence modeling. As Degrez [84] indicated in the case of single fin interactions, laminar studies are useful for weighing the relative importance of viscous and inviscid parameters. Previous studies in laminar interactions are limited, as already discussed. Thus, with these points in mind, the present study was conducted to understand the sharp unswept fin-induced swept and cross shockwave/laminar boundary-layer interactions. A computational study was proposed since most supersonic research facilities operate in the blowdown mode where the high pressure and high Reynolds number typically result in turbulent flows. The quasiconical flowfield resulting from fin-induced swept SBLI will be discussed in detail for different combinations of Mach numbers, Reynolds numbers, and fin leading-edge angles. The separated flow features will be discussed in detail in regard to the flow physics, and a scaling law was developed for upstream influence at different conditions considered. The concept of free interactions is well established in two-dimensional flows but is still unexplored in three-dimensional swept interactions. Since most practical problems are three-dimensional, it is essential to study such interactions that can yield distinctly different separation characteristics. It is hypothesized that the two-dimensional, free interaction theory can be extended to three-dimensional flows through a suitable transformation. Additionally, the study of the underlying physics associated with crossing shockwave/laminar boundary-layer interactions was performed. The configuration of interest is a pair of swept shockwaves of an opposite family crossing a flat plate boundary layer. The study is critical as the phenomenon occurs in a variety of situations in aerodynamics and propulsion. An example of where crossing SBLI can occur is in high-speed inlets and can lead to large-scale flow separation. Depending on the strength of the shockwaves, a variety of complex interaction phenomena ensue. The structure of the current research study is shown as a flowchart in Fig. 2.8. The present study was conducted to

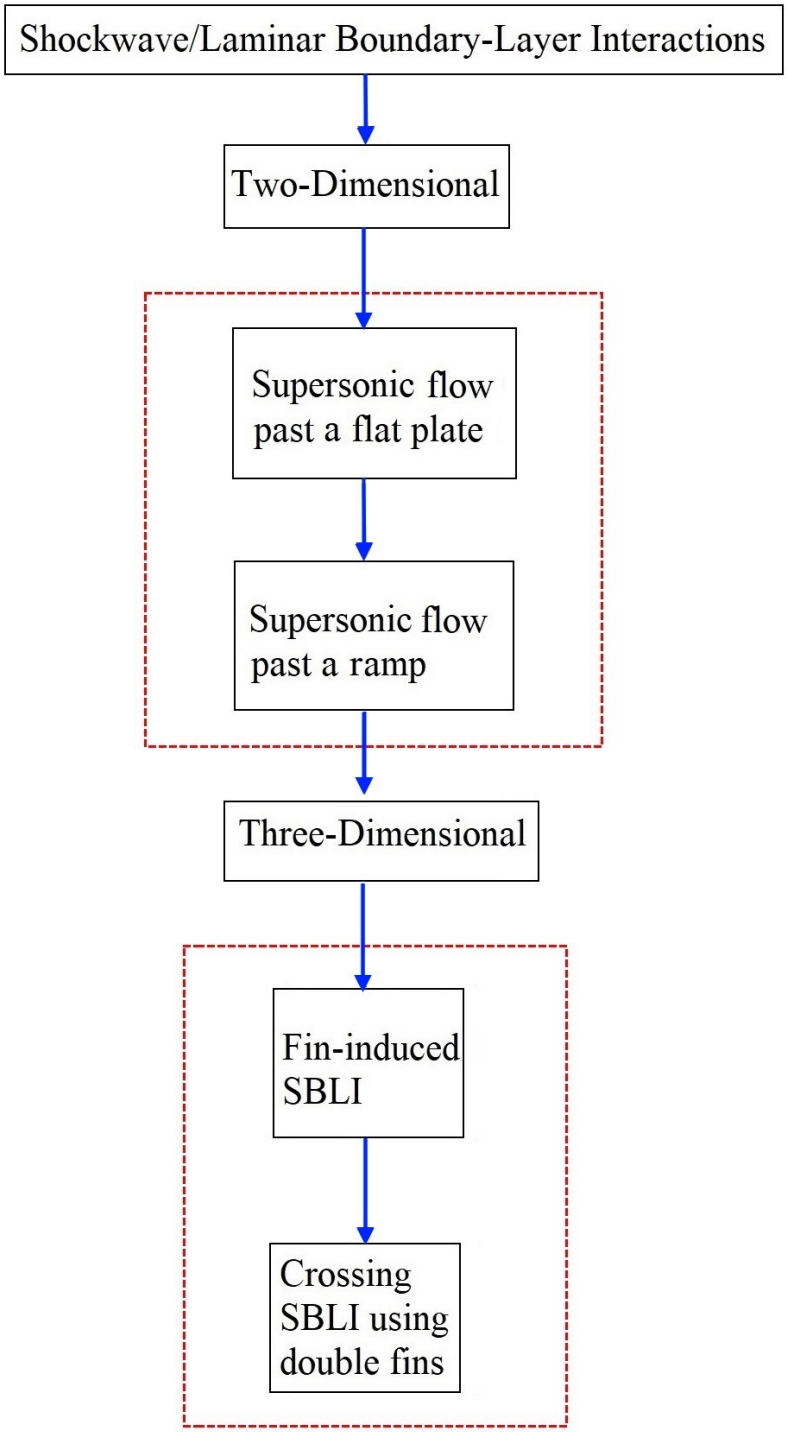

Figure 2.8: Flowchart of the research study

study laminar swept and cross shockwave/ boundary-layer interactions. The computational approach and the discussion on the solver used are provided in Chapter 3. Two-dimensional interactions are considered first, as shown in the structure of the research in Fig. 2.8. Supersonic flow past a flat plate was performed to identify the location where the shock generator can be placed to reduce the effect of viscous–inviscid interactions at the flat plate leading edge. More discussion can be found in Chapter 3. The solver was validated by simulating a supersonic flow past a ramp and comparing the surface pressure variation against the experimental data obtained by Sfeir [104]. Two-dimensional interactions are followed by three-dimensional swept and cross interactions. Chapter 4 consists of the discussion on swept interactions induced by a single fin mounted on a flat plate. A study on the separated flowfield in crossing shock interactions is provided in Chapter 5 using a double fin configuration. The significant contributions of the present work include:

- Study of the quasiconical symmetry in fin-induced shockwave/ laminar boundary-layer interactions.
- Discussion on the multiple separations embedded in the primary separation region.
- An upstream-influence scaling law was developed for laminar fin-induced interactions.
- Extension of the concept of two-dimensional free interaction theory in three-dimensional swept interactions induced by a sharp fin.
- Study of the separated flowfield in laminar crossing shock interactions using surface flow visualization.
- Identification of the separated flow regimes in laminar interactions using streamlines.

CHAPTER 3

COMPUTATIONAL APPROACH

Computational fluid dynamics (CFD) is considered a third approach after the theory and experiment in the study of fluid dynamics. Generally, the numerical solution of partial differential equations is performed in three steps, namely, pre-processing, solution of the discretized system, and post-processing. The pre-processing step involves defining the geometry and generating grids, which will be discussed in detail for the different interactions considered in the present study.

Numerical schemes used in the study of high-speed flows should be capable of capturing discontinuities such as shockwaves. Schemes such as the piecewise parabolic method (PPM) [105], essentially non-oscillatory schemes (ENO) [106], and weighted ENO schemes (WENO) [107] are popular in producing accurate solutions. However, these methods typically involve Riemann solvers that are difficult to implement and computationally expensive [108]. In the present study, the governing, unsteady three-dimensional compressible equations were solved using the open source *rhoCentralFoam*. It is a density-based compressible flow solver in the OpenFOAM® package, based on the central upwind schemes of Kurganov and Tadmor [109], which does not involve Riemann solvers, and hence field-by-field decompositions are avoided. This approach, developed for multi-dimensional systems, is based on *central* schemes proposed by Nessyahu and Tadmor [110] as a second-order generalization of the Lax–Friedrichs scheme. The resulting numerical scheme has been proven to obtain accurate solutions for compressible flow problems [108]. Post processing in the present work in-

cludes the data reduction and visualization and were achieved by using a combination of Paraview®, Tecplot® and MATLAB®.

3.1 Governing Equations

The governing, unsteady three-dimensional compressible equations were solved using the finite volume method (FVM), which will be discussed briefly in this chapter. The continuity equation

$$\frac{\partial \rho}{\partial t} + \nabla \cdot (\mathbf{u}\rho) = 0 \tag{3.1}$$

was solved with the value of velocity $\mathbf{u}$ from the previous time step, thereby providing a new value for density ρ. The momentum equation was solved in two steps [108]. In the first step, the inviscid equation

$$\left(\frac{\partial(\rho\mathbf{u})}{\partial t}\right)_I + \nabla \cdot (\mathbf{u}\rho\mathbf{u}) + \nabla p = 0 \tag{3.2}$$

was solved explicitly for the momentum flux $\rho\mathbf{u}$ which was used to update the value of $\mathbf{u}$ by the known value of ρ. The subscript I stands for the inviscid contribution. In the second step, the diffusion correction equation

$$\left(\frac{\partial(\rho\mathbf{u})}{\partial t}\right)_V - \nabla \cdot (\mu\nabla\mathbf{u}) - \nabla \cdot \left[\mu\left((\nabla\mathbf{u})^T - \frac{2}{3}\mathrm{tr}(\nabla\mathbf{u})\mathbf{I}\right)\right] = 0 \tag{3.3}$$

was solved implicitly for $\mathbf{u}$, where $\mathbf{I}$ is the unit tensor and the subscript V stands for the contribution of viscous effects.

The energy equation was solved in two steps by the flow solver. The inviscid equation was solved first, and a diffusion correction was introduced to solve for the temperature T [108]. In the first step, the total energy density ρE was obtained by solving explicitly the equation

$$\left(\frac{\partial(\rho E)}{\partial t}\right)_I + \nabla \cdot (\mathbf{u}(\rho E + p)) + \nabla \cdot \left[-2\mu\left(\mathbf{D} - \frac{1}{3}\mathrm{tr}(\mathbf{D})\mathbf{I}\right) \cdot \mathbf{u}\right] = 0 \tag{3.4}$$

where the deformation gradient tensor $\mathbf{D} \equiv \frac{1}{2}(\nabla\mathbf{u} + (\nabla\mathbf{u})^T)$. As previously mentioned, the subscript of the time derivative I represents the inviscid contribution. The temperature T was then updated from the total energy density ρE using

$$T = \frac{1}{c_v}\left(\frac{\rho E}{\rho} - \frac{|\mathbf{u}|^2}{2}\right) \tag{3.5}$$

where c_v is the specific heat capacity at constant volume. In the second step, the diffusion correction equation

$$\left(\frac{\partial(\rho c_v T)}{\partial t}\right)_V - \nabla \cdot (k\nabla T) = 0 \tag{3.6}$$

was solved implicitly for T. The time derivative $\left(\frac{\partial}{\partial t}\right)_V$ represents that due to diffusion only. After the temperature was updated, the temperature-dependent quantities, namely, thermal conductivity k and dynamic viscosity μ, were then updated at the new temperature. The pressure p was updated using the equation of state

$$p = \rho R T \tag{3.7}$$

where R is the specific gas constant for air.

Dynamic viscosity was previously calculated using Sutherland's law

$$\mu = \frac{C_1 T^{3/2}}{T + C_2} \tag{3.8}$$

where $C_1 = 1.458 \times 10^{-6}$ Pa/K$^{0.5}$ and $C_2 = 110.4$ K. As is obvious in the above, the governing equations do not consider turbulence.

3.2 Brief Discussion of the Solver

OpenFOAM® is an open-source CFD package that uses the finite volume method for solving fluid dynamics problems. In FVM, the computational domain is divided into cells called control volumes. Figure 3.1 shows adjacent cells connected

by a face. The cell face can be either internal or connected to an external boundary. In the former case, the cell face intersects two cells; in the latter case, the face belongs to a single cell only. In this method, all dependent variables and material properties are stored at each cell center.

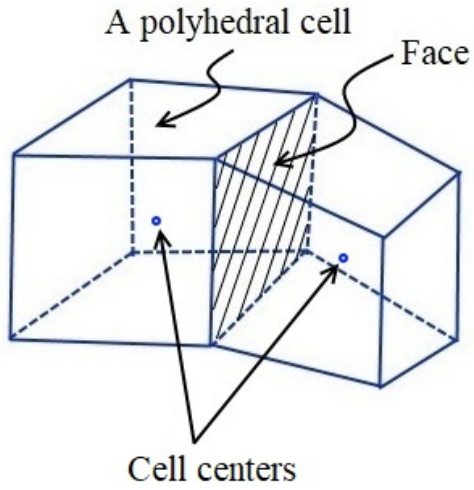

Figure 3.1: Finite volume discretization

The governing equations are integrated over each cell volume. The divergence and gradient terms in the equations are converted to integrals over the cell surface using a generalized form of Gauss's theorem. The next step is the discretization, where surface integration requires the flux values of the primary variables. The values at the cell faces are obtained by interpolating the values at the cell centers connected by that face. The Courant–Friedrich–Lewy (CFL) condition is a numerical constraint determining the time step allowed for a specified grid size. For explicit schemes, the CFL number is less than unity but larger for implicit schemes because these have unconditional stability. The time discretization in the solver determines the

way the solver updates the solution in time. The solver considered in the present study, *rhoCentralFoam*, uses the second-order semi-discrete, non-staggered central differencing interpolation schemes developed by Kurganov and Tadmor [109] and Kurganov et al. [111]. The detailed procedure of discretization and interpolation in *rhoCentralFoam* can be found in [108].

The input files in OpenFOAM are set up with a *case* directory that contains a minimum of three directories 0, *system*, and *constant* [112]. The structure of an OpenFOAM case directory used in the present study with the files contained in the mentioned directories are shown in Fig. 3.2. The initial boundary conditions are

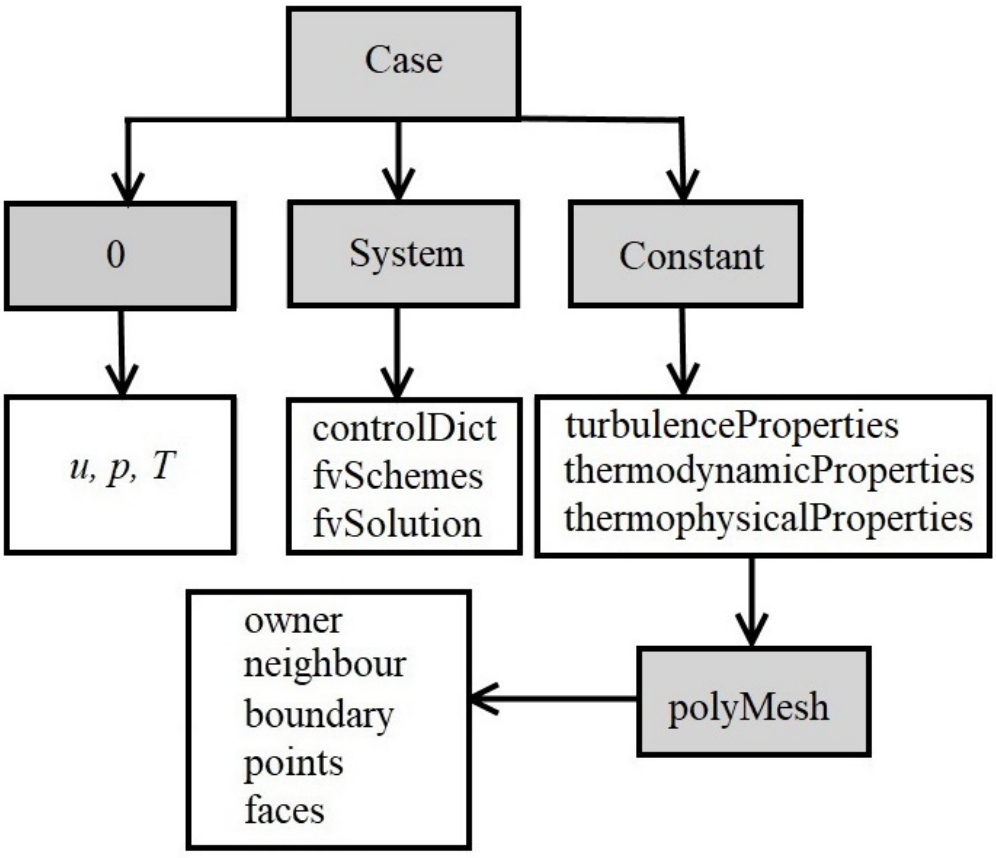

Figure 3.2: OpenFOAM set up files

provided in the 0 directory, where the values of velocity, temperature, and pressure are inputted. The *system* directory contains the specifications for the numerical simulation that includes the settings for the run, discretization schemes, and solution procedures. It consists of three set-up files, as shown in the figure. The values of the time step, run time, and CFL condition are assigned in a *controlDict* file. In the present case, the CFL number is limited to 0.2 to obtain accurate results when solving partial differential equations. Robinet [113] stated that global instabilities generally have low frequencies, which correspond to a time step of $\mathcal{O}(10^{-5})$ s. In the present study, a physical time step of 1×10^{-7} s was used for the simulation, which was deemed acceptable based on Robinet's criterion. The numerical discretization schemes for the different components of the equations are assigned in *fvSchemes*. Temporal discretization is done using a first-order implicit scheme. A second-order Gaussian integration scheme is used for the discretization of gradient and divergence terms. The *fvSolution* file contains the instructions on how to solve each discretized linear equation system and the details of residual control.

The third sub-directory in the *case* directory is *constant*, as shown in the figure. This directory contains the specifications for turbulence and fluid properties. The *turbulenceProperties* file determines the turbulence model used for the simulation. The present study involves laminar flow and, hence, turbulence modeling is not required. The thermophysical and thermodynamic properties are provided in the *constant* directory. A sub-directory *polyMesh*, shown in Fig. 3.2, contains the files of the generated grid, namely, owner, neighbour, boundary, points, and faces. As already discussed, internal faces connect two cells, and boundary faces connect a cell and an external boundary. Each internal face is therefore assigned an 'owner' cell and 'neighbour' cell described by the corresponding labels *owner* and *neighbour*, respectively. In the case of *boundary*, the connected cell is considered as the owner, and the boundary

condition will be specified at the boundary. The files *points*, and *faces* consists of the list of cell vertices, and the cell faces, respectively. In the present study, the grids are generated using Pointwise® V18.2 and exported to *polyMesh* directory. The details of the grid generation and grid independence will be discussed in detail later in this chapter. In CFD, the solution techniques use an iterative process to improve a solution successively. The convergence of an iterative solution is monitored by a residual that measures the relative change of a conserved variable among successive iterations [114]. Residual convergence criteria in the current study were set to 1×10^{-6} for all the variables [115].

3.3 Two-Dimensional Interactions

In the present study, the understanding of two-dimensional interactions is critical to validate the solver used. Numerical simulations are performed to compare with the theoretical and experimental results to confirm that the key flow physics is captured and the resulting data is accurate. The validation of numerical results of the supersonic flow past a flat plate and a ramp is discussed in detail in this section.

3.3.1 Supersonic Flow Past a Flat Plate

It is essential to study flow problems where the boundary layer changes the nature of the outer inviscid flow. Such problems are helpful in understanding the phenomenon of viscous–inviscid interactions. Two of such interactions in high-speed flows are leading edge and shockwave/boundary-layer interactions.

Two regions of leading-edge interactions are shown in Fig. 3.3 where the interaction is strong immediately downstream of the leading edge with a weak interaction region further downstream.

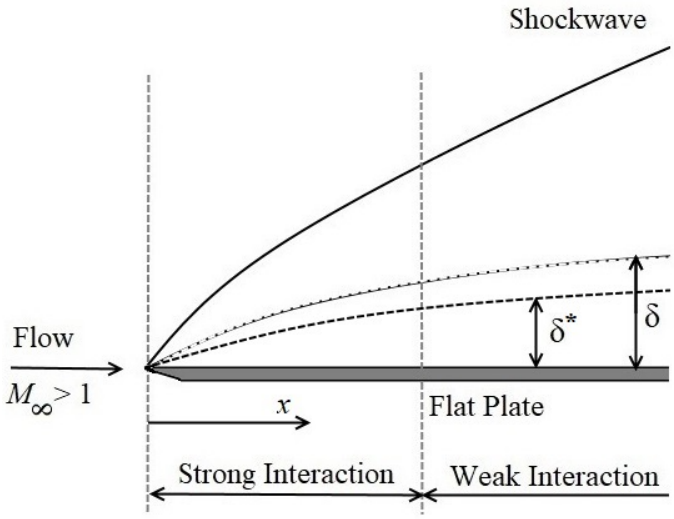

Figure 3.3: Illustration of strong and weak viscous interactions

In the leading-edge region, the growth rate of the displacement thickness of the boundary layer is large. Hence, the incoming freestream flow considers this as an effective body with rapidly growing thickness. A shockwave is generated at the leading edge, and thus the inviscid flow is strongly affected in this region. The changes in inviscid flow, in turn, affect the boundary-layer growth and properties leading to a mutual interaction process. The variation in pressure is a significant consequence of this viscous interaction, and a schematic of the pressure variation in the strong interaction region is shown in Fig. 3.4, invalidating the usual, thin boundary-layer assumption. The pressure along this portion of the surface of the plate is considerably higher than the incoming freestream value.

In the weak interaction further downstream from the flat-plate leading edge, the growth rate of the boundary layer is much reduced so that the outer inviscid flow

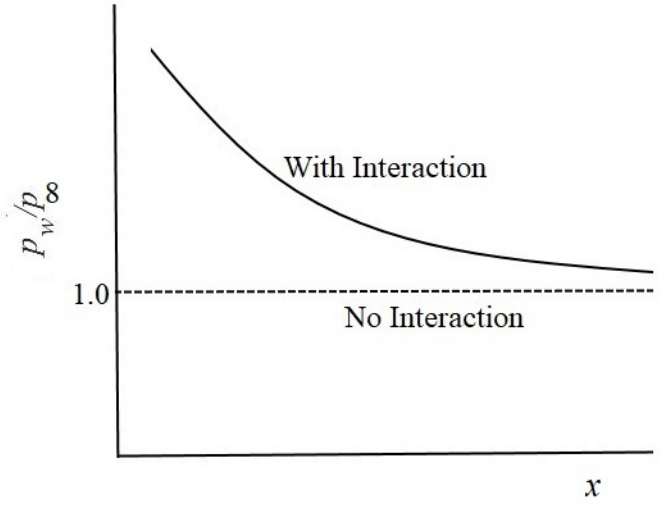

Figure 3.4: Schematic of pressure variation in the strong interaction region

is weakly affected by so-called viscous effects. The similarity parameter governing (laminar) leading-edge viscous interactions is

$$\bar{\chi} \triangleq \frac{M_\infty^3}{\sqrt{Re}}\sqrt{C} \tag{3.9}$$

where the Chapman–Rubesin parameter

$$C = \frac{\rho_w \mu_w}{\rho_e \mu_e} \tag{3.10}$$

The value of the similarity parameter $\bar{\chi}$ can be used to identify whether the interaction region is strong or weak. This type of pressure increment was first reported by Becker [116] by measuring pressures near the leading edge of a wedge. For an insulated flat plate [117, 118], the pressure variation for the strong and the weak interaction is given respectively by

$$\frac{p_w}{p_\infty} = 0.514\bar{\chi} + 0.759 \tag{3.11}$$

$$= 1 + 0.31\bar{\chi} + 0.05\bar{\chi}^2 \tag{3.12}$$

As already discussed in Chapter 2, the objective of the present study is to improve the understanding of fin-induced shockwave/laminar boundary-layer interactions. It is thus critical to determine the location where a shock generator (sharp fin in the present study) can be placed on the flat plate. The incoming flow near the fin apex must be minimally affected by the leading-edge viscous interaction to obtain accurate results. Thus, the study of supersonic flow past a flat plate at the corresponding flow conditions will help determine this location. An example of this study is demonstrated below at an incoming freestream Mach number $M_\infty = 2$, $T_\infty = 100$ K, $L = 4$ m, $Re_L = 3 \times 10^5$ [119]. The surface pressure distribution obtained by numerical simulation was plotted against $\bar{\chi}$ and is shown in Fig. 3.5. The pressure

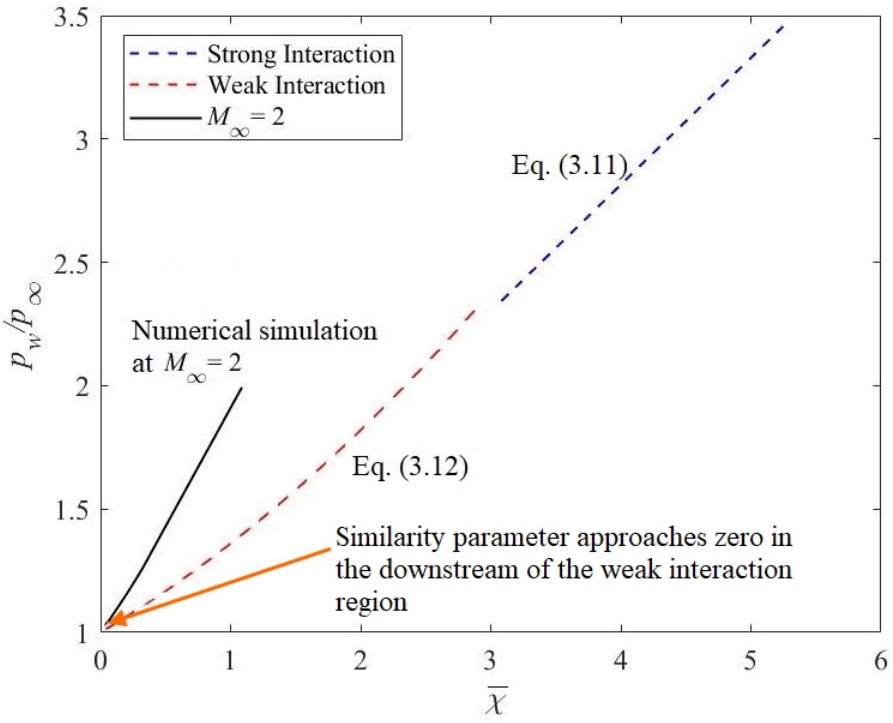

Figure 3.5: Computed surface pressure variation plotted against the similarity parameter $\bar{\chi}$ at $M_\infty = 2$ showing the strong and weak interactions according to Eqs. (3.11) and (3.12)

variation normalized by the incoming freestream pressure was compared against the theoretical results for the strong and weak interaction using Eqs. (3.11) and (3.12). It can be inferred from the plot that the present numerical results do not follow the theory; however, the plot also indicates that the location of the fin apex is sufficiently downstream for the leading edge effects to be minimal. As the value of similarity parameter $\bar{\chi}$ approaches zero, the pressure ratio was found to approach unity downstream of the weak interaction region. More discussion on this topic in the light of the present research will be made later in this chapter.

Another validation is to compare the numerical solution with the analytical Blasius solution subjected to Howarth–Dorodnitsyn compressibility transformation. Howarth [120] developed the theory of compressible flow in a laminar boundary layer by assuming the viscosity to be proportional to the absolute temperature, with the Prandtl number to be unity. The method involves stretching the ordinate normal to the boundary layer using integration as follows:

$$Y = \int_0^y \frac{\rho(y')}{\rho_e} dy' \tag{3.13}$$

The governing equations were then cast in terms of a compressible stream function resulting in the Blasius similarity equation. Thus, the Blasius solution can be defined in the (x, Y) plane. The transformation was inverted to find the compressible solution in the physical (x, y) plane, namely,

$$y = \int_0^Y \frac{\rho_e}{\rho(Y')} dY' \tag{3.14}$$

A detailed information on the transformation can be found in [120]. A MATLAB® code was developed for obtaining laminar boundary layer solutions using the Howarth–Dorodnitsyn transformation. The results of compressibility transformation in terms of the Blasius similarity variable $\eta \triangleq y\sqrt{\frac{U_e}{\nu_e x}}$ at different freestream Mach numbers

for an adiabatic wall is shown in Fig. 3.6. The value of η when u/u_e approaches unity was found to be increasing with Mach number. Hence, it can be understood from the velocity profiles that the boundary-layer thickness increases with increasing Mach number.

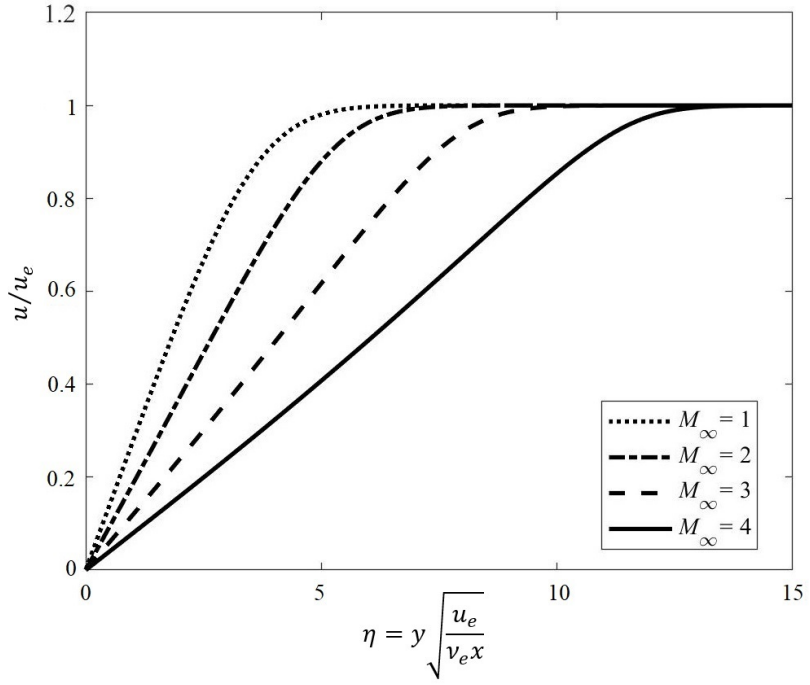

Figure 3.6: Howarth–Dorodnitsyn compressibility transformation results

The velocity profiles from the previously described numerical simulation of supersonic laminar flow past a flat plate were used to compare with the theoretical results. Velocity profiles at different streamwise locations identified by x/L were plotted in terms of the Blasius similarity variable η. These profiles were compared with the theoretical velocity profile as shown in Fig. 3.7 at $M_\infty = 2$. The collapse of the plots is evident from the figure, and it shows that they are indeed self-similar.

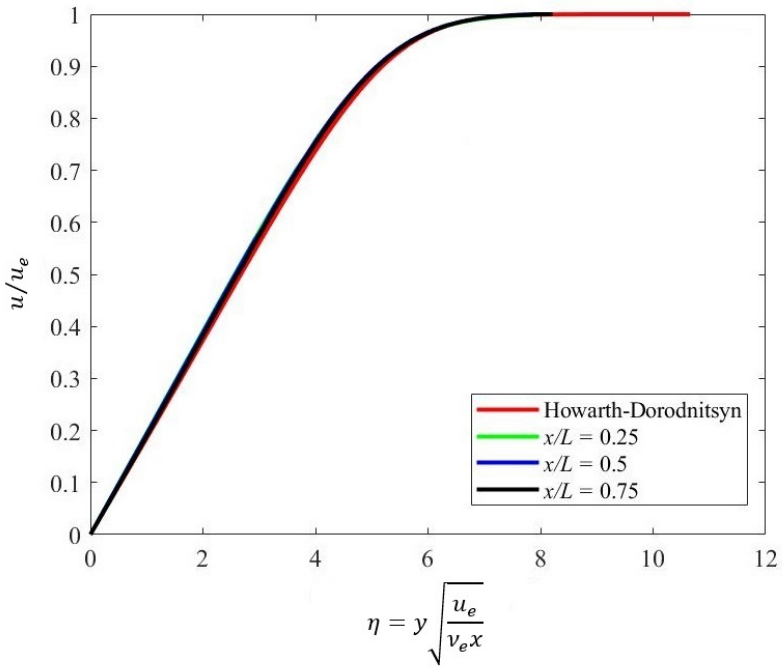

Figure 3.7: Comparison of the transformed Blasius profile and the velocity profiles at different streamwise locations at $M_\infty = 2$

3.3.2 Supersonic Flow Past a Ramp

The flowfield of ramp-induced SBLI was discussed in detail in Chapter 1 in explaining two-dimensional separation. To ensure that the solver can adequately capture the physics of laminar SBLI, a supersonic flow past a compression ramp was simulated numerically for different conditions studied. The incoming freestream conditions were provided at the inlet. In the present numerical simulation, short inviscid wall preceded the "viscous" wall so that the sharp gradients in the flow solution are not close to the inlet boundary.

3.3.2.1 Validation Using Sfeir's Results

The validation of numerical results with the experimental data obtained by Sfeir [104] will be discussed in this section. Flow past a ramp with $\alpha_r = 11$ deg

mounted on a flat plate at a distance of $L_r = 100$ mm from the leading edge was numerically simulated. Boundary conditions were the same as in Sfeir's experimental study at $M_\infty = 2.64$ and $Re_{L_r} = 1.4 \times 10^5$ [104]. A numerical schlieren image obtained from the simulation results revealed the leading-edge shockwave, separation shockwave, reattachment shockwave, and the separated region, as shown in Fig. 3.8. The oblique shockwave generated by the ramp created an adverse pressure gradient

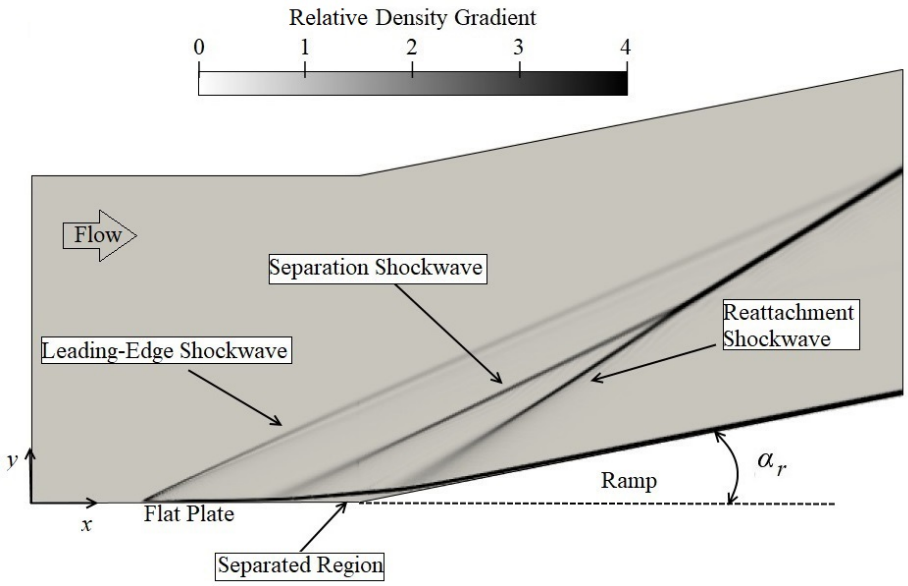

Figure 3.8: Numerical schlieren image of the supersonic flow past a ramp at $M_\infty = 2.64$ and $\alpha_r = 11$ deg

that was strong enough for the boundary layer to separate. The flow separated at the point of separation reattached on the ramp resulting in a closed separation bubble. The separation shockwave and the reattachment shockwave together created the typical lambda shock pattern discussed earlier in the Chapter 1. This lambda-foot shock structure is evident in the numerical schlieren image. Moreover, the extensive compression systems at both the separation and reattachment are clearly seen in

the figure. The streamlines deflect as it pass through the shock structure. Figure 3.9 shows the enlarged image of the separated region for clarity. The deviation of streamlines through the shockwaves is evident in the figure. The separation and reattachment shockwaves are shown using dashed lines.

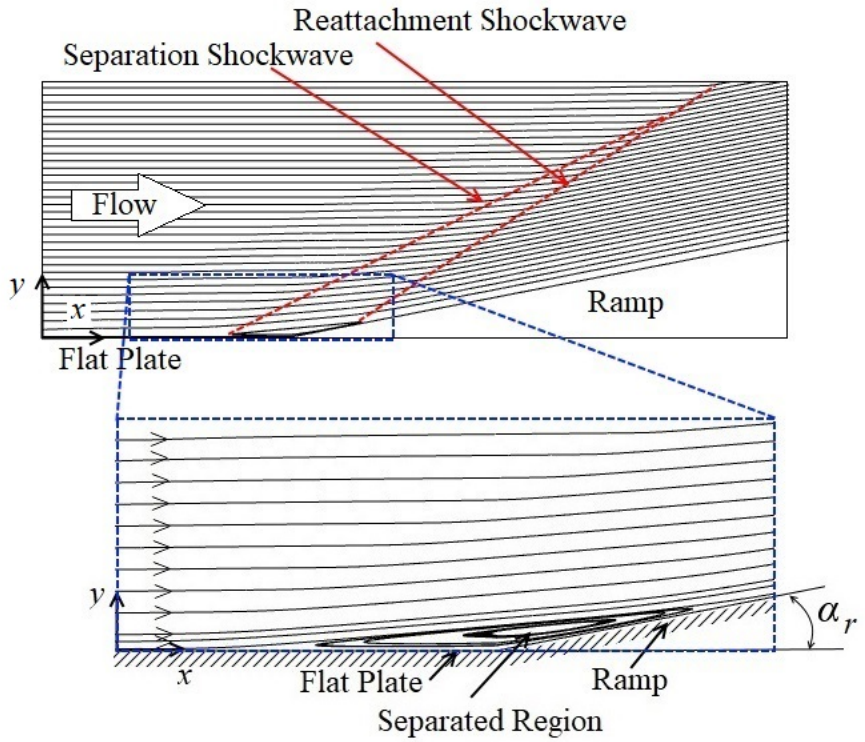

Figure 3.9: Computational results showing the supersonic flow past a ramp at $M_\infty = 2.64$, $\alpha_r = 11$ deg

The surface pressure normalized by the incoming freestream pressure was plotted against the incoming flow direction x, normalized by the length of the flat plate. These pressure variation was compared against experimental results obtained by Sfeir. Here, the flow direction is from left to right as indicated using the arrow in Fig. 3.10. The numerical and experimental data were found to agree reasonably well. A pressure

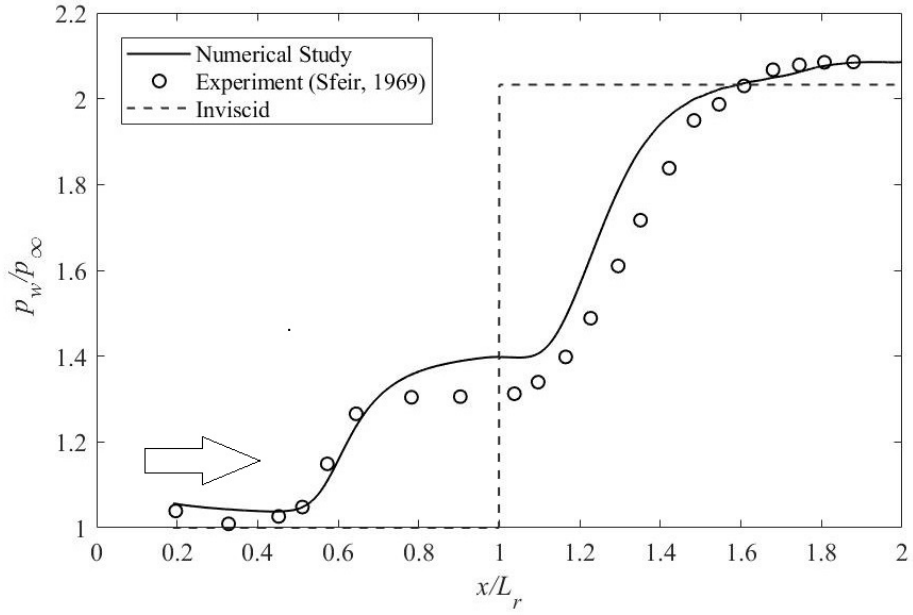

Figure 3.10: Comparison of surface pressure distribution for the supersonic flow past a ramp with the experimental results

plateau was observed in the plot which is an indicator of two-dimensional separation. The surface pressure further increased and reached a peak value at the reattachment location typical of ramp-induced interaction. The inviscid pressure distribution is also plotted in the figure. The surface pressure near the reattachment region is found to be higher than the corresponding inviscid pressure due to the local Edney type IV interaction [15]. It can also be seen that the viscous interaction drastically stretches the extent of the pressure rise from the step inviscid rise.

3.3.2.2 Two-Dimensional Free Interaction Theory

A brief discussion of two-dimensional free interaction theory [18] with some present results is provided in this section as a background to the extension in three-dimensional interactions. A dimensionless function $F(\bar{x})$ from the analysis by Chapman et al. for two-dimensional flows is assumed to be a universal correlation function

independent of M_∞ and Re. This function is expressed in terms of two dimensionless functions $f_1(\bar{x})$ and $f_2(\bar{x})$, namely,

$$F(\bar{x}) = \sqrt{f_1(\bar{x}) f_2(\bar{x})} \tag{3.15}$$

The function $f_1(\bar{x})$ is obtained from simplification of the boundary-layer momentum equation at the wall that gives a relationship between the streamwise pressure gradient and the normal shear-stress gradient,

$$\frac{dp}{dx} = \left(\frac{\partial \tau}{\partial y}\right)_w \tag{3.16}$$

Next, by performing a streamwise integration of Eq. (3.16) from the point of upstream influence and after further simplification yields

$$f_1(\bar{x}) = \int_{\bar{x_U}}^{\bar{x}} \left(\frac{\partial \bar{\tau}}{\partial \bar{y}}\right)_w d\bar{x} \tag{3.17}$$

The normalized length $\bar{x}$ shown in Eq. (3.17) is given by

$$\bar{x} = \frac{x - x_U}{x_S - x_U} \tag{3.18}$$

and the wall shear stress is normalized by the wall shear stress at the upstream influence

$$\bar{\tau} = \frac{\tau_w}{\tau_{w_U}} \tag{3.19}$$

The vertical displacement y is normalized by the displacement thickness δ^* at the interaction onset. The resulting normalized vertical displacement is given by

$$\bar{y} = \frac{y}{\delta^*_U} \tag{3.20}$$

The function

$$f_2(\bar{x}) = \frac{\partial \bar{\delta}^*}{\partial \bar{x}} \tag{3.21}$$

is obtained after introducing normalized quantities that connects the boundary-layer thickening and the pressure variation induced in the outer inviscid flow, namely,

$$\sqrt{M_U^2 - 1}\left(\frac{p - p_U}{2q_U}\right) = \frac{d\delta^*}{dx} \tag{3.22}$$

The universal correlation function $F(\bar{x})$, determined from experiments [7], at separation point is shown in Table 3.1 below. The higher value of $F(\bar{x})$ for turbulent flow shows that laminar boundary layers are more susceptible to separate than turbulent ones. Hence, the distance between the separation point and the upstream influence $(x_S - x_U)$ is larger for laminar interactions. This difference is because the subsonic portion of the laminar boundary layer is thicker than the turbulent ones. The thicker boundary layer allows a longer upstream propagation of the disturbance under an adverse pressure gradient.

Table 3.1: Values of the universal correlation function at separation point [7].

	F
Laminar flow	0.81
Turbulent flow	4.22

It can also be seen from the above summary that the pressure rise at separation depends only on the flow properties at the interaction onset and not on the downstream conditions. The data from the present numerical study for ramp angles of $\alpha_r = 6$, 7, 9 and 11 deg, all at Mach 2.64, are plotted according to Eq. (3.15) and is shown in Fig. 3.11. The excellent agreement of data to the free interaction theory is evident from the plot.

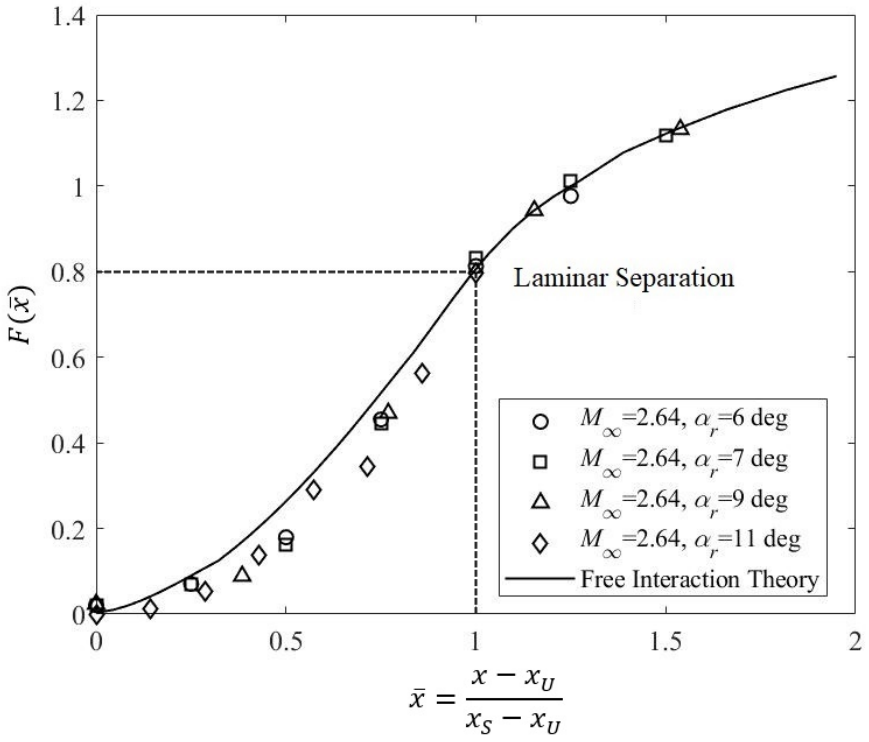

Figure 3.11: Correlation function for the pressure rise during separation for laminar flows

3.4 Three-Dimensional Interactions

The building-block configurations used for studying three-dimensional interactions are characterized by sweep, as already mentioned in Chapter 1. The three-dimensional interactions are rich in topological features [19], and a study of laminar fin-induced interaction can help improve the physical understanding of the flow problem without the complications arising from turbulence and turbulence modeling. The details regarding geometry, boundary conditions, and the computational grids will be included in this section.

3.4.1 Sharp Unswept Fin-Induced Interactions

3.4.1.1 Geometry and Boundary Conditions

The oblique shockwave was generated by an unswept sharp fin mounted perpendicularly on a flat plate with a leading-edge angle α_f as shown in Fig. 3.12. The

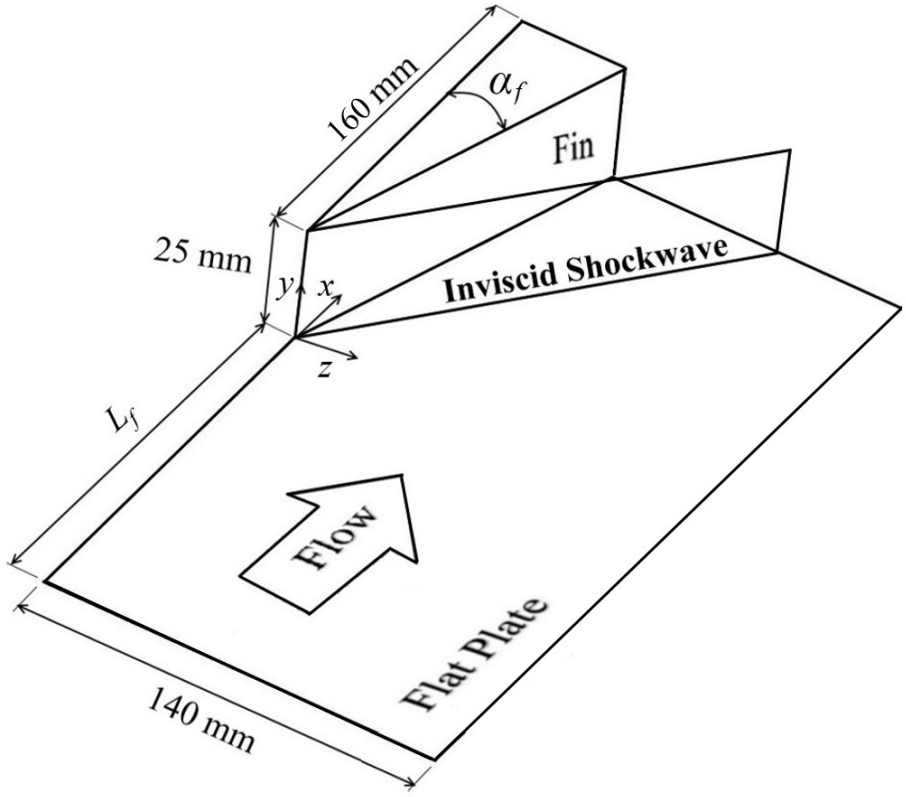

Figure 3.12: Schematic of sharp fin configuration for the present study

shockwave interacts with the flat-plate boundary layer at a freestream Mach number M_∞. Different cases of fin-plate configurations and freestream conditions were studied and are shown in Table 3.2.

The length of flat plate till the fin apex L_f was determined to be minimally affected by the viscous interaction at the leading edge of the flat plate by using the theory of viscous interaction previously discussed. A numerical simulation of the flow

Table 3.2: Different cases considered for the present computational study.

M_∞	α_f (deg)	L_f (mm)	δ (mm)	Re_δ
2.64	19	130	3.5	3053
2.64	16	130	10.4	1009
2.64	16	130	3.5	3053
2.64	16	130	1.2	9084
2.95	16	150	3.9	3658
3.44	16	150	4.2	4599
3.93	16	150	4.5	5643
2.64	13	130	3.5	3053
2.64	10	130	3.5	3053
6.00	10	50	1.3	12361

past a flat plate at $M_\infty = 2.64$ was performed, and the variation of surface pressure was compared against the theoretical results for the strong and weak interaction using Eqs. (3.11) and (3.12). The comparison is shown in Fig. 3.13 where the surface pressure normalized by the incoming freestream pressure is plotted against $\bar{\chi}$. The

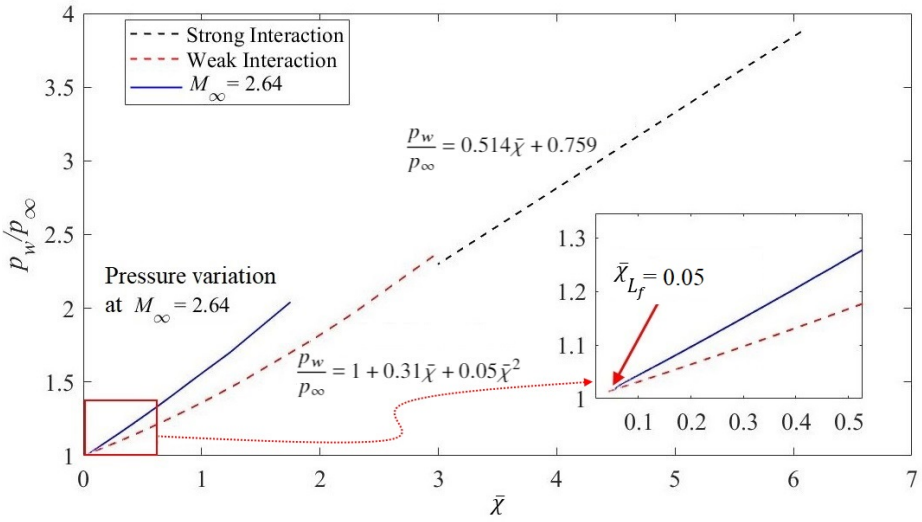

Figure 3.13: Pressure variation due to leading edge viscous–inviscid interaction at $M_\infty = 2.64$ compared with theoretical pressure ratio. Location of $\bar{\chi}_{L_f}$ is also shown.

plot shows that the present numerical results do not follow the theory but nevertheless indicates that the location of the fin apex is sufficiently downstream of the flat plate leading edge. In particular, the location of $\bar{\chi}_{L_f}$ for $M_\infty = 2.64$ is shown in the plot, corresponding to a wall pressure ratio close to unity. The values of L_f and the corresponding values of $\bar{\chi}$ for the different M_∞ considered are shown in Table 3.3. The location L_f for the four Mach numbers was chosen to ensure that the viscous

Table 3.3: Length of the flat plate till the fin apex L_f.

M_∞	L_f (mm)	$\bar{\chi}_{L_f}$
2.64	130	0.05
2.95	150	0.06
3.44	150	0.09
3.93	150	0.12

interaction at the leading edge was negligible at the SBLI location. This is shown by the values of the leading-edge viscous interaction parameter $\bar{\chi}_{L_f} \approx 0$.(see Table 3.3) that places the SBLI in the weak viscous interaction of the flat-plate leading edge. Of particular note is that L_f is 130 mm for Mach 2.64 only and 150 mm otherwise for the other Mach numbers of $M_\infty = 2.95$, 3.44, and 3.93.

The incoming freestream Mach number of $M_\infty = 2.64$ and the corresponding Reynolds number was chosen to match the laminar, two-dimensional, compression ramp study of Sfeir [104]. The stagnation temperature $T_0 = 283$ K and the stagnation pressure $p_0 = 8.9$ kPa. Adiabatic wall and no-slip conditions were assumed for the wall. The values of $M_\infty = 2.95$, 3.44, and 3.93 parallelled those of the turbulent SBLI study by Lu and Settles [121]. The case of $M_\infty = 6$ matched the conditions of the study by Zuber et al. [103] in laminar cross SBLI. The Prandtl number was assumed constant with a value of 0.713. Undisturbed boundary-layer thicknesses at

the fin apex for each Mach number are given in Table 3.2, where the criterion for the boundary-layer edge was $0.995u_e$.

3.4.1.2 Grid Generation and Grid Independence Study

The computational grid for the present study was generated using Pointwise® V18.2. A computational domain was modeled from the geometry shown in Fig. 3.12 and was discretized in the (x, y, z)-directions to generate a three-dimensional structured grid. An assessment of computational and experimental data for SBLIs by DeBonis et al. [122] concluded that the results have apparently no dependence on whether the computational grid was structured or unstructured. Different views of a grid generated for the present study are shown in Fig. 3.14. The grid density was

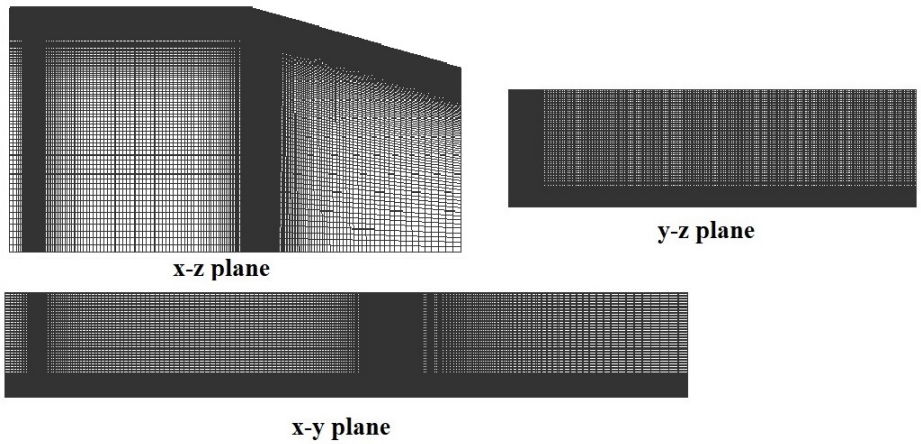

Figure 3.14: Different views of the computational grid generated for $M_\infty = 2.64$ and $\alpha_f = 16$ deg

made higher toward the plate and fin surfaces by applying a cell-to-cell expansion ratio of 1.1 [123] in each coordinate direction to capture the large velocity gradients in the boundary layer. The grid was also made denser at the leading edge of the flat plate to properly resolve the viscous–inviscid interaction at that location.

A grid independence study (GIS) was performed to determine a grid distribution that resolves the flowfield without an excessive number of grid cells that is computationally expensive. An example of the approach is described for $M_\infty = 2.64$ and $\alpha_f = 16$ deg. Starting from the coarse grid with $757,264$ cells, two successively finer grids were then generated by applying a refinement ratio r to the grid spacing in each coordinate direction. The value of r should be greater than 1.1 [124] for grid refinement and in the present study, an arbitrary value of $r = 1.5$ was selected. The number of cells in each grid thus generated is shown in Table 3.4.

Table 3.4: Grids generated for GIS at $M_\infty = 2.64$ and $\alpha_f = 16$ deg.

Grid	$x \times y \times z$	Number of cells
1	$152 \times 53 \times 94$	757,264
2	$230 \times 79 \times 140$	2,543,800
3	$345 \times 118 \times 210$	8,549,100

Following Roache [125], a grid convergence index (GCI) is defined for two successive grids i and $i+1$ where grid $i+1$ is finer than grid i:

$$\mathrm{GCI}_{i,i+1} \equiv \frac{F_s |e_{i,i+1}|}{r^P - 1} \tag{3.23}$$

in which F_s is a safety factor in the range $1.25 < F_s < 3$, $e_{i,i+1}$ is the relative error between two grids and P is the order of grid convergence. As recommended by Roache [124], $F_s = 1.25$ was selected when three or more grids are used for GIS. The relative error in solutions between two grids i and $i+1$ was calculated by

$$e_{i,i+1} = \frac{|g_i - g_{i+1}|}{g_{i+1}} \tag{3.24}$$

where g_i is a flow property obtained for grid i. In the present study, g was the maximum surface pressure along a line normal to the inviscid shockwave and starting

at $x/\delta = 32$ from the fin apex, which was in the farfield region. The values of g_1, g_2 and g_3 were 1311.5, 1319.05 and 1322.6 Pa respectively. The calculated values of $e_{i,i+1}$ for the present study are shown in Table 3.5.

Table 3.5: Relative error and GCI calculated for each refinement step.

Grids	e	GCI (%)
1, 2	5.7×10^{-3}	0.63
2, 3	2.7×10^{-3}	0.29

The order of convergence P is given by

$$P = \ln\left(\frac{g_1 - g_2}{g_2 - g_3}\right) \Big/ \ln r \tag{3.25}$$

In general, the order of convergence in GIS is considered in the behavior of the error in the solution. This error is defined as the difference between the discrete solution f and the exact solution [124, 125]. A second-order solution would have a theoretical order of convergence equal to 2 but the observed order of convergence in the numerical solution would likely be lower due to boundary conditions, numerical models, and the grid [124]. Applying Eq. (3.25) yields the order of convergence to be 1.86 for the present study which is slightly less than 2. The obtained values of GCI for each refinement step are shown in Table 3.5. The GCI was based upon a grid refinement error estimator derived from the theory of generalized Richardson extrapolation [126]. A small value of the GCI is an indication that numerical uncertainty due to the discretization error is negligible. Presented as a percentage, the GCI indicates how much the solution would change with a further refinement of the grid [124].

One of the key requirements for accuracy in discretization error estimation is that the solutions should be in the asymptotic range [127]. When a grid is refined using r, the asymptotic range is defined as the sequence of systematically refined

grids over which the discretization error is reduced. Roache defined the GCI as a scale to evaluate how far the solution is from the asymptotic value [125]. Also, a small value of GCI indicates that the computation is within the asymptotic range and the achievement of asymptotic range is examined by

$$\frac{\mathrm{GCI}_{1,2}}{r^P \times \mathrm{GCI}_{2,3}} \approx 1 \tag{3.26}$$

The calculated GCIs in the present study satisfied Eq. (3.26) with the value of 1.02. Further, the variation of surface pressure on a plane normal to the inviscid shockwave at $x/\delta = 32$ for the different grids considered is shown in Fig. 3.15.

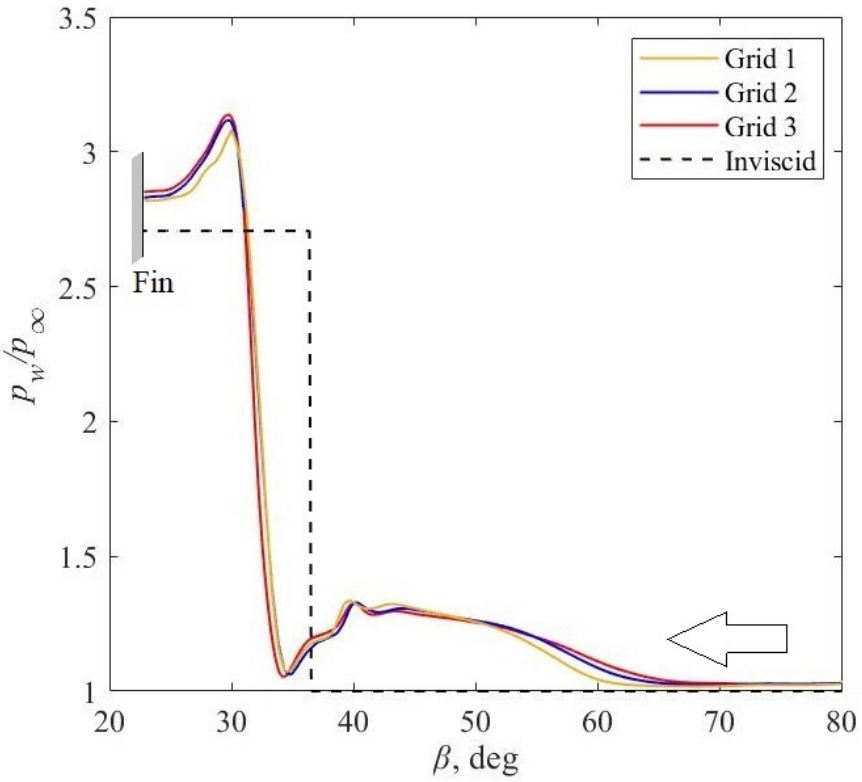

Figure 3.15: Normalized surface pressure for different grids studied at $M_\infty = 2.64$ and $\alpha_f = 16$ deg. The arrow in the figure indicates the direction normal to the inviscid shockwave

The values were normalized by the incoming freestream pressure and were plotted against an angle β made by the surface flow features in the farfield region with respect to the incoming freestream direction. The arrow in the figure indicates the direction normal to the inviscid shockwave. The rise in pressure starting from the upstream-influence angle $\beta_U \approx 65$ deg was due to the generation of compression waves followed by a pressure plateau that is typical of separated interactions and further reached a peak value at the attachment close to the fin. More discussion on the surface pressure variation will be made in Chapter 4. The figure also shows the inviscid pressure distribution.

Grid 2 with 2,543,800 cells was selected for the present study considering the small value of GCI between grids 2 and 3, thus reducing the computational effort. Grid independence was also investigated based on the visualization of surface flowfield using the concept of limiting streamlines. The key flow features pertinent to fin-induced interactions, as discussed in Chapter 1, were visible in all the three grids considered. Interaction flowfield corresponding to each grid studied is shown in Fig. 3.16. A detailed discussion on the flow visualization can be found in Chapter 4.

The minimum and maximum grid spacings in each coordinate direction expressed in terms of the boundary-layer thickness at the fin apex are shown in Table 3.6. The minimum grid spacing is the distance of the first grid point adjacent to the fin or the flat plate, with the maximum grid spacing in the outer (freestream) region.

Table 3.6: Minimum and maximum grid spacing in each coordinate direction.

	$\Delta x/\delta$	$\Delta y/\delta$	$\Delta z/\delta$
Minimum	0.07	0.014	0.07
Maximum	0.3	0.18	0.73

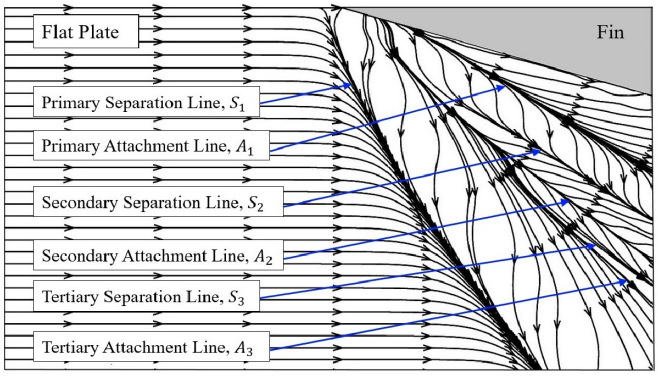

(a) Grid 1

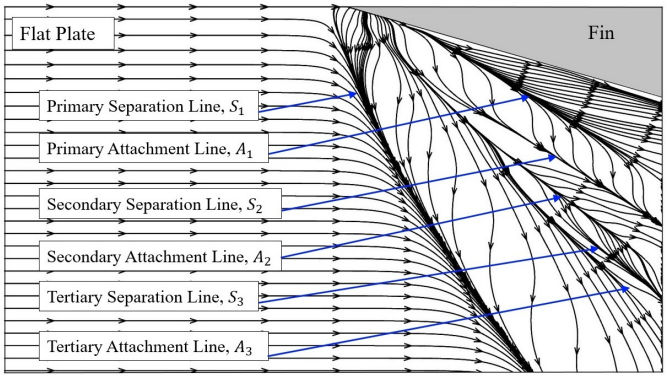

(b) Grid 2

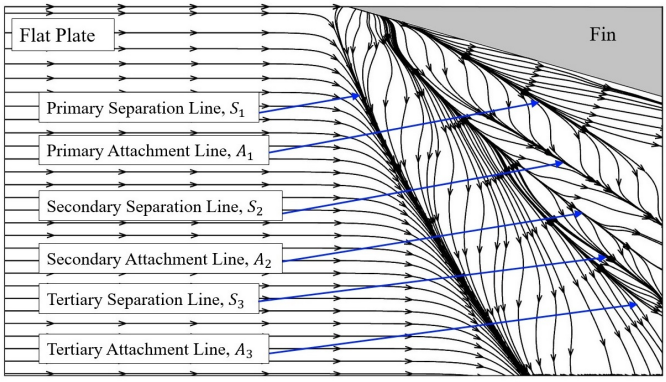

(c) Grid 3

Figure 3.16: Visualization of surface flowfield for different grids studied at $M_\infty = 2.64$ and $\alpha_f = 16$ deg

In addition to surface flow visualization, the values of the upstream-influence angle and the length of flow separation at the fin apex were compared for different

grids. The upstream-influence angle β_U, as shown in Fig. 3.17, is the angle made by the line of upstream influence in the conical farfield region with the streamwise direction. Also, the length of flow separation at fin apex identified by L_{S_1} is shown in Fig. 3.17.

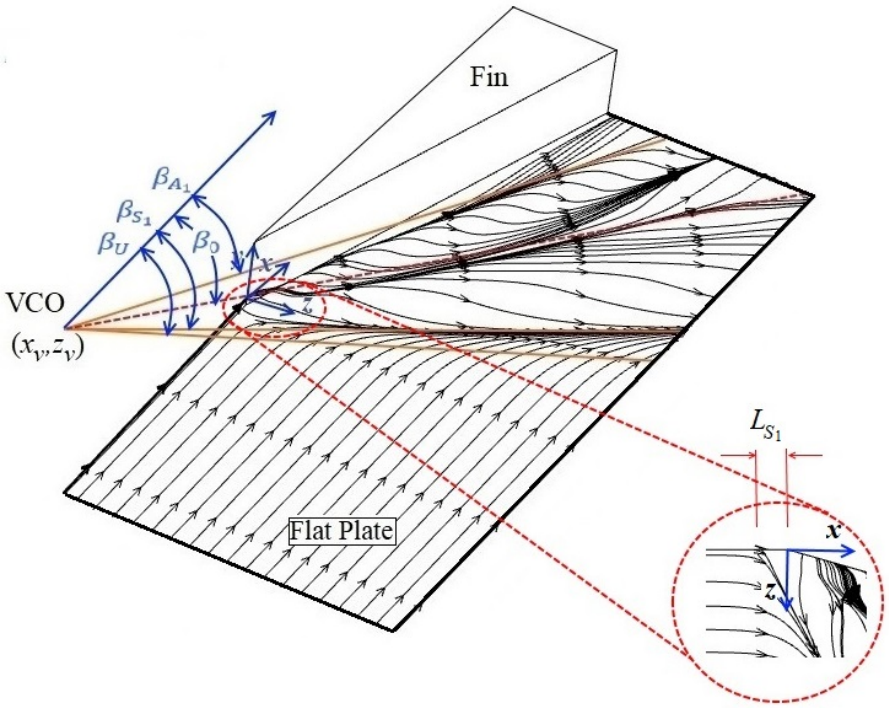

Figure 3.17: Schematic of the fin-induced interaction flowfield to show upstream-influence angle β_U and the length of flow separation at fin apex L_{S_1}

The values of β_U and L_{S_1} for all the grids considered in the GIS are shown in Table 3.7. The differences in both quantities were calculated between subsequent grids and were found to decrease with grid refinement. The values of $\Delta\beta_U$ and ΔL_{S_1} between grids 2 and 3 show a minimal variation that confirms the achievement of grid independence of flow variables and thus justify the selection of grid 2 for the present study.

Table 3.7: Comparison of flow parameters to investigate grid independence at $M_\infty = 2.64$ and $\alpha_f = 16$ deg.

Grid	β_U (deg)	$\Delta\beta_U$ (deg)	L_{S_1} (mm)	ΔL_{S_1} (mm)
1	62.47	2.80	6.35	0.83
2	65.27		7.18	
2	65.27	0.21	7.18	0.09
3	65.48		7.27	

3.4.2 Cross Shockwave/Boundary-Layer Interactions

3.4.2.1 Geometry and Boundary Conditions

The computational domain for the double fin configuration considered in the present study was selected based on the studies performed by Thivet et al. [87] on turbulent cross SBLIs. The configuration is shown schematically in Fig. 3.18 where two opposed symmetric unswept, sharp fins of length 248 mm and height 40 mm with leading-edge angles α_f are mounted on a flat plate. The fin vertices are separated by 70 mm, and the width of the throat is 30 mm. The throat is followed by a diverging duct with an angle of 20 deg, as shown in the figure. The configuration is symmetric about the centerplane. The oblique shockwaves generated by the fins interact with the flat plate boundary layer at a freestream Mach number $M_\infty = 4$ resulting in a complex flowfield [87].

The flowfield, especially of a separated cross SBLI, is rich in topological features [37] but which may be masked in a turbulent flow. There are certain parameters that significantly affect the interaction flowfield including the Mach and Reynolds numbers, the incoming boundary layer thickness, the fin leading-edge angles, the distance between the fin vertices, and the throat width. However, the present study focuses on the effect of varying fin leading-edge angles on the separated cross SBLI. Thus, different cases were considered by gradually increasing the fin leading-edge angle α_f

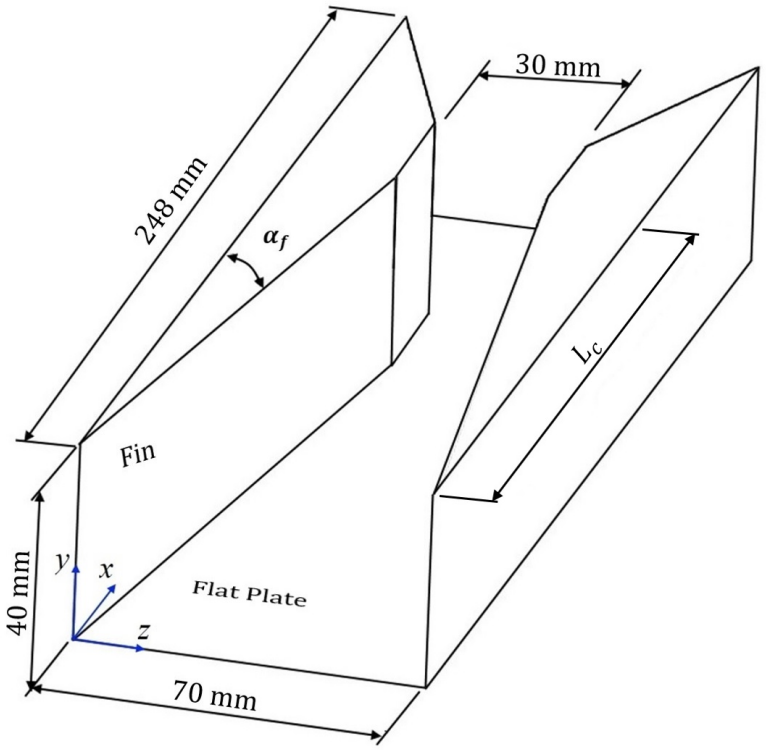

Figure 3.18: Schematic of the double fin configuration where two opposed symmetric sharp fins are mounted on a flat plate

starting at 7 deg [87], and thereby increasing the corresponding shock strengths, see Table 3.8. The streamwise length of the converging section of the fins L_c, shown in Fig. 3.18, was varied to keep the distance between the fin vertices (= 70 mm) and the throat width(= 30 mm) unchanged. The values of L_c corresponding to the values of α_f are shown in Table 3.8.

Table 3.8: Different cases considered for the present computational study.

M_∞	α_f (deg)	L_c (mm)
4	7	163
4	9	126
4	11	103
4	13	87

Figure 3.19 depicts the top view of the computational domain considered in the present study. The configuration is symmetric about the centerplane. However, following the literature [87], the footprint of the centerplane on the plate surface will be denoted as throat middle line (TML) in the present research study, as shown in the figure. The length of the flat plate till the fin apex $L_f = 150$ mm was determined to

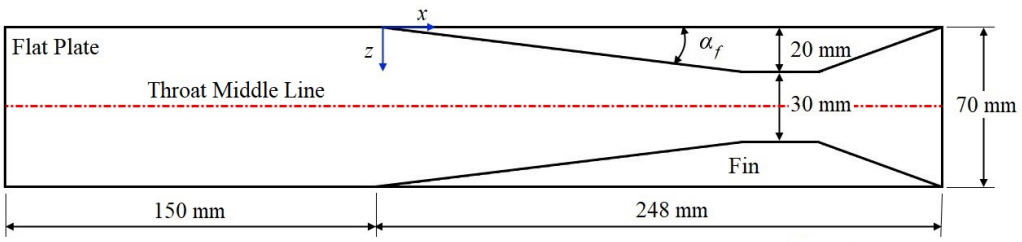

Figure 3.19: Topview of the computational domain considered for studying cross SBLI at $M_\infty = 4$

be minimally affected by the viscous interaction at the leading edge of the flat plate by using the theory of viscous interaction previously discussed. The freestream Mach number $M_\infty = 4$ was kept constant. The stagnation temperature $T_0 = 283$ K and the stagnation pressure $p_0 = 8.9$ kPa [104]. Adiabatic wall and no-slip conditions were assumed for the wall. The undisturbed boundary-layer thickness at the fin apex was found to be 4.6 mm, where the criterion for the boundary-layer edge was $0.995u_e$. The Reynolds number was kept constant in the present study and based on the value of δ, $Re_\delta = 5855$. The Prandtl number was assumed constant with a value of 0.713.

3.4.2.2 Grid Generation and Grid Independence Study

The computational grid for the cross SBLI study was generated by discretizing the domain shown in Fig. 3.19 in the (x, y, z)-directions to generate a three-dimensional structured grid. The grid density was made higher toward the plate, and

fin surfaces by applying a cell-to-cell expansion ratio of 1.1 [123] in each coordinate direction to capture the large velocity gradients in the boundary layer. The grid was also denser at the leading edge of the flat plate to properly resolve the viscous–inviscid interaction at that location. The clustering of grids was made along the throat centerplane of the domain to capture the intersection of the oblique shockwaves and the centerline flow separation. Different views of the grid generated for $M_\infty = 4$ and $\alpha_f = 7$ deg are shown in Fig. 3.20. A grid independence study (GIS) was performed

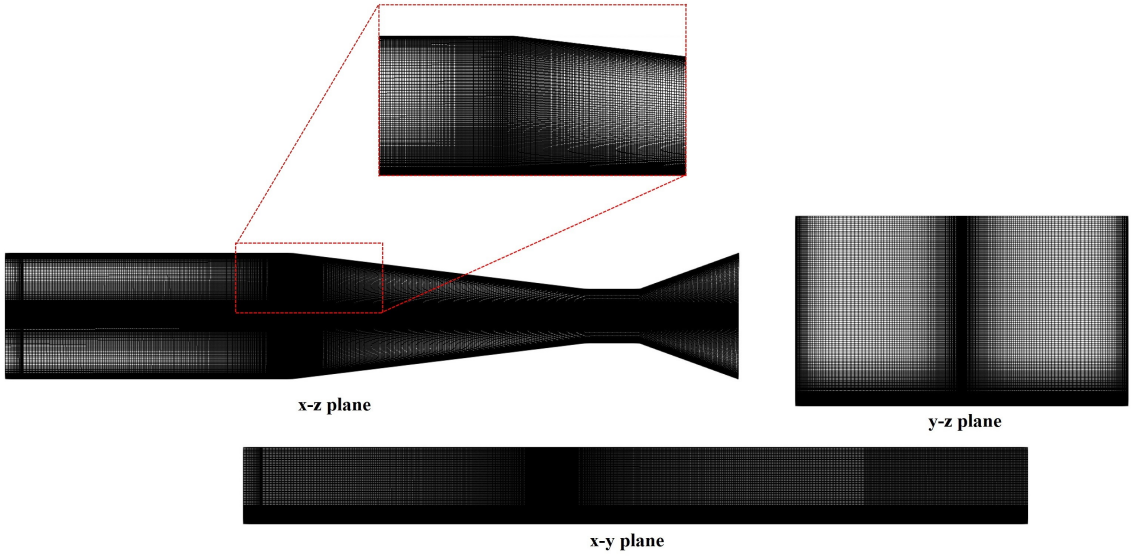

Figure 3.20: Different views of the computational grid generated for $M_\infty = 4$ and $\alpha_f = 7$ deg

to determine a grid distribution that resolves the flowfield without an excessive number of grid cells that are computationally expensive and will be discussed briefly. An example of GIS conducted for the swept shock interaction was discussed in detail previously. The same procedure was performed in the case of cross SBLI at $M_\infty = 4$ and $\alpha_f = 7$ deg and will be discussed briefly. A refinement ratio $r = 1.5$ was used

for generating the grids considered for GIS. The number of cells in each grid thus generated is shown in Table 3.9.

Table 3.9: Grids generated for GIS at $M_\infty = 4$ and $\alpha_f = 7$ deg.

Grid	$x \times y \times z$	Number of cells
1	$273 \times 70 \times 47$	898,170
2	$408 \times 105 \times 70$	2,998,800
3	$613 \times 158 \times 105$	10,169,670

The surface pressure at the throat centerplane was considered as the flow property g used in the grid independence study (see Eq. (3.24)). The values of g_1, g_2 and g_3 were 658.8, 669.6 and 674.8 Pa respectively at $x/\delta = 13$ from the fin apex. The calculated values of $e_{i,i+1}$ for the present study using Eq. (3.24) and the values of GCI for each refinement step using Eq. (3.23) are shown in Table 3.10. The order of convergence P was calculated to be 1.8 using Eq. (3.25).

Table 3.10: Relative error and GCI calculated for each refinement step.

Grids	e	GCI (%)
1, 2	1.6×10^{-2}	1.9×10^{-2}
2, 3	7.8×10^{-3}	9.4×10^{-3}

As previously discussed, a small value of the GCI is an indication that numerical uncertainty due to the discretization error is negligible and that the computation is within the asymptotic range. The achievement of the asymptotic range is examined by the Eq. (3.26) and the calculated GCIs in the present study satisfied the condition with the value of 1.01. Grid 2 with $2,998,800$ cells was selected for the present study considering the small value of GCI between grids 2 and 3, thus reducing the

computational effort. The surface pressure normalized by the incoming freestream pressure at $x/\delta = 13$ from the fin apex plotted against z is shown in Fig. 3.21 for the different grids studied.

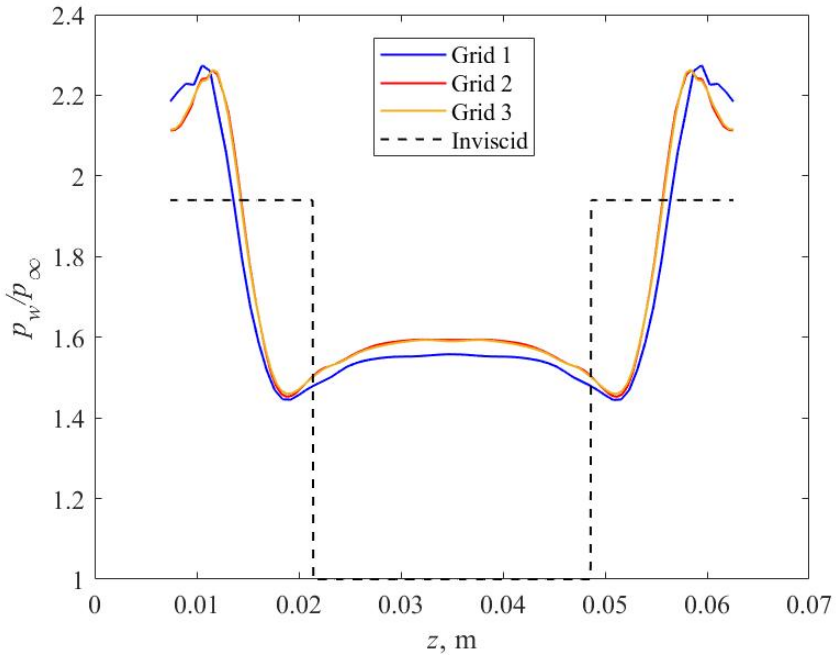

Figure 3.21: Normalized surface pressure at $x/\delta = 13$ from the fin apex for different grids studied at $M_\infty = 4$ and $\alpha_f = 7$ deg

The pressure plots collapsed upon grid refinement, as shown in the figure. The inviscid pressure distribution was also plotted, and the surface pressure downstream of the interaction close to the fin was found to be larger than the inviscid pressure. The variation of surface pressure will be discussed in detail later in Chapter 5. In addition to the surface pressure distribution, certain surface topological features in cross SBLI were investigated to confirm that the grid is properly resolved. One of the features was the length of flow separation at the fin apex identified by L_{S_1} as shown

in Fig. 3.22. Also, the location of the centerline separation from the fin apex L_{N_S} shown in the figure was compared for the different grids considered.

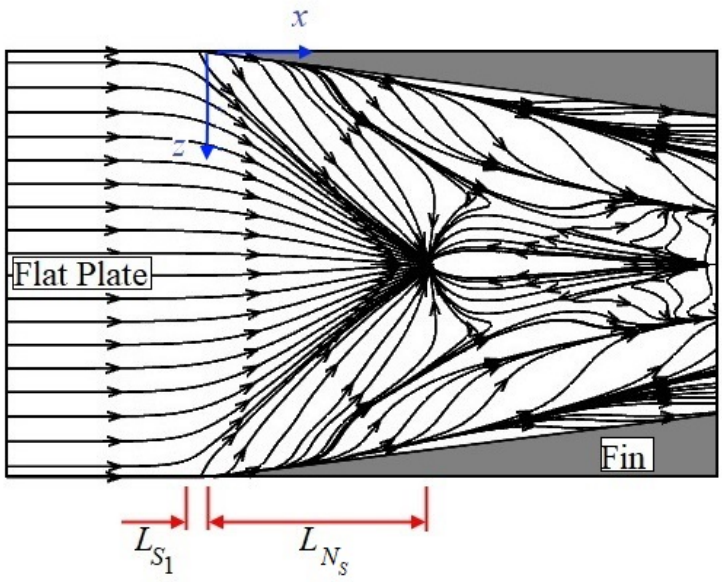

Figure 3.22: Surface topological features used for grid independence study at $M_\infty = 4$ and $\alpha_f = 7$ deg

The surface topology of cross shockwave/boundary-layer interaction will be discussed thoroughly in Chapter 5. The values of L_{S_1} and L_{N_S} for the grids considered are shown in Table 3.11. The difference in both quantities was calculated between

Table 3.11: Comparison of flow parameters to investigate grid independence.

Grid	L_{S_1} (mm)	ΔL_{S_1} (mm)	L_{N_S} (mm)	ΔL_{N_S} (mm)
1	2.71	0.13	40.5	0.44
2	2.84		40.94	
2	2.84	0.02	40.94	0.06
3	2.86		41	

subsequent grids and was found to decrease with grid refinement. The minimal variation of the flow variables between grids 2 and 3 confirms the achievement of grid independence and thus justifies the selection of grid 2 for the present study.

The minimum grid spacing in the x-direction was near the flat plate leading edge and at the fin apex with a value $\Delta x/\delta = 0.05$. The maximum spacing $\Delta x/\delta = 0.5$ was in the upstream of the fin apex. The first cell height at the flat plate surface was $\Delta y/\delta = 0.01$, and the maximum y-grid spacing was in the outer region with a value of $\Delta y/\delta = 0.13$. The grid spacing in the z-direction was concentrated near the fin surfaces and the throat centerplane with a value of $\Delta z/\delta = 0.05$ and a maximum value of $\Delta z/\delta = 0.5$ in the upstream of the fin apex.

CHAPTER 4

SWEPT SHOCKWAVE/BOUNDARY-LAYER INTERACTIONS

4.1 Flow Visualization

The oblique shockwave generated by the sharp, unswept fin interacted with the flat plate laminar boundary layer for different conditions studied. The transverse pressure gradient generated by the oblique shockwave imparts a transverse velocity to the flow. The slow-moving fluid close to the surface will be deflected more than the fluid further away because of this transverse pressure gradient and give rise to cross-flows [21]. Korkegi [58] studied incipient separation in three-dimensional turbulent interactions and found that for $M_\infty > 1.6$, the fin angle at which incipient separation occurs α_i is given by Eq. (2.2). A laminar boundary layer is more susceptible to separation than a turbulent one thus its incipient separation occurs earlier. All the cases studied were strong enough to cause flow separation.

4.1.1 Surface Flow Topology

The present understanding of three-dimensional flow separation was made from the experimental and computational surface flow visualizations of the interaction flow-field [19]. Lighthill [25] considered skin-friction lines to form the desired continuous vector field for topological analysis, and the line of separation was identified by the convergence of skin-friction lines. When the distance from the surface tends to zero, the streamlines parallel the skin-friction lines and are called limiting streamlines, as introduced by Sears [22]. Brown [23] proposed that the convergence of limiting streamlines can be used to identify the line of separation in three-dimensional studies

as shown in Fig. 4.1a. Limiting streamlines lifting off from either side of the line

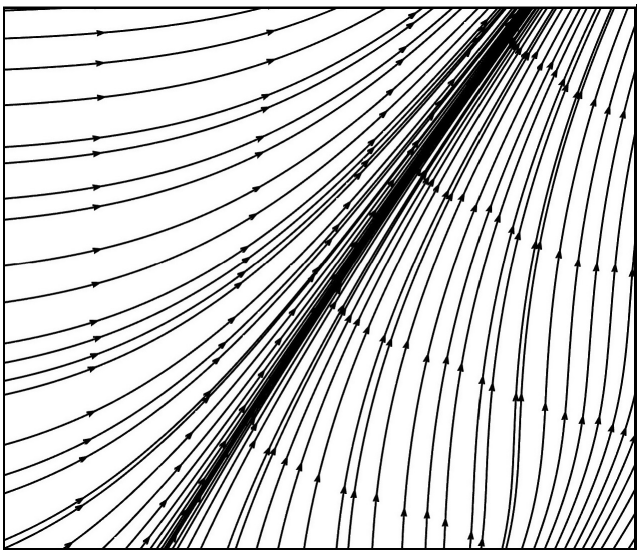

(a) Flow separation

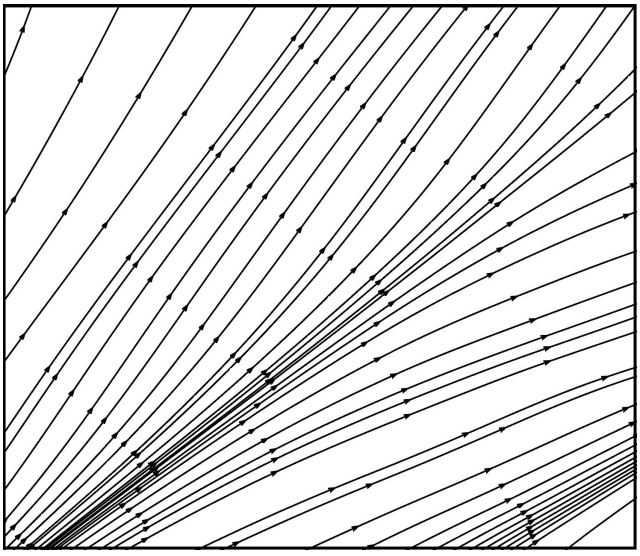

(b) Flow attachment

Figure 4.1: Separation and attachment identified by the convergence and divergence of limiting streamlines.

of separation cannot cross because of the presence of a stream surface originating from the line of separation and is a characteristic of flow separation [19]. In contrast,

skin-friction lines tend to diverge from the line of attachment [25, 128], and can be identified by the divergence of limiting streamlines as shown in Fig. 4.1b.

The oblique shockwave generated by the sharp fin was strong enough to cause separation in all the cases studied. Pressure contour of the surface flowfield at $M_\infty = 3.44$ and $\alpha_f = 16$ deg is shown in Fig. 4.2 using Paraview®. The transverse

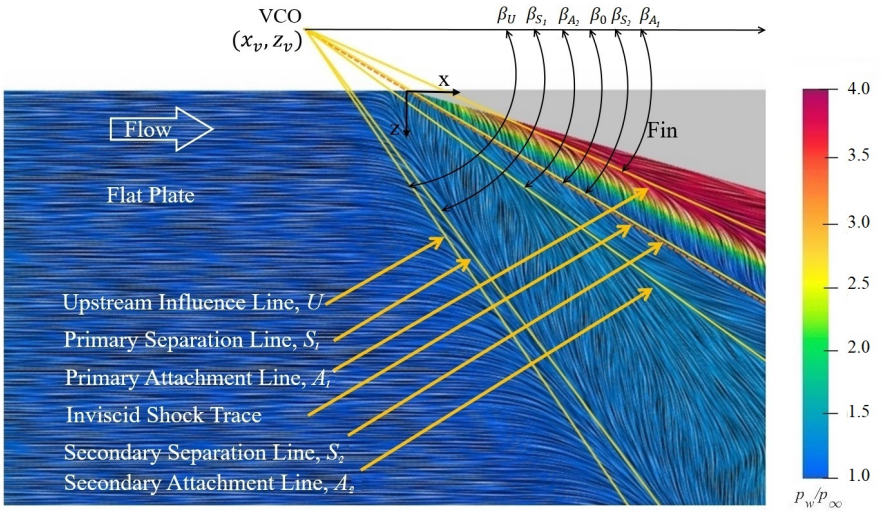

Figure 4.2: Surface pressure distribution at $M_\infty = 3.44$, $\alpha_f = 16$ deg and the location of the virtual conical origin

pressure gradient generated by the shockwave caused the development of a crossflow in the near-wall layer with a higher deflection of the slower-moving fluid close to the wall [129]. The flow features of the interaction identified in Fig. 4.2 will be explained in detail using Fig. 4.3 for the $M_\infty = 3.93$, $\alpha_f = 16$ deg case.

Streamlines at the first cell height $\Delta y/\delta = 0.014$ from the flat plate were assumed to follow skin-friction lines and are used for displaying and helping to understand the surface flow topology. This approach is justified by using the concept of limiting streamlines, already discussed. The key flow features pertinent to fin-induced

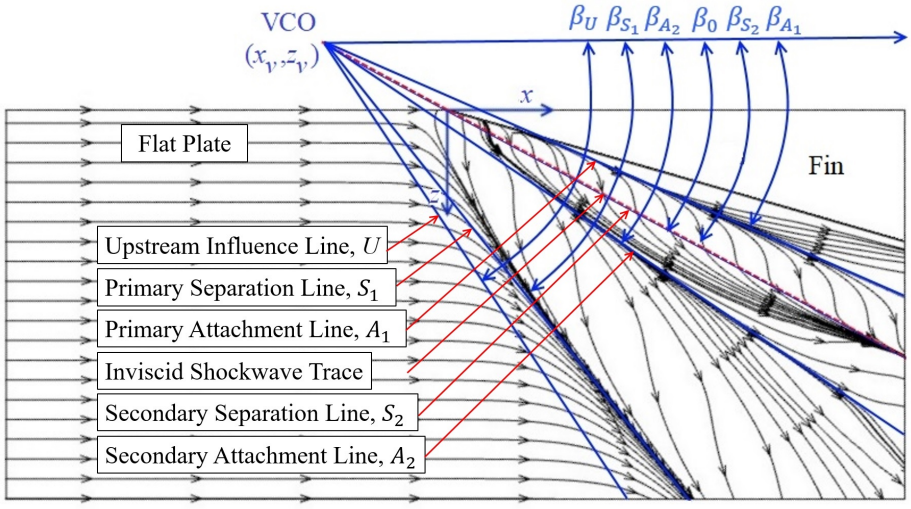

Figure 4.3: The surface flowfield and the location of the virtual conical origin at $M_\infty = 3.93$, $\alpha_f = 16$ deg

interactions can be explained based on the surface flow topology at $M_\infty = 3.93$ and $\alpha_f = 16$ deg and the resulting surface flowfield is shown in Fig. 4.3. The limiting streamlines deflected as they approached the fin, and the line of upstream influence U was identified by the beginning of this deflection. Instead of forming a separation bubble as in two-dimensional separation, the streamlines rolled up to form a vortical structure sweeping downstream. As discussed in Chapter 2, such a swept separation structure has been widely observed in various three-dimensional interaction experiments [19, 21, 84, 130]. The line of primary separation S_1 can be seen to be just downstream of U and can be understood by the convergence of the limiting streamlines [25, 131]. Close to the fin surface, an attachment line was identified that impinged the surface at the primary attachment A_1 where the limiting streamlines diverged. It can also be seen that the separated vortical structure, as identified by its surface topology [19] increased in size as the flow moved downstream.

A secondary separation was observed in the flow further downstream from fin apex and which was closer to the fin surface than the primary separation. Appearance

of secondary separation led to the formation of the lines of secondary separation S_2 and secondary attachment A_2. The key features identified here, namely, U, S_1 and A_1, together with the inviscid shock trace, were extrapolated and converged to a common point upstream of the fin leading edge. This point is termed as the virtual conical origin (VCO). Also, it can be inferred from the figure that this conical symmetry only existed further downstream from the VCO and that an inception zone existed near the fin apex [29, 30, 31, 32, 33]. The conical surface topological features made an angle β with the incoming flow direction, originating from the VCO. The angles corresponding to the flow features are identified by the appropriate subscripts and the inviscid shock trace is identified by β_0.

Another observation is that U was at a stand-off distance from fin apex. This local apical feature has apparently not been discussed in the literature but is nevertheless expected to be present. This feature is expected because the local SBLI at the apex is sufficiently strong to cause local boundary-layer separation thereby leading to the observation of a separation zone and the associated upstream influence being ahead of the apex.

4.1.2 Cross-Plane Flow Features

Experimental and numerical studies in turbulent interactions revealed a lambda-shockwave structure composed of a main shockwave, a separation shockwave, and a rear quasi-normal shockwave [78, 27, 79]. The separation shockwave is formed by the coalescence of compression waves caused by the geometry of the separation zone. Based on the results from the experimental and computational studies performed by Degrez [84, 85], the compression upstream of the inviscid shockwave in laminar interaction is more likely to be spread in a "compression fan" than a separation shockwave. The reason for the claim is that the thickening and separation of laminar boundary

layers are gentler than for turbulent interactions. A combined surface and off-surface visualization for the $M_\infty = 3.93$ and $\alpha_f = 16$ deg case is shown in Fig. 4.4. The

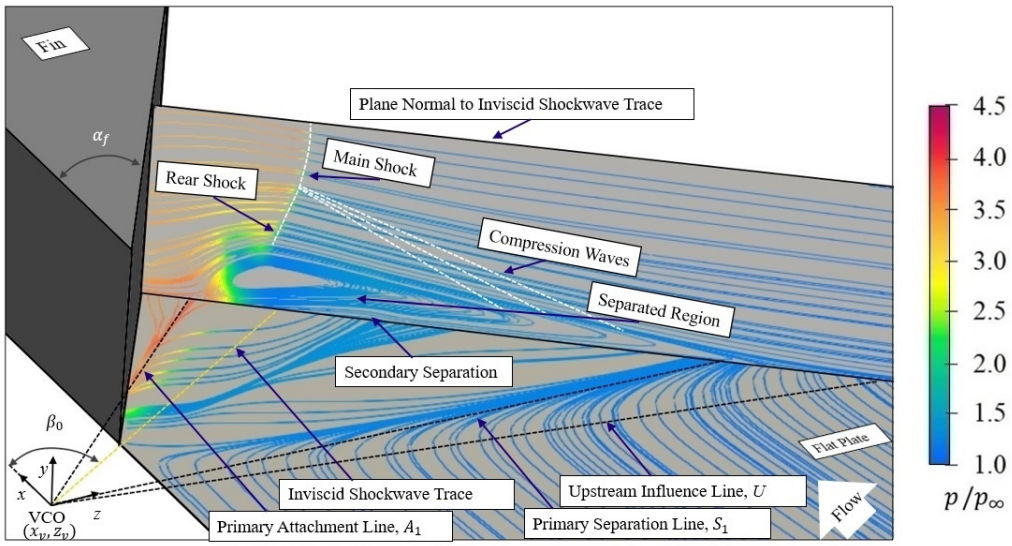

Figure 4.4: Surface and cross-plane features in fin-induced interaction at $M_\infty = 3.93$, $\alpha_f = 16$ deg, and the location of the virtual conical origin. Streamlines are colored by the pressure variation normalized by the incoming freestream pressure.

off-surface plane is taken to be normal to the inviscid shockwave and the flat plate. The incoming flow direction is shown schematically by the arrow on the lower right of the figure. Key features are identified on the plane. Streamlines are color coded by the variation of the pressure normalized by the incoming freestream pressure. An interesting observation is that the separated structure beneath the shock leg is more elongated than turbulent interactions because of the greater extent of laminar separation. A secondary separated region is also visible on the cross-plane. The convergence and divergence of limiting streamlines indicate flow separation and attachment, respectively, and are extrapolated to the virtual conical origin, as shown in the figure. The figure shows that the peak surface pressure is in the region after the shockwave. Moreover, the rise in pressure is mostly not large until behind the main and the rear

shock. The figure indicates schematically the presence of compression waves but these are too weak to be visible using this visualization technique.

4.1.3 Upstream Influence and Scaling

It was mentioned that the upstream influence is one of the key flow features in fin-generated SBLIs. The pressure rise caused by the shockwave is transmitted upstream through the subsonic part of the boundary layer. The thickness of the subsonic layer depends on the velocity profile at that point. It would be thinner for turbulent boundary layer as the velocity profile is fuller than that of the laminar case. Thus, the closer proximity of the sonic line to the flat plate surface in the case of turbulent flows is expected to lead to a lesser upstream extent than for laminar interactions. This difference was observed in the current study.

Settles and co-workers [53, 60] reported that the upstream influence is a function of Re_δ and the normal Mach number $M_n = M_\infty \sin\beta_0$ for turbulent, fin-generated SBLIs. The Dolling–Settles–Bogdonoff upstream-influence scaling law is expressed as

$$\frac{\tilde{\zeta}_U}{M_n} = f(\tilde{\xi}_U) \tag{4.1}$$

where

$$\tilde{\xi}_U = \frac{\xi_U}{\delta} Re_\delta^a \tag{4.2}$$

$$\tilde{\zeta}_U = \frac{\zeta_U}{\delta} Re_\delta^b \tag{4.3}$$

(ξ, ζ) being a shockwave-based coordinate system, as shown in Fig. 4.5. The exponents $a = b = 1/3$ are empirical constants. A fin-induced turbulent interaction study performed by Settles and Lu [121] confirmed the validity of this scaling law using the experimental data. The resulting plots at different freestream Mach numbers in the range of $2.5 - 4$ agreed well with the scaling law.

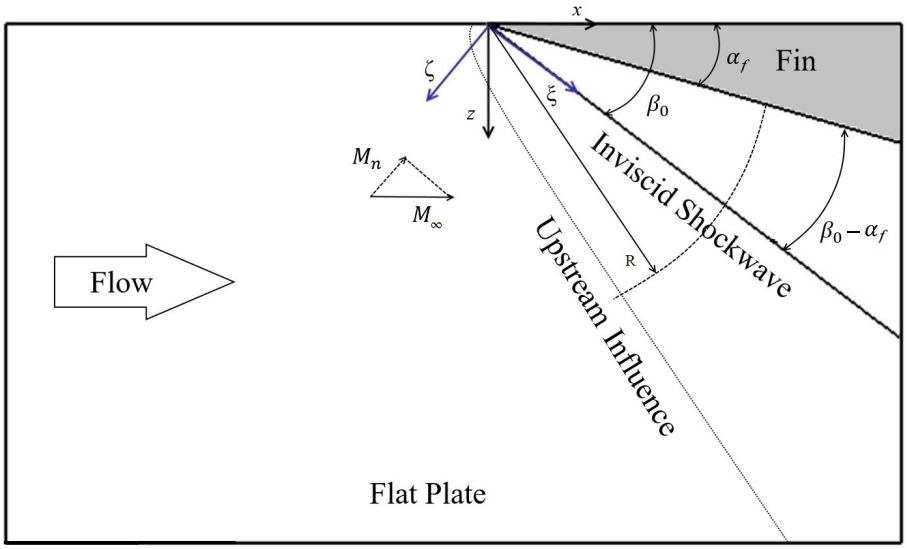

Figure 4.5: Schematic of the top-view of the fin-plate configuration

Numerical results from the present study were plotted to investigate the validity of the upstream-influence scaling law. The scaled data, according to Eq. (4.1) with the same values of exponents as for turbulent interactions, is shown in Fig. 4.6. Also shown is the scaled upstream influence for turbulent interactions [121] that reveals the much larger extent of laminar interactions, as discussed above. Moreover, the figure shows a residual Mach number effect on the laminar upstream influence that diminished as M_n was increased at a constant $\alpha_f = 16$ deg, which was not observed in turbulent interactions. This effect appears to asymptote with increasing M_∞, suggesting a limiting hypersonic behavior. In addition to that, at constant $M_\infty = 2.64$ and $\alpha_f = 16$ deg, the figure exhibits a Reynolds number influence that increased with Re_δ and an inverse α_f effect at constant values of $M_\infty = 2.64$ and $Re_\delta = 3053$.

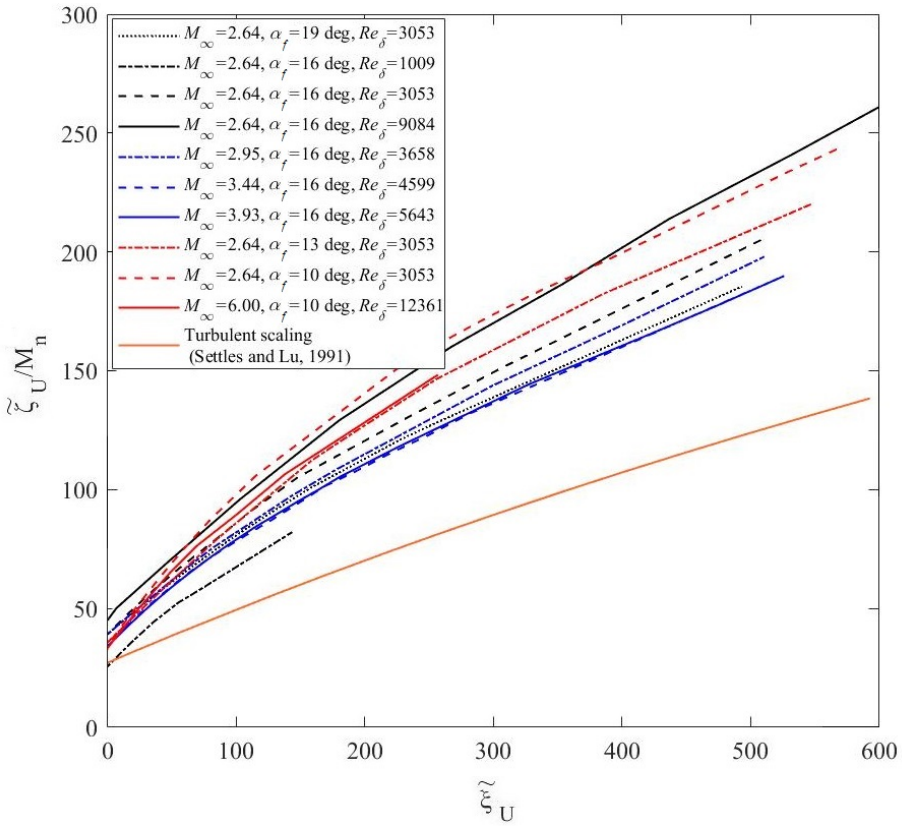

Figure 4.6: Upstream-influence scaling for fin-generated SBLIs and the comparison with turbulent results

Due to the nature of the residual Mach number effect which appeared to diminish with an increase in M_∞, it was thought that this behavior might fall into a general, three-dimensional hypersonic viscous interaction law of the form

$$\frac{\zeta}{\delta} = f\left(M^c Re^d, \frac{\xi}{\delta}\right) \tag{4.4}$$

neglecting wall temperature conditions. The use of generalized, hypersonic viscous interaction laws has been proposed previously by Stollery and co-workers [132], amongst others. The relationship was determined empirically from the computed upstream influence data, leading to

$$\frac{\hat{\zeta}_U}{M_n^{0.05}} = f(\hat{\xi}_U) \tag{4.5}$$

where

$$\hat{\xi}_U = \frac{\xi_U}{\delta} Re_\delta^{0.03} \tag{4.6}$$

$$\hat{\zeta}_U = \frac{\zeta_U}{\delta} Re_\delta^{0.03} \tag{4.7}$$

The updated exponents were applied to the values of M_∞ and Re_δ used in the study and are shown in Table 4.1. In the supersonic regime, $K_\beta = M_\infty \sin\beta_0 \approx M_\infty \beta_0$ is considered to be a better similarity parameter compared to hypersonic similarity parameter [121]. The values of K_β are also shown in Table 4.1. After applying the

Table 4.1: Mach numbers and Reynolds numbers in terms of updated scaling exponents

M_∞	α_f (deg)	β_0 (deg)	β_0 (rad)	K_β	M_n	$M_n^{0.05}$	$M_\infty^{0.05}$	Re_δ	$Re_\delta^{0.03}$
2.64	19	39.9	0.7	1.85	1.7	1.027	1.05	3053	1.27
2.64	16	36.5	0.64	1.7	1.57	1.023	1.05	1009	1.23
2.64	16	36.5	0.64	1.7	1.57	1.023	1.05	3053	1.27
2.64	16	36.5	0.64	1.7	1.57	1.023	1.05	9084	1.31
2.95	16	33.7	0.6	1.77	1.64	1.025	1.055	3658	1.28
3.44	16	30.5	0.53	1.82	1.75	1.028	1.06	4599	1.29
3.93	16	28.4	0.5	1.96	1.87	1.032	1.07	5643	1.3
2.64	13	33.3	0.58	1.53	1.45	1.018	1.05	3053	1.27
2.64	10	30.4	0.53	1.4	1.34	1.014	1.05	3053	1.27
6.00	10	17.6	0.31	1.86	1.81	1.03	1.09	12361	1.33

updated exponents, the dependence of freestream Mach number and normal Mach number is almost in the same range for the cases considered in the present study.

The computed data were scaled using Eq. (4.5) and the agreement to the scaling law is evident in Fig. 4.7. The data obtained based on the laminar experimental conditions of Zuber et al. [103] were found to agree reasonably with the scaling law at $M_\infty = 6$. Despite the satisfactory scaling, more studies should be undertaken to understand the influence of Mach number and Reynolds number.

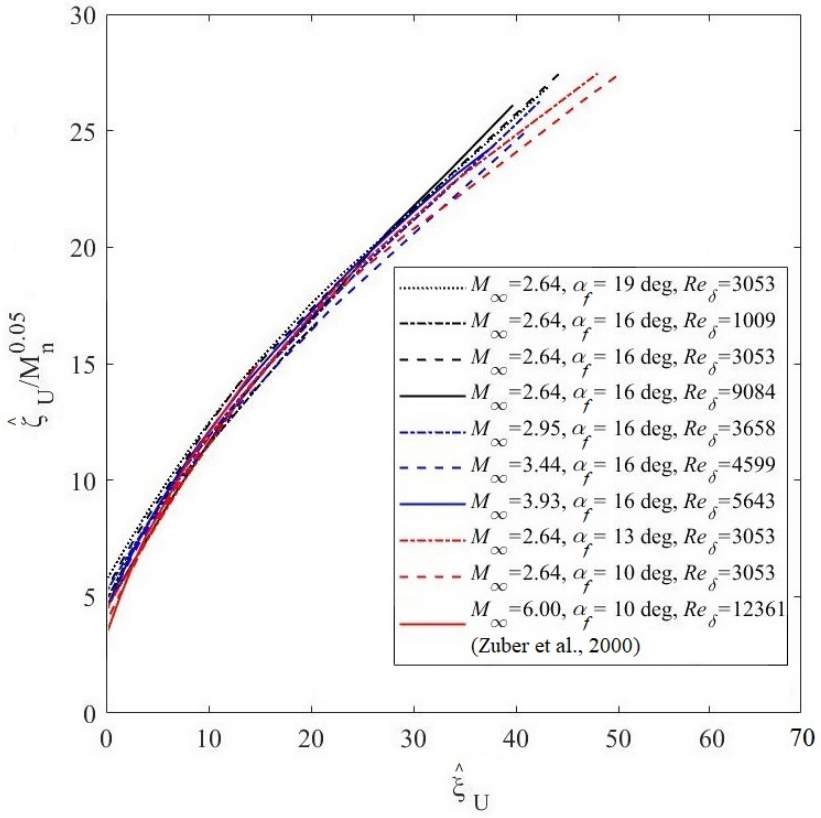

Figure 4.7: Upstream-influence scaling for fin-induced shockwave/laminar boundary-layer interactions

4.1.4 Separation and Attachment

All the cases studied exhibited an extensive open separation which appears as a flattened vortical flow. Also, the flowfield is found to be following a quasiconical nature in all the cases. The line of primary separation is seen to be just downstream of the line of upstream influence, and the line of primary attachment is close to the fin. At sufficiently large shock strengths, additional separations and attachments can develop within the primary separated region. Recalling the results obtained by Degrez [86], the primary separation is accompanied in most of the cases by a secondary separation. This is because the shock strength required for laminar separation is smaller compared to a turbulent one. Degrez also noted that, in some instances,

higher-order separations might be present in the primary separated region. This finding is relevant, but the limitations in experimental capabilities restrict the flow conditions to be tested. On the other hand, numerical simulations require a sufficient grid resolution to capture all the flowfield details.

A secondary separated region was observed in all the cases studied. As Zubin and Ostapenko [62] found, the secondary separated region in the laminar flowfield is larger than the corresponding turbulent cases due to the reasons already discussed. The secondary separated region is visible in the computed flowfield for the case of $M_\infty = 2.95$ and $\alpha_f = 16$ deg, shown in Fig. 4.8. It is evident from the surface flow

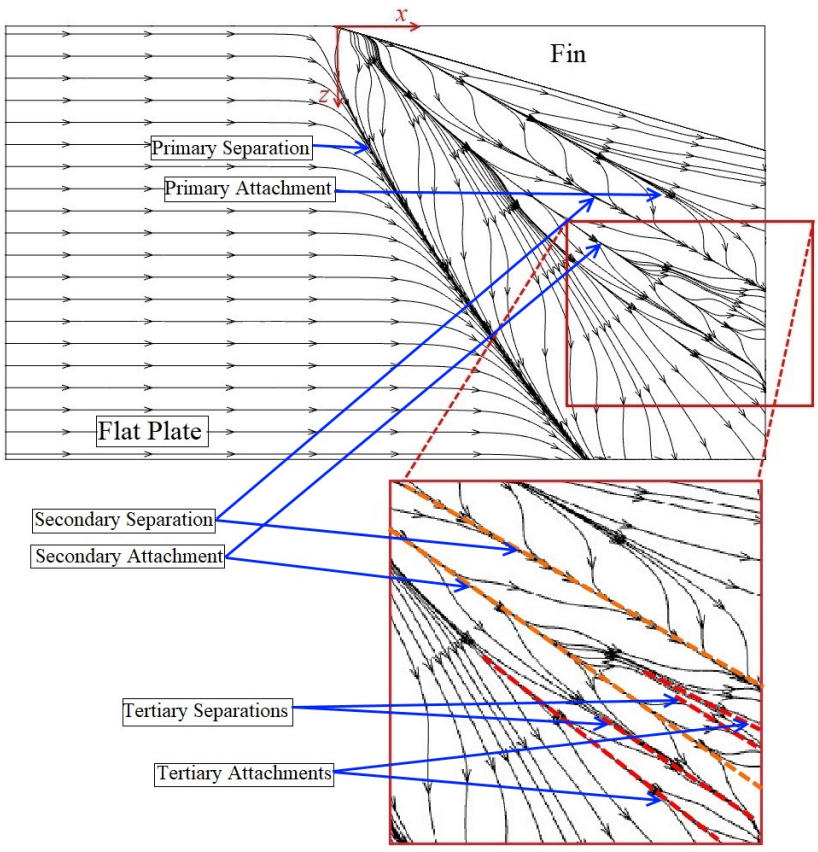

Figure 4.8: Surface topology of the fin-induced laminar SBLI at $M_\infty = 2.95$ and $\alpha_f = 16$ deg

visualization that the secondary separation occurs further downstream from the fin apex. Unlike turbulent interactions, laminar interactions correspond to an extended separated region leading to an elongated vortical flow under the shock structure. Moving downstream from the fin apex, the interaction region widens because of its quasiconical nature. In the present study, additional separated regions near the secondary attachment were visualized using surface flow topology. Even though such a possibility was mentioned by Degrez, this feature is apparently not discussed in the literature. A system of tertiary separations and attachments on both sides of the secondary attachment line is evident from the surface topology by the convergence and divergence of limiting streamlines, respectively. Additionally, the presence of tertiary separation can be studied using an off-surface visualization.

A schematic of the plane normal to the fin-induced inviscid shockwave in the farfield of the interaction region is shown in Fig. 4.9 using dashed lines. Moreover,

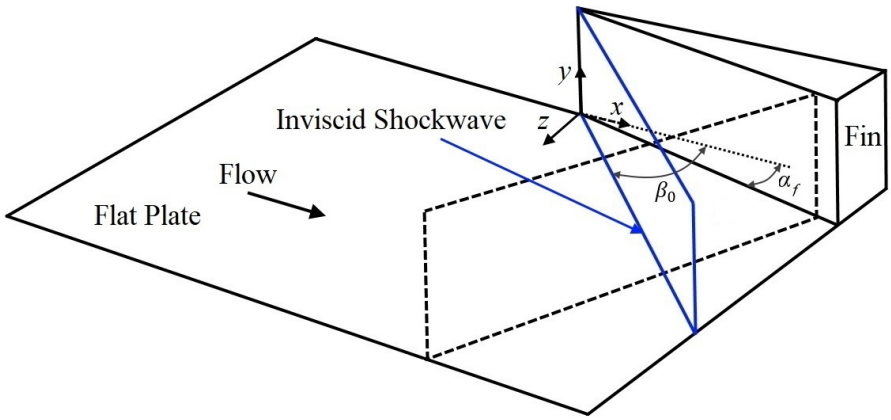

Figure 4.9: Schematic of the fin-plate configuration to show a plane normal to the inviscid shockwave

the plane is normal to the flat plate surface, and can be used to study the system

of tertiary separations and attachments on both sides of the secondary attachment. An off-surface visualization on the plane using streamlines showing the multiple separations and attachments is displayed in Fig. 4.10. The separated flow from the

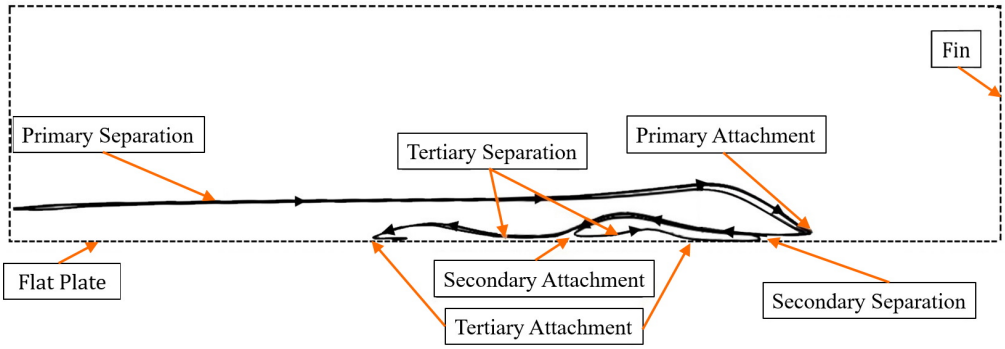

Figure 4.10: Tertiary separation in fin-induced interaction at $M_\infty = 2.95$, $\alpha_f = 16$ deg

primary separation moving towards the fin surface was found to attach at the primary attachment. The flow direction is shown using arrows. The locations of secondary separation and attachment beneath the primary separated flow are noticeable in the figure. The presence of secondary separation and attachment was confirmed in numerous experimental and computational studies [21]; however, as it is displayed in the figure, the flow impinging at the secondary attachment was found to further separate and attach on either side. Another off-surface visualization is made using streamlines and Mach number variation, as shown in Fig. 4.11 on the plane normal to the inviscid shockwave in the farfield of the interaction. The additional separated regions on both sides of the secondary attachment are visible in the Mach number contours within the primary separated region. It appears logical to explain the occurrence of the "new" separated regions using an impinging supersonic jet model. The flow at the secondary attachment can be considered as an inclined supersonic jet impinging on

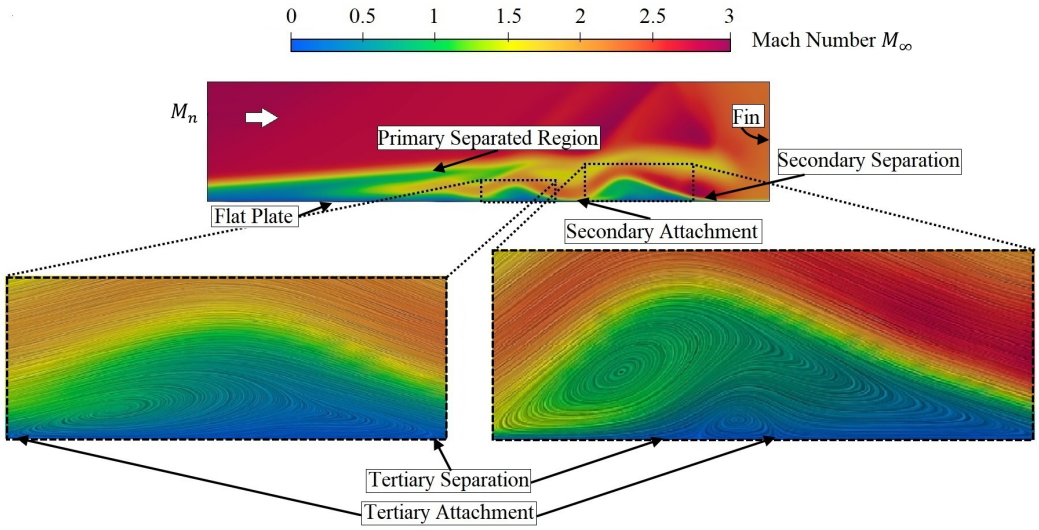

Figure 4.11: Visualization of tertiary separation in the interaction flowfield at $M_\infty = 2.95$ and $\alpha_f = 16$ deg along a plane normal to the inviscid shockwave

the flat plate surface similar to an Edney type IV interaction [15]. The impinging jet causes a high pressure at the attachment. A schematic of the inclined supersonic jet impinging on a flat plate is displayed in Fig. 4.12 [6]. Since the jet is inclined, it is not expected to separate symmetrically on both sides of the impinging location. Such an observation can be made in the present case where one separated region (on the left in Fig. 4.10) is larger than the other. The surface flow topology (see Fig. 4.8) can also be used to confirm this observation. Henderson [133] and Lamont and Hunt [6, 134] studied the impinging jet problem on flat plates and wedges, and this asymmetry can be confirmed in the results.

The flow conditions for the existence of an impinging supersonic jet were calculated by Henderson [135] with the aid of shock polar. According to his study, the freestream Mach number must be at least equal to approximately 2.4 for the appearance of a supersonic jet. In the present study, all the Mach numbers considered are greater than 2.4. Hence, it is expected to occur in the cases studied presently. How-

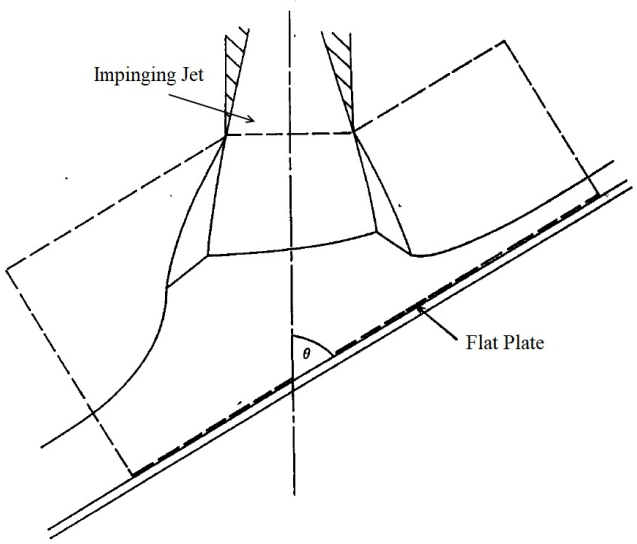

Figure 4.12: Schematic of an inclined supersonic jet impinging on a flat plate [6]

ever, the factors affecting the appearance of the multiple separated regions include the extent of the separated region and the intensity of shock strength. Investigations were performed using different combinations of freestream Mach number and fin angle to develop an expression to recognize the location of tertiary separation. A radius R on the flat plate surface centered at the fin apex, as shown in Fig. 4.5, was used to identify the beginning of this separation. It was found that for the different conditions studied, $(R/\delta)(\beta_0 - \alpha_f) \approx 10$. The radius R was normalized by the undisturbed boundary-layer thickness at the fin apex. The values of flow parameters and the resulting expression are shown in Table 4.2. Another observation is that the value of R from the fin apex increases with the freestream Mach number. Hence, the occurrence of tertiary separation will be further downstream of the fin apex at higher Mach numbers.

Table 4.2: Location of tertiary separation.

M_∞	α_f (deg)	β_0 (deg)	$\beta_0 - \alpha_f$ (rad)	R (mm)	δ (mm)	$(R/\delta)(\beta_0 - \alpha_f)$
2.64	19	39.9	0.37	93	3.5	9.8
2.64	16	36.5	0.36	94	3.5	9.7
2.95	16	33.7	0.32	117	3.9	9.6
3.44	16	30.5	0.25	159	4.2	9.6
3.93	16	28.4	0.22	196	4.5	9.6
2.64	13	33.3	0.35	97	3.5	9.7
2.64	10	30.4	0.35	98	3.5	9.8

4.2 Free Interaction Theory

Studies from previous investigators in three-dimensional interactions provided evidence of conical free interaction by the collapse of surface pressure in the vicinity of the upstream influence. There does not appear to be attempts in extending the correlations developed for free interaction to three-dimensional, conical interactions. These previous studies found that conical symmetry occurs only in a farfield region, following an inception region near the apex, as shown in Fig. 4.13 [32]. The quasiconical nature established in laminar fin-induced interactions [136, 137] facilitates the examination of surface flow features. This coordinate system is (R_v, β) where R_v is the radius from the VCO and β is the angle made by surface flow features with respect to the incoming freestream direction.

The conical nature of the separated farfield flow allows for the polar coordinate system centered on the VCO to be applied, as shown in Fig. 4.13. The distance between the interaction onset and the point of separation is no longer described by length scales. Hence, new parameters must be introduced. In particular, analogous to $\bar{x}$ in two-dimensional interactions is the normalized angle

$$\bar{\beta} = \frac{\beta - \beta_U}{\beta_S - \beta_U} \tag{4.8}$$

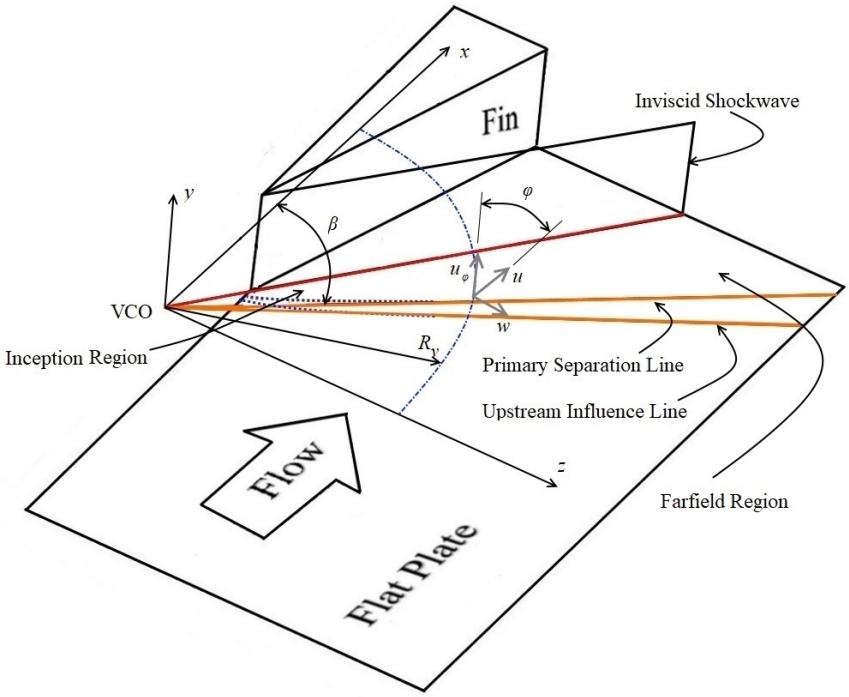

Figure 4.13: Schematic of the fin-plate configuration showing (R_v, β) coordinate system

The universal correlation function in two-dimensional interactions was then updated with the normalized angle $\bar{\beta}$. Thus, the correlation function for three-dimensional conical interactions becomes

$$F(\bar{\beta}) = \sqrt{f_1(\bar{\beta}) f_2(\bar{\beta})} \tag{4.9}$$

where

$$f_1(\bar{\beta}) = \int_{\bar{\beta_U}}^{\bar{\beta}} \left(\frac{\partial \bar{\tau}}{\partial \bar{y}} \right)_w d\bar{\beta} \tag{4.10}$$

and

$$f_2(\bar{\beta}) = \frac{\partial \bar{\delta^*}}{\partial \bar{\beta}} \tag{4.11}$$

The boundary-layer parameters involved in the analysis were calculated based on the circumferential velocity [138], identified as u_ϕ (see Fig. 4.13), and is given by

$$u_\phi = u\cos\phi - w\sin\phi \tag{4.12}$$

where u and w are the velocity components in x and z directions respectively. Also, ϕ is the angle made by u_ϕ to the incoming flow direction. Results from the present study at a normalized radius $R_v/\delta = 38$, which is in the farfield of the interaction region, are plotted according to Eq. (4.9) and is shown in Fig. 4.14. The results with

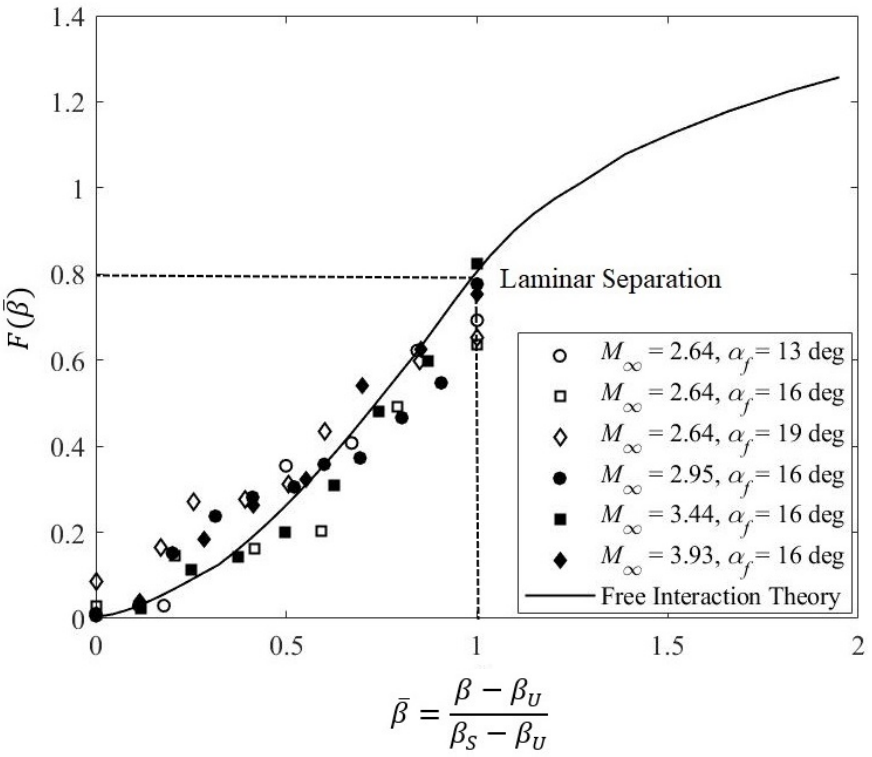

Figure 4.14: Free interaction theory applied to laminar fin-induced SBLI

different combinations of freestream Mach number and fin leading-edge angle agree reasonably well to the conical free interaction theory. This agreement means that the flow is independent of downstream influences. Thus, free interaction is further

confirmed for quasiconical interactions through an appropriate change of coordinate system.

4.3 Surface Pressure Distribution

The surface pressure distribution upstream of the shockwave should exhibit a universal form that possesses the characteristic plateau and dip to confirm quasiconical free interaction. The variation of surface pressure was examined for $M_\infty = 3.44$ and $\alpha_f = 16$ deg at different locations in the farfield region (see Fig. 4.15) normal to the inviscid shockwave to ensure quasiconical free interaction.

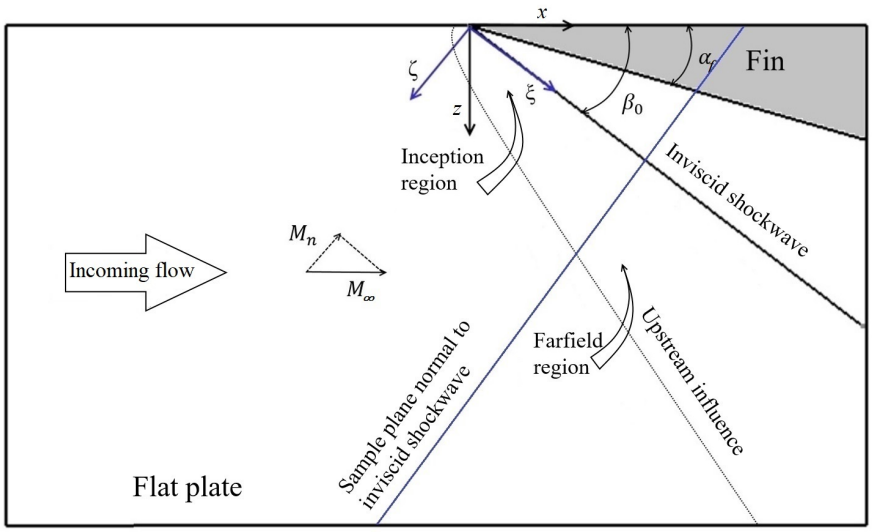

Figure 4.15: Schematic of the top-view of the fin-plate configuration

The surface pressure p_w was normalized by the incoming freestream pressure p_∞ and was plotted against the angle $(\beta - \beta_0)$ at different x/δ from the fin apex and shown in Fig. 4.16. As can be observed from the plots, the surface pressure distribution showed an excellent collapse indicating quasiconical free interaction. The surface pressure started to rise along the line of upstream influence by the generation

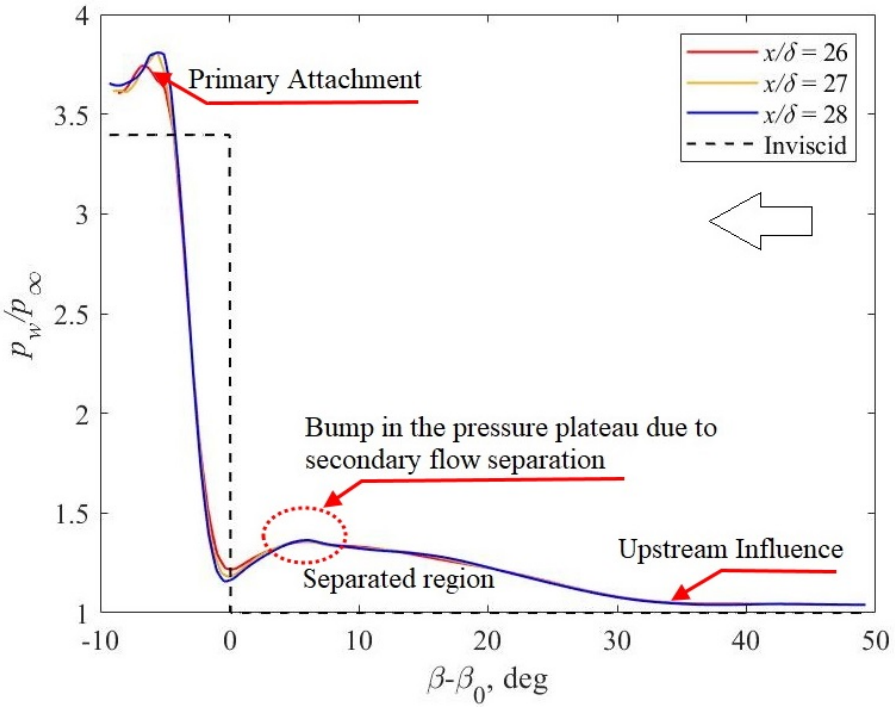

Figure 4.16: Surface pressure distribution on a plane normal to the shockwave at $M_\infty = 3.44$ and $\alpha_f = 16$ deg at different values of x/δ. Flow direction is shown using the arrow.

of compression waves. This increase in pressure then reached a plateau typical of separated flows. A second more progressive rise to a peak pressure occurred at the reattachment close to the fin at A_1. The inviscid pressure jump is also shown in Fig. 4.16 and is found to be lower than the peak pressure at the primary attachment. The flow direction is from right to left in this plot and is shown by the arrow. The small bump in the pressure plateau, observed further downstream of the fin apex, was identified as secondary flow separation.

Additionally, the surface pressure variation normalised by the incoming freestream pressure in the direction normal to the inviscid shockwave was examined for different Mach numbers considered in the present study, keeping the fin angle fixed at $\alpha_f = 16$ deg at $x/\delta = 20$ from the fin apex along x-axis, which is in the farfield of

the interaction region and are shown in Fig. 4.17. Inviscid pressure jumps cor-

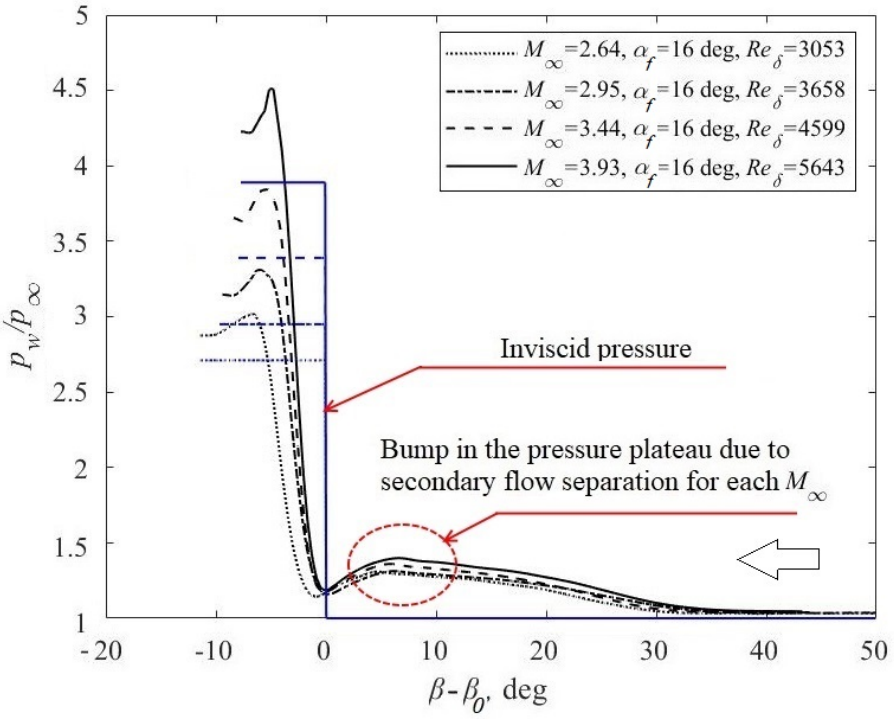

Figure 4.17: Surface pressure distribution on a plane normal to the shockwave for different Mach numbers

responding to each Mach number studied are also considered and the flow direction is from right to left in this plot. As can be observed, the surface pressure distribution showed good collapse indicating conical free interaction. The surface pressure started to rise along the line of upstream influence by the generation of compression waves, as already discussed. This increase in pressure then reached a plateau typical of separated flows. A second more progressive rise to a peak pressure took place at the reattachment close to the fin at A_1. For each Mach number, this peak pressure is larger than the corresponding inviscid pressure jump. The small bump in the pressure

plateau, observed further downstream of the fin apex, was identified as being due to secondary separation.

Degrez [139] studied different geometries, namely, the unswept wedge, asymmetric dihedron, and a half-circular cone. Conical free interaction was confirmed by the collapse of the pressure plots near the upstream influence. Thus, it is worthwhile to examine the surface pressure distribution in the present fin-induced interaction study using the normalization procedure by Lu [27]. The normalized surface pressure distributions for a combination of different Mach numbers $M_\infty = 2.64$ and 2.95 and fin angles $\alpha_f = 16$ and 19 deg are plotted at the farfield region. The normalized pressure

$$p^* = \frac{p - p_\infty}{p_{plat} - p_\infty} \tag{4.13}$$

In the spherical framework of conical interactions, the abscissa can be simplified by introducing a normalized angle

$$\beta^* = \frac{\beta - \beta_0}{\beta_U - \beta_0} \tag{4.14}$$

noting that surface features can be expressed by polar coordinates. At the upstream influence, β^* reaches unity. The surface pressure distribution normal to the inviscid shockwave at a radius $R_v/\delta = 38$ in the farfield region is plotted using the normalization procedure and is shown in Fig. 4.18. The typical plateau and dip characteristics of the universal pressure distribution is evident from the plot. Moreover, the collapse of the data from separated interactions of different strengths indicate the appropriateness of this scaling procedure for laminar fin interactions and evidence of conical free interaction. It can be inferred from the transformed pressure distribution that conical free interactions result in a universal pressure distribution. The data for all the cases collapse together from the upstream influence to the vicinity of the invis-

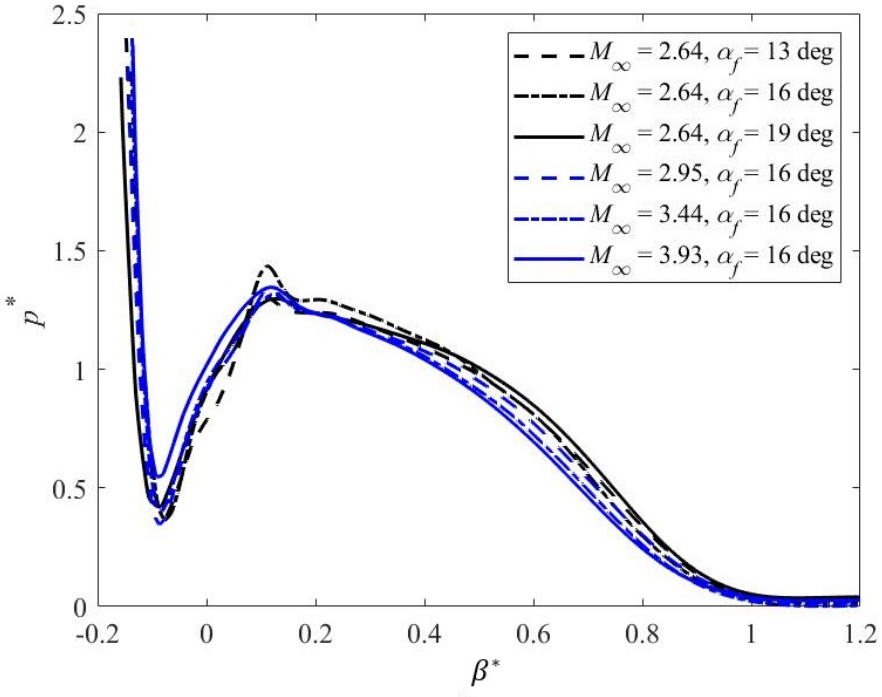

Figure 4.18: Universal pressure distribution plot

cid shockwave location at $\beta^* = 0$. Thus, the quasiconical free interaction concept is reinforced from observations of the surface pressure at different shock strengths studied. The "hump" that appears in the pressure plateau is due to the secondary flow separation, as already mentioned.

It is imperative to plot the surface pressure distribution further downstream to study about the tertiary separated regions visualized from the surface topology. A typical plateau-dip should be present at those regions where the limiting streamlines converge and diverge for separation and attachment, respectively. Fig. 4.19 shows the surface pressure distribution in the farfield of the interaction flowfield at $M_\infty = 2.95$ and fin angle $\alpha_f = 16$ deg. The locations at which the surface pressure variation is studied are identified by the shockwave coordinate normalized by the undisturbed boundary-layer thickness at the fin apex. An additional pressure plateau is clearly

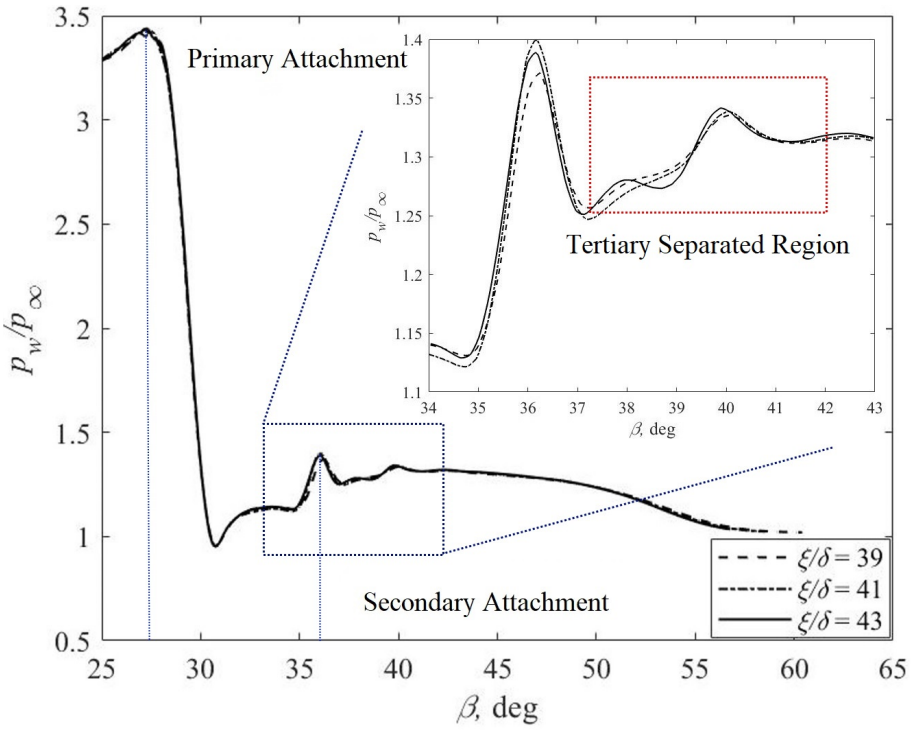

Figure 4.19: Surface pressure distribution confirming the presence of tertiary separation at $M_\infty = 2.95$ and $\alpha_f = 16$ deg

visible to the left side of the pressure rise due to the secondary attachment. As already discussed, in the case of an inclined supersonic jet, it is not expected to separate symmetrically on both sides of the impinging location (secondary attachment in the figure). An observation in the present case was made using flow visualizations where one separated region is larger than the other. The studies performed by Lamont and Hunt [6, 134] and Henderson [133] on impinging jet on flat plates and wedges show this asymmetry in the surface pressure distributions.

CHAPTER 5

CROSS SHOCKWAVE/BOUNDARY-LAYER INTERACTIONS

A large number of experimental and computational investigations have been carried out on crossing-shock interactions involving turbulent boundary layers but there are fewer involving laminar flows. However, as stated a few times previously, the study of laminar interactions is significant for understanding flow physics. The complex flowfield resulting from symmetrical, crossing shockwave/laminar boundary-layer interactions was studied presently at Mach 4 and fin leading-edge angles $\alpha_f = 7$, 9, 11, and 13 deg. Two oblique shockwaves induced by the sharp fins from opposite families intersect at the throat centerplane and generated reflected shockwaves. Further, these shockwaves impinge on the fin surfaces before reflecting again towards the throat centerplane. Such a phenomenon can lead to crossing shockwaves further downstream in the interaction region. However, the present study is focused on the flowfield induced by the primary shock intersection.

5.1 Flow Visualization

The crossing oblique shockwaves interacted with the flat-plate laminar boundary layer, and all the interactions considered were strong enough to cause flow separation. Due to the strong adverse pressure gradient generated by the intersecting shockwaves, the fluid lifts along the line of primary separation without reattaching to the wall resulting in an open separation.

5.1.1 Surface Flow Topology

The computed surface flow visualization induced by the primary shock intersection will be discussed using the concept of limiting streamlines. The topology was studied at the first cell height from the flat plate $\Delta y/\delta = 0.01$. The key flow features resulting from the interaction were found to be symmetrical about the throat centerplane because of the configuration considered. The initial part of the interaction region on either side of the throat centerplane, namely, the primary separation and attachment lines, is similar to that of single fin-induced interactions.

The surface flowfield was visualized at $M_\infty = 4$ and $\alpha_f = 7$ deg, as shown in Fig. 5.1. The figure is color-coded by the variation of surface pressure normalized

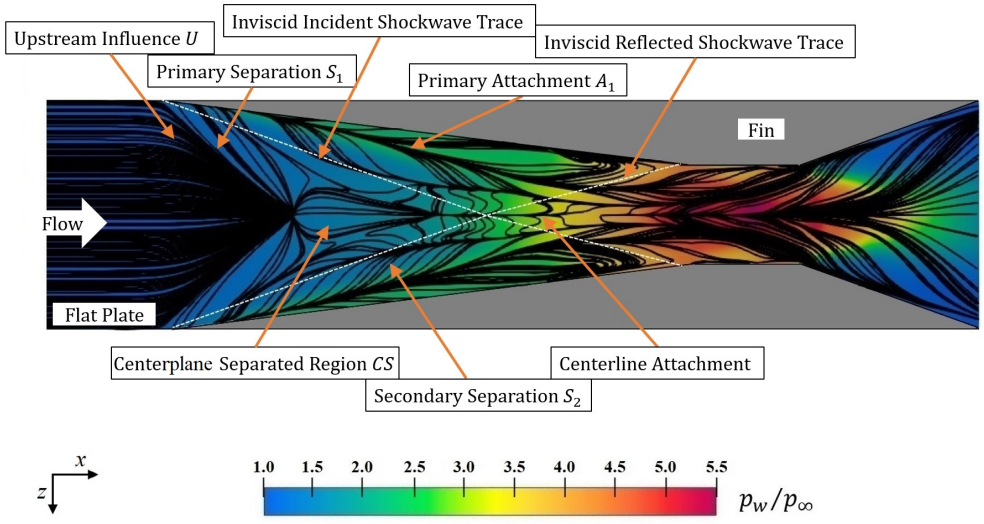

Figure 5.1: Computed surface flowfield of crossing shock interactions at $M_\infty = 4$ and $\alpha_f = 7$ deg. For convenience, only one of the symmetric flow features is labeled

by the incoming freestream pressure. The location of the inviscid shockwave system is indicated by the dashed lines. The flow direction is from left to right, as shown in the figure using an arrow. It is evident from the figure that the flowfield is rich

in topological features. As previously discussed in single fin-induced interactions, the limiting streamlines begin to deflect in the vicinity of the line of upstream influence U, where the rise in pressure is first felt. A similar procedure can be used in crossing shock interactions where the limiting streamlines are deflected by the interactions induced by the individual fins. However, the deflection was found to diminish moving towards the throat middle line and asymptotically approach one another to form a narrow region of parallel flow in the streamwise direction at the throat middle line. Hence, the variation of surface pressure should also be considered to identify the lines of upstream influence.

Similar to the single fin-induced interaction, the lines of primary separation S_1 downstream of the upstream influence were present in crossing-shock interactions corresponding to the individual fins. The flow accumulating at the lines of primary separation left the flat plate surface as a free-shear layer and rolled up to form two primary counter-rotating vortical structures moving downstream. The computed surface flow pattern exhibited the footprint of this primary separation extending the entire spanwise distance from one fin to the other, as shown in Fig. 5.1, and can be identified by the convergence of limiting streamlines [19].

As discussed in the case of an open separation, a different stream surface is attached to the flat plate surface and can be recognized by the divergence of limiting streamlines (primary attachment A_1) close to each fin. A centerplane separated region CS can be found in the immediate downstream of the intersection of the lines of primary separation. Such a flow feature was visualized in turbulent interaction studies [4] at a higher shock strength than that in the present investigation. This can be because the laminar flows are more susceptible to separation than turbulent ones. More discussion on the centerplane separated region and a comparison of this flow feature for the different cases studied will be made in the next section.

A second line of converging streamlines was found downstream of the primary separation close to and roughly parallel to the throat middle line. This feature is identified as the line of secondary flow separation S_2. Finally, a second line of divergence can be understood on the TML that corresponds to the centerline attachment. An interesting observation is that the secondary separation and the centerline attachment approach each other as they move downstream. As mentioned earlier, the present study focuses on the separated flowfield induced by the primary shock intersection shown using the dashed lines. The topological features were evident in all the cases considered. However, as the shock strength increases with the fin leading-edge angle, the limiting streamlines deflect more with increasing shockwave angle.

5.1.2 Centerplane Separated Region

The surface flow topology near the centerplane separated region CS at $M_\infty = 4$, and $\alpha_f = 7$ deg shown in Fig. 5.2 will be discussed in this section. Incident and

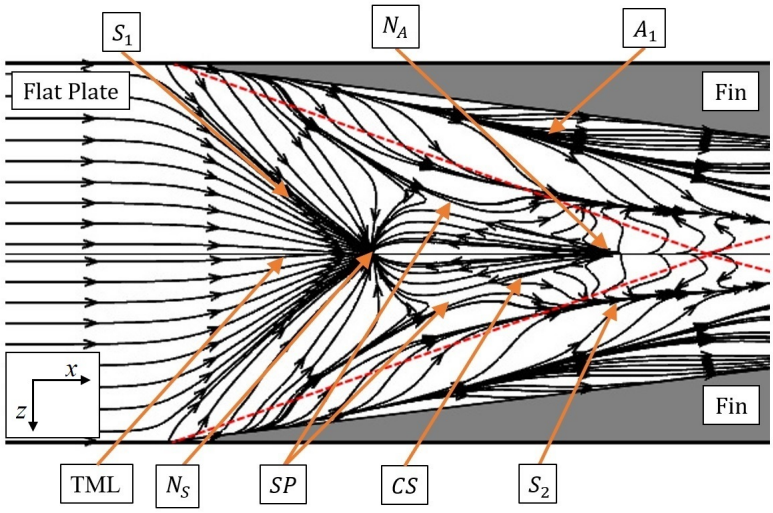

Figure 5.2: Computed surface flowfield in the vicinity of the centerplane separated region at $M_\infty = 4$, and $\alpha_f = 7$ deg

reflected shockwave traces are shown using dashed lines. In addition to the flow features already seen, a brief discussion on the singular points on both sides of the the throat centerplane will be made. Legendre [140] has shown that the separated flowfield can be interpreted by introducing a minimal number of elementary singularities. The singular points are classified as nodal points N and saddle points SP [19]. The separation node (N_S), the attachment node (N_A), and the saddle points (SP) identified in the surface flowfield are shown in the figure. The separation node shown in the figure was recognized by the arrangement of limiting streamlines where all the lines are directed towards the nodal point N_S. The location of this separation node can be considered as the beginning of the centerplane separated region and is found to be at a distance of $x/\delta \approx 9$ from the fin apex for the case of $M_\infty = 4$ and $\alpha_f = 7$ deg. At the attachment node, the limiting streamlines are found to be directed away from the nodal point N_A. The saddle points were identified by the pattern of limiting streamlines where the directions on either side of the singular point (SP) are inward on one particular line and outward on the other.

The centerplane separated region was visualized using streamlines and limiting streamlines, as shown by the dashed boundary in Fig. 5.3. The streamlines are color-coded by the magnitude of velocity normalized by the incoming freestream velocity. The flow lifts at the separation node, and the surface flowfield is shown using the white-and-gray limiting streamlines. An off-surface plane parallel to the incoming streamwise direction is also shown enlarged in the figure at the midsection. Further light may be shed on the structure of the centerplane separated region by the examination of streamlines in the symmetry plane. The flow attaching close to the fin apex moves spanwise towards the centerplane separated region as displayed using limiting streamlines. The key flow features discussed earlier in the surface flow topology are also presented in the figure. More discussion on the separated flow structures

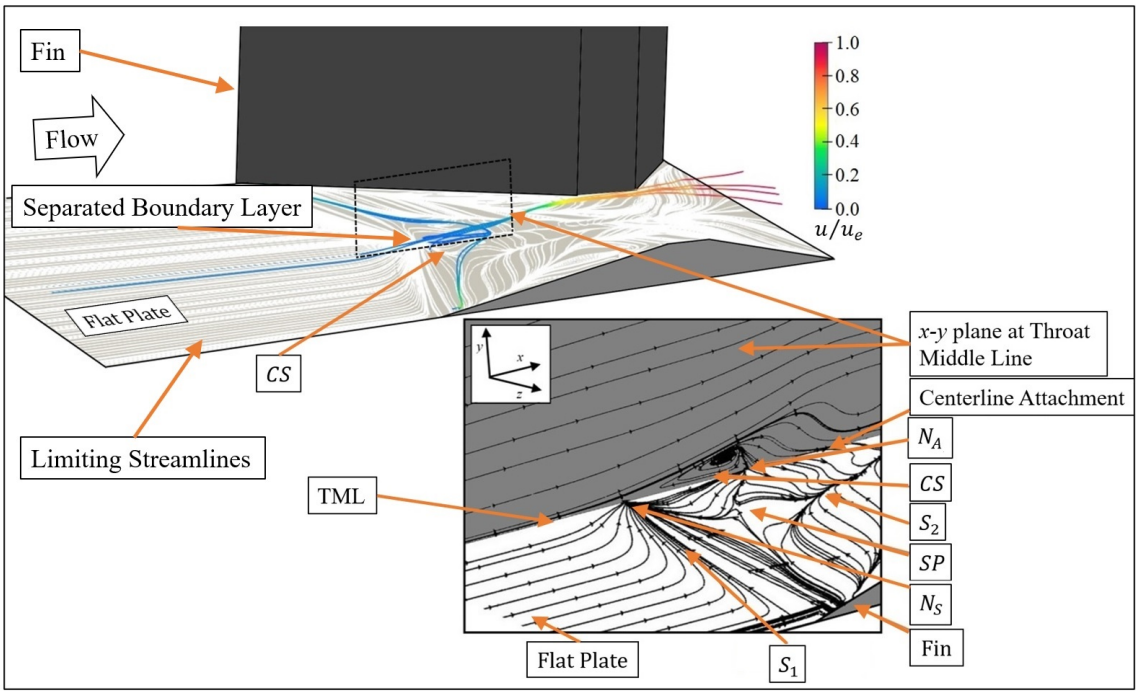

Figure 5.3: Visualization of the centerplane separated region using streamlines and limiting streamlines at $M_\infty = 4$ and $\alpha_f = 7$ deg

will be made later in this chapter. When the fin leading-edge angle was increased, the corresponding shockwave angle induced by the fins was also increased, resulting in the crossing of shockwaves happening further ahead than otherwise. Due to the upstream movement of the location of the intersection, the surface flow topology was altered. However, the critical flow features and singular points discussed above were found in all the cases studied.

A comparison of the surface flowfield in the vicinity of the centerplane separated region is shown in Fig. 5.4. The lines of primary separation from the individual fins tend to turn in a spanwise direction while approaching the throat centerplane, as shown in the figure. This can be attributed to the merging of compression waves corresponding to the individual fin-induced interactions. Additionally, the footprint of the centerplane separated region in the immediate downstream of S_1 was found

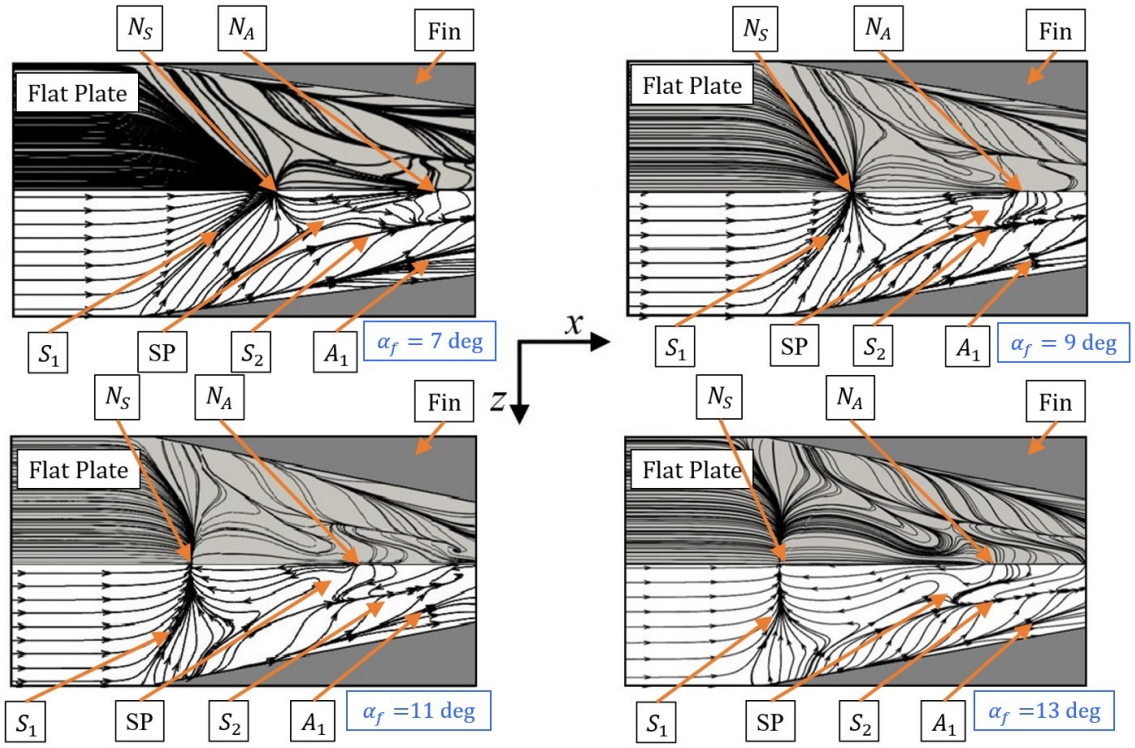

Figure 5.4: Comparison of the centerplane separated region for the different cases considered

to increase with the shock strength. The lines of secondary separation were also indicated in all the cases studied. Nonetheless, the singular points identified in the flowfield were found to reposition with increasing shock strength. The separation node N_S was shifted upstream along the throat middle line towards the fin apices. Another observation is that the saddle points SP on both sides of the CS were found to move closer to the attachment node N_A. This could be due to the increasing flow deflection with respect to the shockwave angle β_0 and the enlargement of the centerplane separated region. The distance between the fin apex and the separation node denoted as L_{N_S} was measured and normalized by the undisturbed boundary layer thickness at the fin apex. These values are shown in Table 5.1.

Table 5.1: Location of the separation node from the fin apex.

M_∞	α_f (deg)	β_0 (deg)	L_{N_S} (m)	L_{N_S}/δ
4	7	19.63	0.041	8.9
4	9	21.34	0.022	4.8
4	11	23.15	0.011	2.4
4	13	25.06	0.005	1.1

The values of L_{N_S}/δ were then plotted against the fin leading-edge angle α_f and is shown in Fig. 5.5. It is evident from the figure that as the shock strength

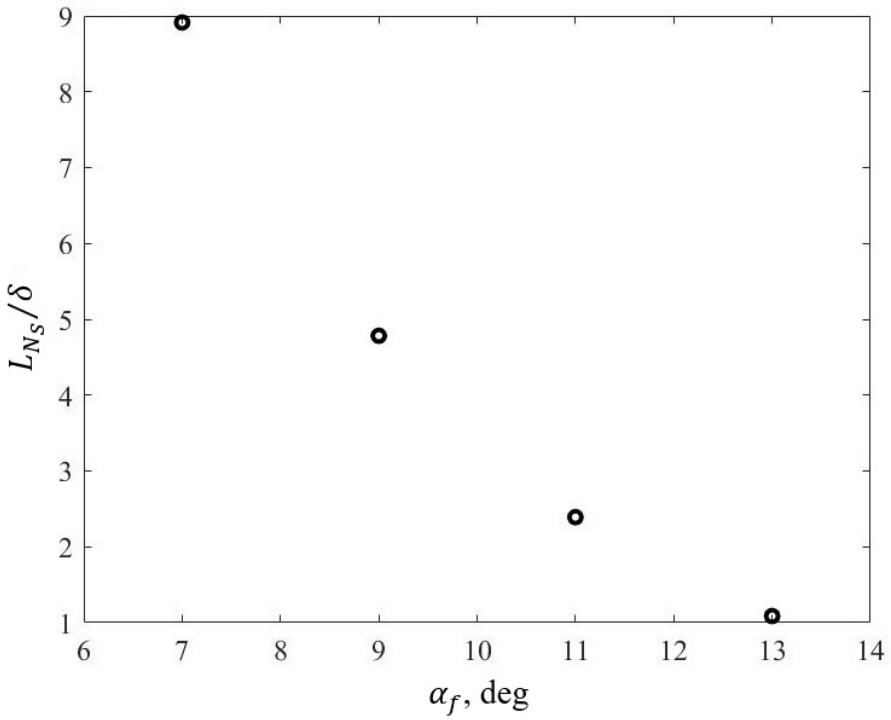

Figure 5.5: Location of the separation node plotted against the fin leading-edge angle

increases with α_f, the separation node moves upstream in the interaction region. Another observation is that the values of L_{N_S} follow a non-linear trend; however, more studies should be undertaken to develop a scaling law to identify the location

of the separation node by varying freestream Mach number M_∞ and the spanwise distance between the fin vertices. Based on these topological features, it can be understood that for stronger interactions, the spanwise width should be increased to avoid the occurrence of any flow blockage phenomenon.

5.1.3 Quasiconical Nature

Further discussion on the salient features will be made using Fig. 5.6 where the flowfield is visualized in the vicinity of the primary shock intersection at $M_\infty = 4$ and $\alpha_f = 7$ deg. Only half of the domain is shown in the figure since the interaction is

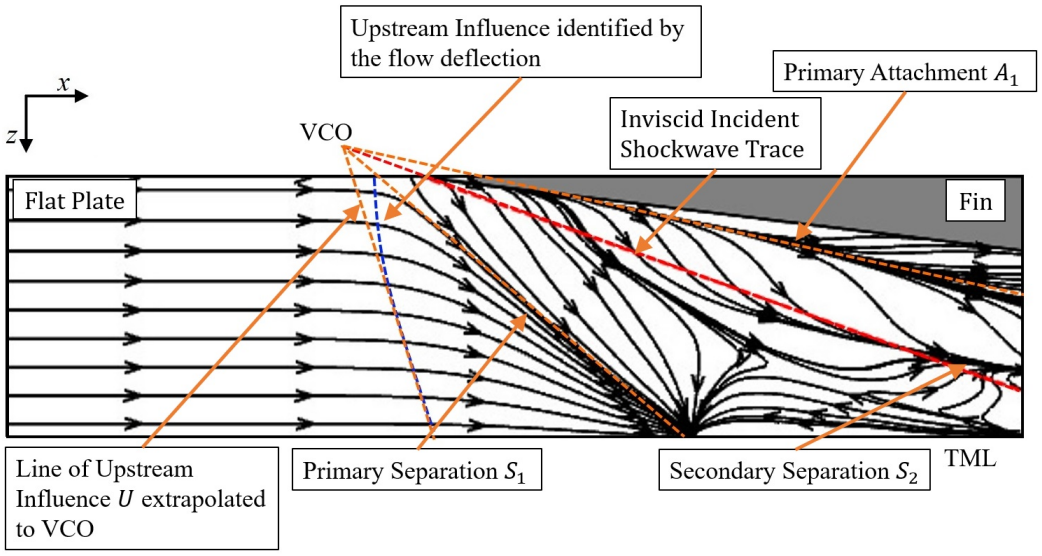

Figure 5.6: Computed surface flowfield of crossing shock interactions at $M_\infty = 4$ and $\alpha_f = 7$ deg

symmetrical about the throat centerplane. It has been established and also confirmed in the present study [141] that the flowfield resulting from single fin-induced interactions follows a quasiconical nature. Considering the crossing shock interactions as an

extension of the former, an examination of the resulting flowfield was conducted to study such a possibility. The lines of upstream influence U, primary separation S_1, and primary attachment A_1 were extrapolated along with the inviscid shockwave trace to a common point, VCO, upstream of the fin apex, as shown in the figure. Considering the symmetry, two such VCOs can be observed corresponding to the individual fin apices. The surface flow features were found to deviate from the quasiconical nature downstream of the flowfield because of the shock intersection. However, the surface pressure in the selected domain can be significantly influenced by the intersection of the shockwaves. Hence, an examination of the surface pressure distribution is necessary to confirm the quasiconical nature in crossing shock interactions. It can be noted that the extent of the upstream influence from the inviscid shock trace in laminar interactions is larger than turbulent ones. Hence, the deviation from the quasiconical nature in laminar interactions will occur earlier than in turbulent interactions and strongly depends on the span width. Upstream influence identified by the flow deflection is shown in the figure. The lines of secondary separation in single fin-induced interactions were found to follow the quasiconical nature. However, it is not the same in crossing shock interactions where S_2 is evidently distinct from that associated with S_1. This deviation can be attributed to the intersecting shockwaves that result in a significantly different flowfield downstream of the primary separation.

The digression from the quasiconical nature was observed in the present study with increasing values of fin leading-edge angle α_f. The increase in shock strength widens the centerplane separated region and results in a spanwise turn of the lines of primary separation, as shown in Fig. 5.4. It can be inferred from the surface flow features that the computational domain corresponding to individual fin-interactions in the present study is not wide enough to examine the quasiconical nature of the flowfield. Since the extent of the upstream influence in laminar interactions is larger

than that of turbulent interactions, the computational domain should be extended by increasing the distance between the fins to study the quasiconical nature.

5.1.4 Separated Flow Structures

The study of separated flow structures is essential in understanding the crossing shock interactions. The computed surface flow pattern exhibited a line of coalescence denoted as the line of primary separation extending the entire spanwise distance from one fin to the other. The flow downstream of this primary separation is rich in flow features as understood from the footprints on the flat plate surface. The principal features of the separated flow structure in the present investigation were studied in a similar manner as described by Gaitonde and Shang [37]. These features, known as "flow regimes," were categorized as the separated boundary layer, vortex interaction, centerline vortices, and entrainment flow [4, 37] and are shown in Fig. 5.7 using streamlines for $M_\infty = 4$ and $\alpha_f = 7$ deg. Only one side of the flow structure is shown for convenience, considering the interaction is symmetric. The computed surface flowfield is also shown in the figure using the 'white colored' limiting streamlines. The separated boundary layer (marked BL) lifted off from the surface along the line of primary separation, as shown in the figure. This regime does not reattach but, instead, forms an open separation moving downstream. The region of flow below this separated layer was occupied by the spanwise movement of fluid from various heights in the boundary layer near the fin apex. The flow attaching in the immediate downstream of the separated boundary layer was identified as the vortex interaction regime (marked VI) by Gaitonde et al. In the present case, the flow in this regime was found to fill the void left by the BL and moved spanwise to form a centerplane separated regime in the vicinity of the throat middle line, as shown in the figure. The structure of the centerplane separated region on the symmetry plane was shown

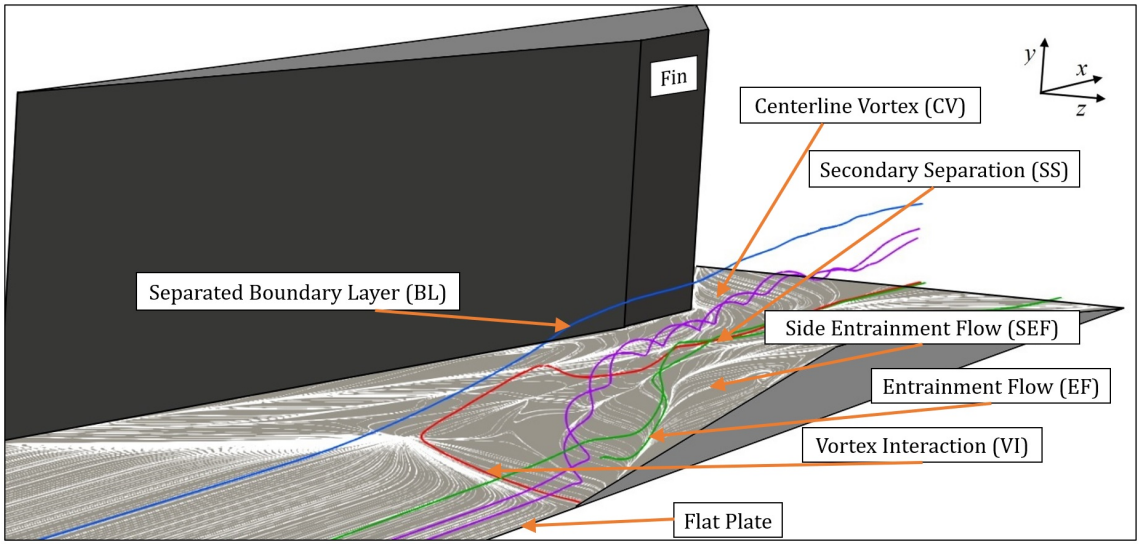

Figure 5.7: Separated flow structure of crossing shock interactions at $M_\infty = 4$ and $\alpha_f = 7$ deg. Limiting streamlines are indicated on the flat plate surface. Incoming flow direction is along the x axis

in Fig. 5.3. The flow from slightly higher locations in the boundary layer near the fin also moved spanwise towards the symmetry plane. The two streams of fluid from each fin were eventually turned in the streamwise direction to form a pair of centerline counter-rotating vortical structures (marked CV) moving downstream. Only one of the vortices is displayed in the figure, as mentioned before. This vortical structure is considered a principal feature of the crossing shock interactions and originates from a region very close to the fin leading edge. The centerline vortex regime remains distinct from the vortex interaction regime, as evident from the figure.

The fluid attaching further downstream on the line of primary attachment A_1 formed the entrainment flow (marked EF), which brings the high-momentum fluid near the flat plate surface. The flow in this regime occupied the region below the separated boundary layer and the vortex interaction. A sub-regime, identified as side entrainment flow (SEF), was observed by Thivet et al. [87] in turbulent interaction studies. This sub-regime is present in laminar interactions as well that constitute the

flow attaching at the A_1 and moving towards the fin. Side entrainment flow identified by the limiting streamlines diverging towards the fin surface is shown in the figure. Additionally, a secondary separated vortical structure (marked SS) is shown in the figure further downstream in the flowfield under the CV regime. When approaching the throat centerplane, the entrainment flow separates and further roll-up with the flow coming from the vortex interaction regime to form the SS regime. The footprint of this structure can be recognized using the lines of secondary separation and centerline attachment in Fig. 5.1.

5.2 Surface Pressure Distribution

The study of single fin-induced interactions discussed in Chapter 4 concluded that the resulting flowfield indicated a quasiconical free interaction. It was confirmed by the overlapping surface pressure distributions plotted against β. These plots were found to follow a universal form with a characteristic plateau and dip typical of separated interactions. As previously mentioned in the introduction, crossing shock interactions are considered an extension of single fin interactions. However, the surface flow visualization confirmed that the intersection of shockwaves could significantly alter the resulting flowfield.

A study was conducted by extrapolating the key flow features in the surface flow visualization for different fin angles. For the weakest interaction considered in the present study using fin angle $\alpha_f = 7$ deg at $M_\infty = 4$, the surface flow features were extrapolated to a common point upstream of the fin apex, known as VCO as shown in Fig. 5.6. An observation was made from the figure that the farfield region downstream of the fin apex is strongly influenced by the upstream influence of intersecting shockwaves and could result in a pressure rise. Thus, it is essential to examine the variation of surface pressure against the reduced angle $\beta - \beta_0$ at

different streamwise locations from the fin apex. The surface pressure distribution was normalized by the incoming freestream pressure and was plotted on a line normal to the inviscid shockwave induced by one of the fins (see Fig. 5.8). The streamwise locations were normalized by the undisturbed boundary-layer thickness at the fin apex. Inviscid pressure variation was also plotted and is shown using dashed line in the figure. A pressure rise is evident upstream of the inviscid shock location near the

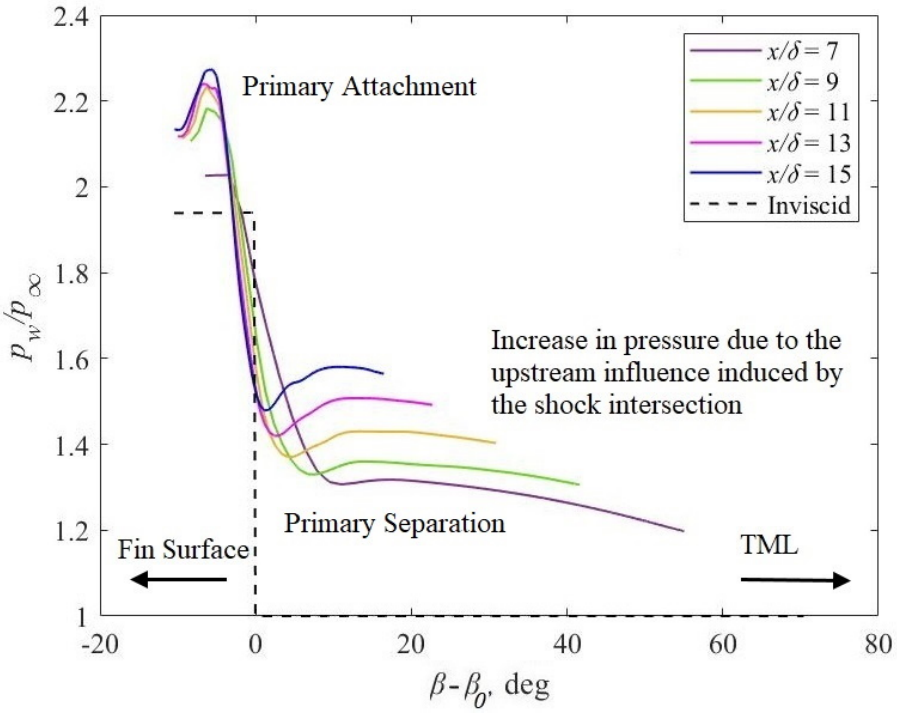

Figure 5.8: Surface pressure distribution on a plane normal to the shockwave at $M_\infty = 4$ and $\alpha_f = 7$ deg. Inviscid pressure variation shown using dashed lines

throat centerplane (identified by TML in the figure). As can be understood from the surface topology in Fig. 5.6, due to the more extensive upstream influence in laminar interactions comparing to turbulent counterpart, the locations considered in the figure are within the upstream influence region of the incident shockwave induced by the fin. Moreover, the pressure rise in the region is critically affected by the shock intersection.

This can be recognized by the increment in surface pressure ratio with x/δ. A pressure plateau in the immediate upstream of the incident inviscid shockwave corresponds to the primary separation, as shown in the figure. A peak pressure can be noticed downstream towards the fin surface and corresponds to the primary flow attachment. The examination of pressure distributions confirms the observation made earlier that the upstream pressure rise is significantly affected by the crossing shockwaves. Hence, it can be concluded that, due to the greater upstream extent in laminar interactions, the pressure rise near the throat centerplane is critically influenced by that induced by the fin-generated incident shockwave and the shock intersection.

Further, the surface pressure distribution was studied normal to the streamwise direction for the different fin angles. The resulting plots can be used to interpret the various topological features identified in surface flow visualization. Considering the case of $\alpha_f = 7$ deg, the spanwise surface pressure normalized by the incoming freestream pressure was plotted at different streamwise locations from the fin apex (see Fig. 5.9). These locations are normalized by the undisturbed boundary-layer thickness at the fin apex.

The variation of surface pressure downstream of the fin apex at $x/\delta = 4$ was found to have a surface plateau and peak on either side of the TML at $z = 0.035$ m. It can be seen from the plot that the surface pressure in the mid-span is greater than unity. As already discussed, this rise in pressure can be attributed to the intersecting shockwaves and the merging of upstream influence induced by individual fins. Further, the pressure values reach a plateau on both sides corresponding to the primary separation followed by a second more progressive increase in pressure close to the fins. The peak pressures correspond to the location of primary attachment A_1. Moving downstream, a rise in pressure can be found in the mid-span region at $x/\delta = 13$ because of the presence of a centerplane separated region. As mentioned

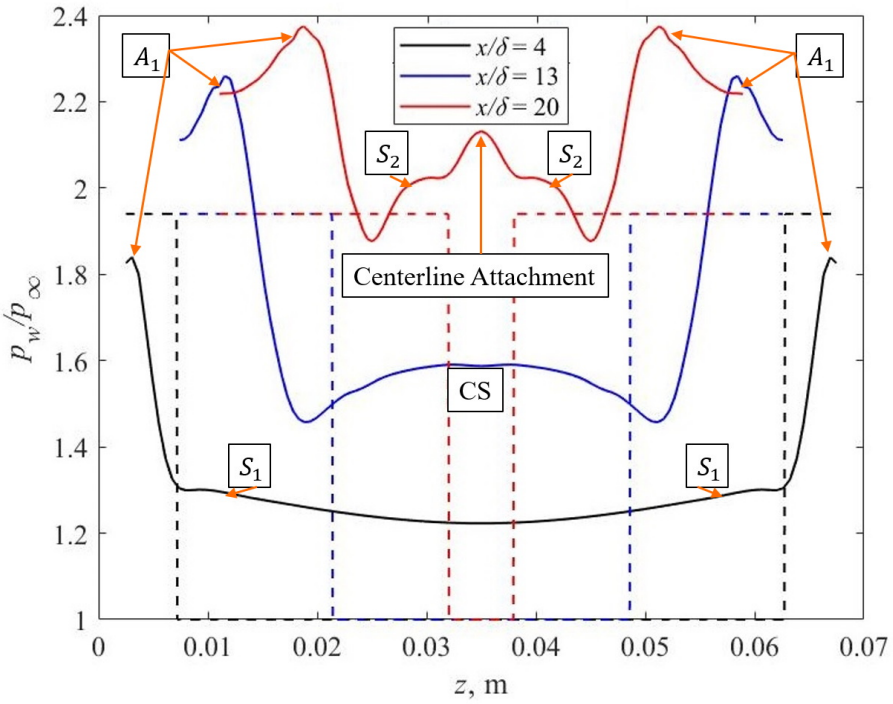

Figure 5.9: Spanwise surface pressure ratio at different streamwise locations. Inviscid pressure variation shown using dashed lines

previously, the location of the separation node was at $L_{N_S}/\delta \approx 9$ from the fin apex, which marks the beginning of the centerplane separated region. The presence of secondary separation and the centerline attachment is evident at $x/\delta = 20$ and can be understood by the pressure plateaus and peak pressure in the mid-span in the vicinity of $z = 0.035$ m. The peak pressures at the lines of primary attachment are visible at every location considered. Inviscid pressure jumps for all the cases are shown in the figure using dashed lines and are color-coded according to the streamwise locations. The pressure ratio at attachment was higher than the corresponding inviscid values as the flow moves downstream.

Nonetheless, the surface pressure downstream of the location of inviscid shock intersection at $x/\delta = 21$ was plotted and is shown in Fig. 5.10. The locations $x/\delta =$

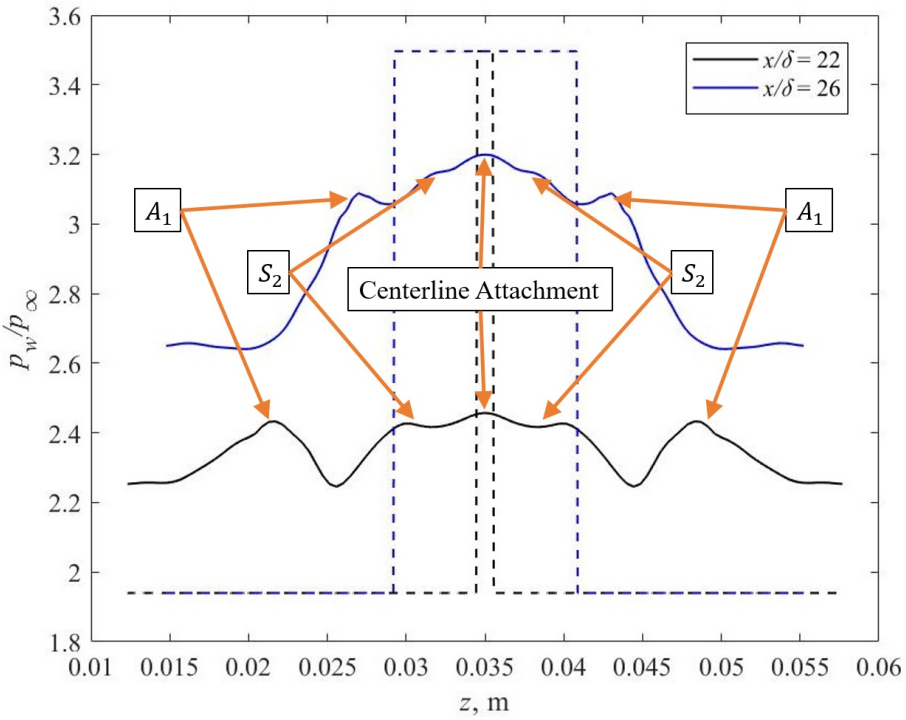

Figure 5.10: Spanwise surface pressure ratio at different streamwise locations. Inviscid pressure variation shown using dashed lines

22 and 26 were arbitrarily chosen to understand the nature of the flowfield beneath the reflected shockwaves. The mid-span plateau and peak variation in pressure indicate the secondary separated region near the throat middle line. As observed in the surface topology, the secondary separation and the centerline attachment approach each other as they move downstream, which is evident in the plots. However, the peak pressure corresponding to the centerline attachment was lower than the corresponding inviscid pressure jumps. This can be because of the viscous interaction at the throat centerplane due to the vortical structures generated by the individual fin interactions. The pressure peaks close to the fins are consistent with the lines of primary attachment converging towards the centerline moving downstream.

CHAPTER 6

CONCLUSIONS

Three-dimensional swept and cross shockwave/boundary-layer interactions were studied numerically using single fin-plate and double fin-plate configurations. Laminar interactions were considered in the present study for a better understanding of flow physics without the complications of turbulence and turbulence modeling. Grid independence studies were conducted to ensure that the flowfield is adequately resolved. The adverse pressure gradient due to the oblique shockwave generated by the fin was strong enough for boundary-layer separation in all the cases considered. In the first part, a single fin-generated, three-dimensional separation was investigated based on the flow topology. The presence of a separated vortical structure moving downstream was visualized, and the lines of separation and attachment were clearly visible from the surface topology results. The flow features downstream of the inception region were found to follow a quasiconical interaction similar to the results from turbulent flow studies. The lines of separation, attachment, and inviscid shockwave trace were extrapolated to a virtual conical origin upstream of the fin apex. Also, a stand-off distance from the line of upstream influence was observed at the fin apex due to the presence of an adverse pressure gradient. An upstream-influence scaling law developed for turbulent interactions was modified for laminar interactions and verified for a combination of Mach number, Reynolds number, and fin angle. The upstream-influence data from the present study was found to agree reasonably with the new scaling law. Multiple separated regions embedded in the primary separated region were confirmed using the surface flow visualizations and the surface pressure

distributions for the different cases studied. The quasiconical nature of fin-induced interactions was used to extend the free interaction theory, well established in two-dimensional flows, to three-dimensional, swept interactions in the present study. The universal, two-dimensional correlation function was expressed in terms of a normalized angle $\bar{\beta}$ and was plotted along a circular arc in the farfield region at $R_v/\delta = 38$ from the virtual conical origin. The resulting plots were found to follow the theoretical trend for the range of freestream Mach numbers and fin angles considered. The variation of normalized surface pressure p^* was plotted against the normalized angle β^* for all the cases studied and agreed well to the universal pressure distribution, which reinforced the concept of free interaction. In the second part, a numerical study was conducted to understand the interaction of a laminar boundary layer and crossing shockwaves generated by a pair of sharp unswept fins at $M_\infty = 4$ and $\alpha_f = 7$, 9, 11, and 13 deg. The key flow features and the singular points in the separated interactions were studied using surface flow visualization. A centerplane separated region was identified in the interaction region, followed by a secondary separated vortical structure in all the cases considered. Further, the flowfield was qualitatively compared with the turbulent crossing shock interaction studies to identify and discuss the separated flow regimes described by Gaitonde and Shang. The separated centerline vortical structures were visualized using streamlines. A study was conducted on the deviation of quasiconical symmetry in crossing shock interactions due to the large extent of upstream influence and the resulting pressure rise. Spanwise surface pressure distribution was studied at different streamwise locations to confirm the topological features and to interpret the nature of the flowfield moving downstream.

6.1 Literature Contributions

The research conducted has led to contributions to the following literature.

Journals

- J. J. Sebastian and F. K. Lu, "Upstream-Influence Scaling of Fin-Induced Laminar Shockwave/Boundary-Layer Interactions," *AIAA Journal*, Vol. 59, No. 5 (2021), pp. 1861-1864
- J. J. Sebastian and F. K. Lu, "Quasiconical Free Interaction in Fin-Induced Shock Wave/Laminar Boundary-Layer Interaction," *AIAA Journal*, Accepted (2021)

Conferences

- J. J. Sebastian and F. K. Lu, "Upstream-Influence Scaling of Fin-generated Shockwave/Laminar Boundary-layer Interactions," *AIAA Aviation Forum*, Virtual Event: AIAA Paper 2020-3009, June 2020
- J. J. Sebastian and F. K. Lu, "Free Interaction in Three-Dimensional, Laminar Shockwave/Boundary-Layer Interaction," *AIAA SciTech Forum*, Virtual Event, AIAA Paper 2021-0490, January 2021
- J. J. Sebastian and F. K. Lu, "Numerical Investigation of Separated Flowfield in a Crossing Shockwave/ Laminar Boundary-Layer Interaction," *AIAA SciTech Forum*, Abstract Submitted, January 2022

It is anticipated that the research findings will result in a number of additional publications. Anticipated topics include (but are not limited to):

- Tertiary flow separation in laminar fin-induced SBLI (paper under preparation)
- Flowfield of a laminar double fin-induced crossing shock interactions

6.2 Recommendations for Future Work

Fundamental studies in laminar crossing shock interactions are limited and the physical understanding of the flowfield is yet to be uncovered completely. The flowfield resulting from the separated cross SBLIs shows that there are certain parameters

that might seriously alter the flow features. These parameters include the freestream Mach and Reynolds numbers, the incoming boundary layer, the fin leading-edge angles, the distance between the fin vertices, and the minimum distance between the fins (throat width). In the present study, only the fin angle was varied to understand the interaction. Further studies are required to uncover the effects of these parameters on the flow structures. An increase in span width could result in a region of quasi-conical symmetry in weak interactions before deviating near the shock intersection. The present study was performed using a symmetric double fin-plate configuration. Further studies are required to study a possible symmetry breaking by introducing disturbances in the flowfield. Additionally, asymmetric configurations can be studied by using fins with different angles mounted on a flat plate.

APPENDIX A

Surface-Flow Visualization in Fin-Induced Laminar Swept SBLI

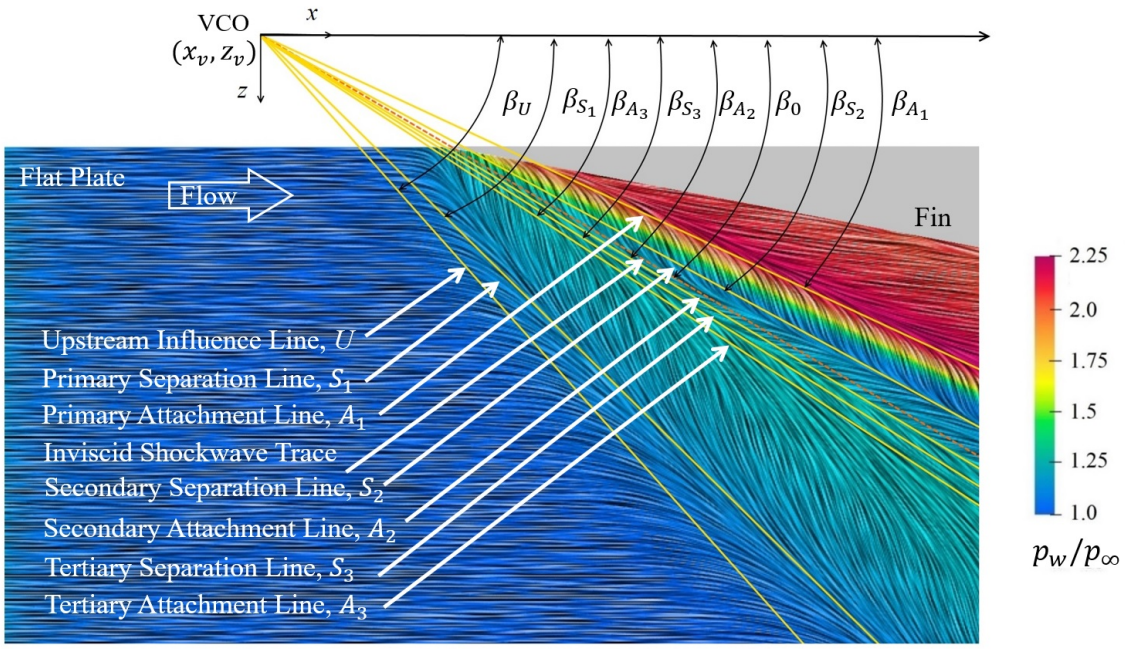

Figure A.1: Pressure contour of the surface flowfield and the location of the virtual conical origin at $M_\infty = 2.64$, $\alpha_f = 10$ deg

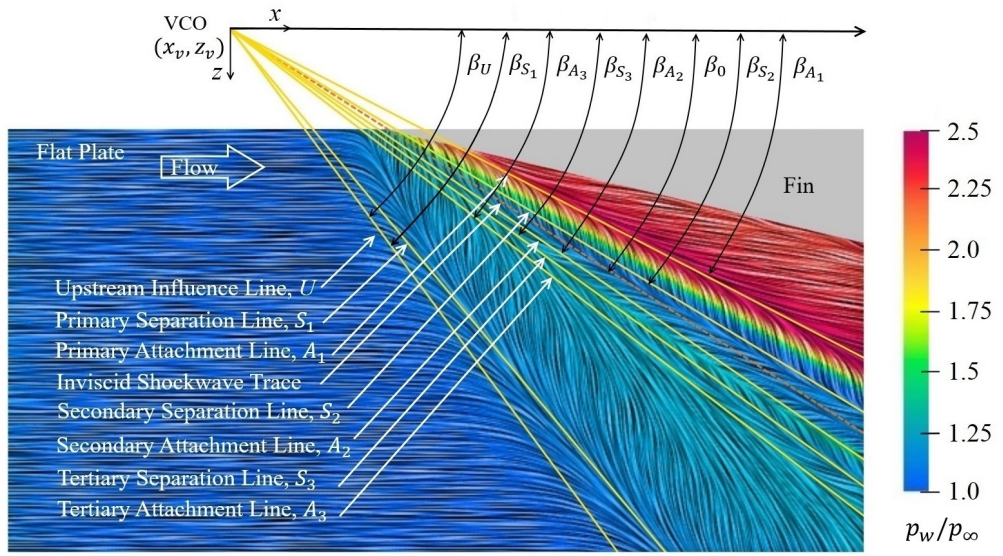

Figure A.2: Pressure contour of the surface flowfield and the location of the virtual conical origin at $M_\infty = 2.64$, $\alpha_f = 13$ deg

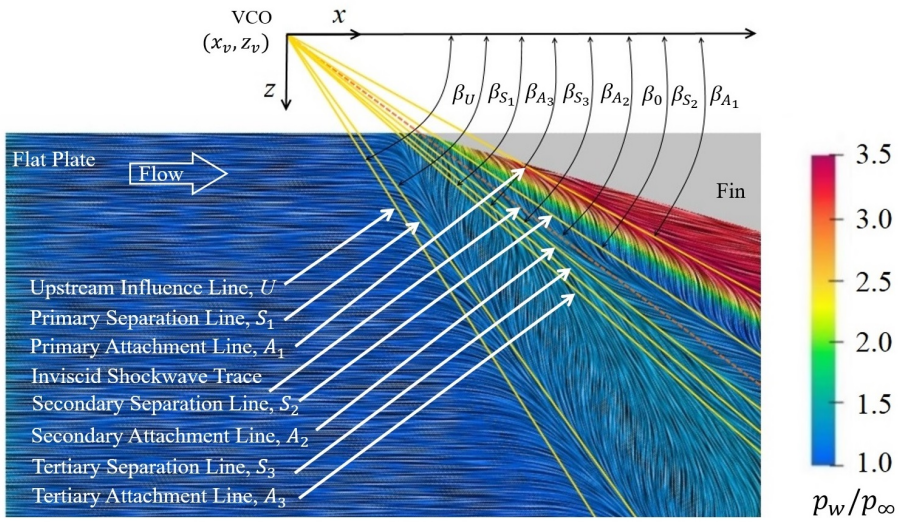

Figure A.3: Pressure contour of the surface flowfield and the location of the virtual conical origin at $M_\infty = 2.64$, $\alpha_f = 16$ deg, $Re_\delta = 3053$

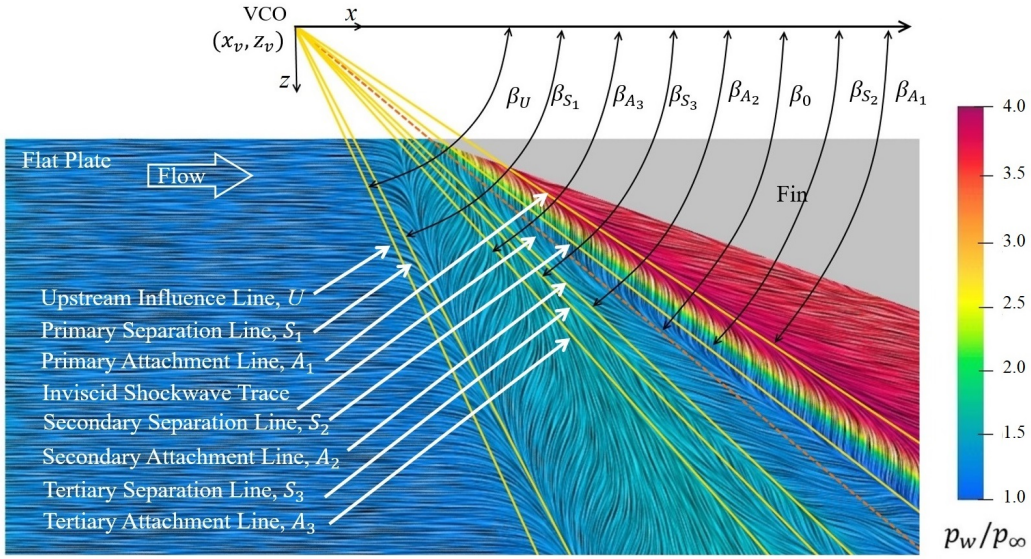

Figure A.4: Pressure contour of the surface flowfield and the location of the virtual conical origin at $M_\infty = 2.64$, $\alpha_f = 19$ deg

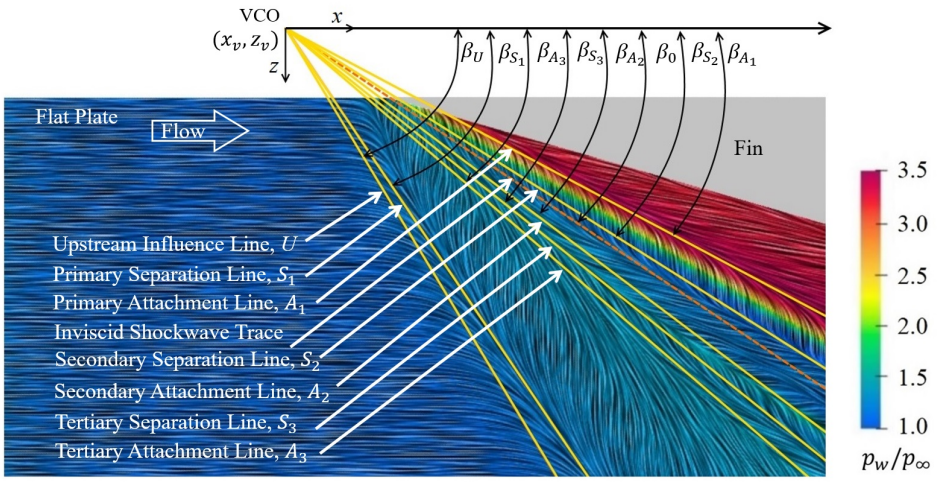

Figure A.5: Pressure contour of the surface flowfield and the location of the virtual conical origin at $M_\infty = 2.95$, $\alpha_f = 16$ deg

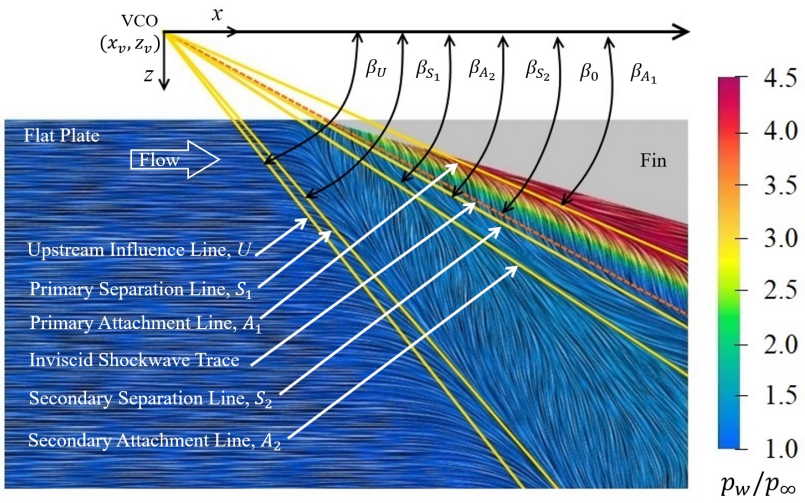

Figure A.6: Pressure contour of the surface flowfield and the location of the virtual conical origin at $M_\infty = 3.93$, $\alpha_f = 16$ deg

APPENDIX B

Surface-Pressure Distribution in Fin-Induced Laminar SBLI at Different Fin Angles

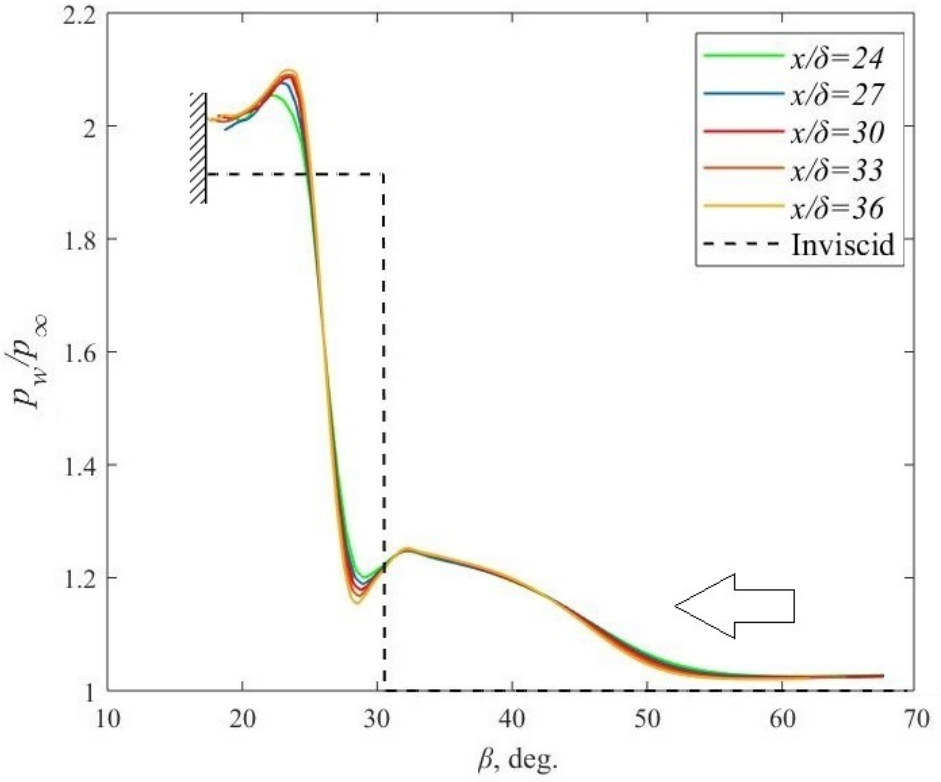

Figure B.1: Surface pressure distribution on a plane normal to the shockwave at $M_\infty = 2.64$, $\alpha_f = 10$ deg

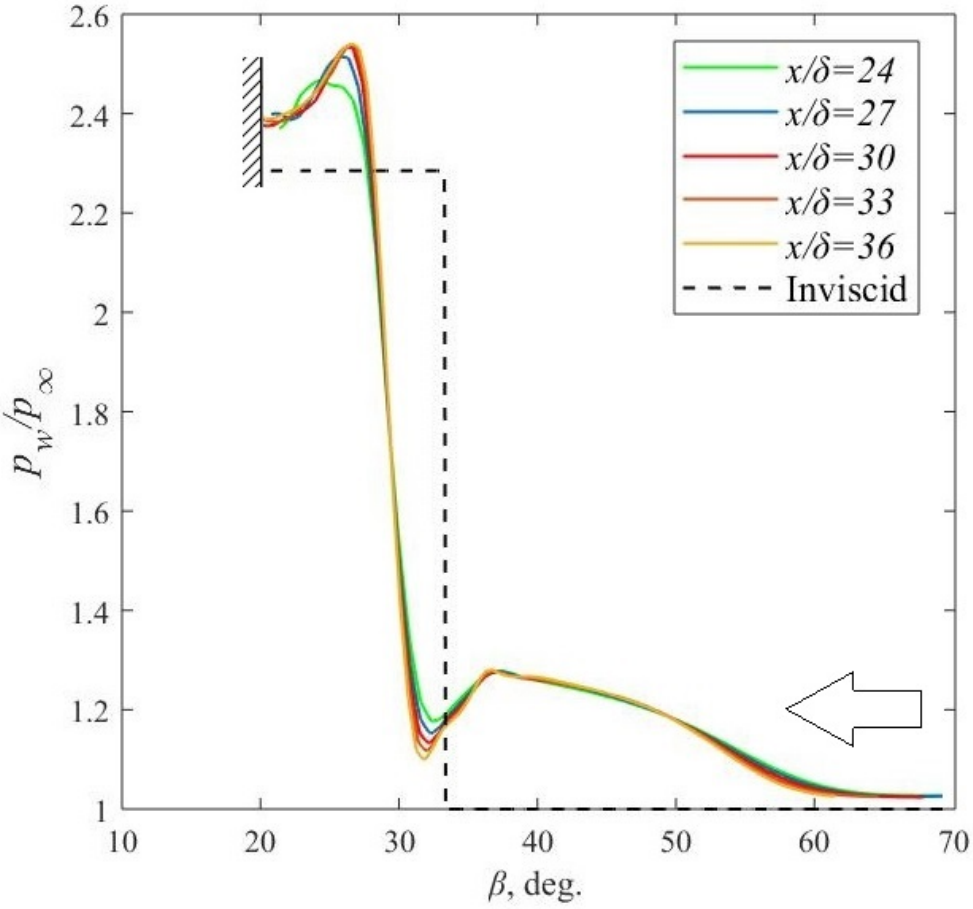

Figure B.2: Surface pressure distribution on a plane normal to the shockwave at $M_\infty = 2.64$, $\alpha_f = 13$ deg

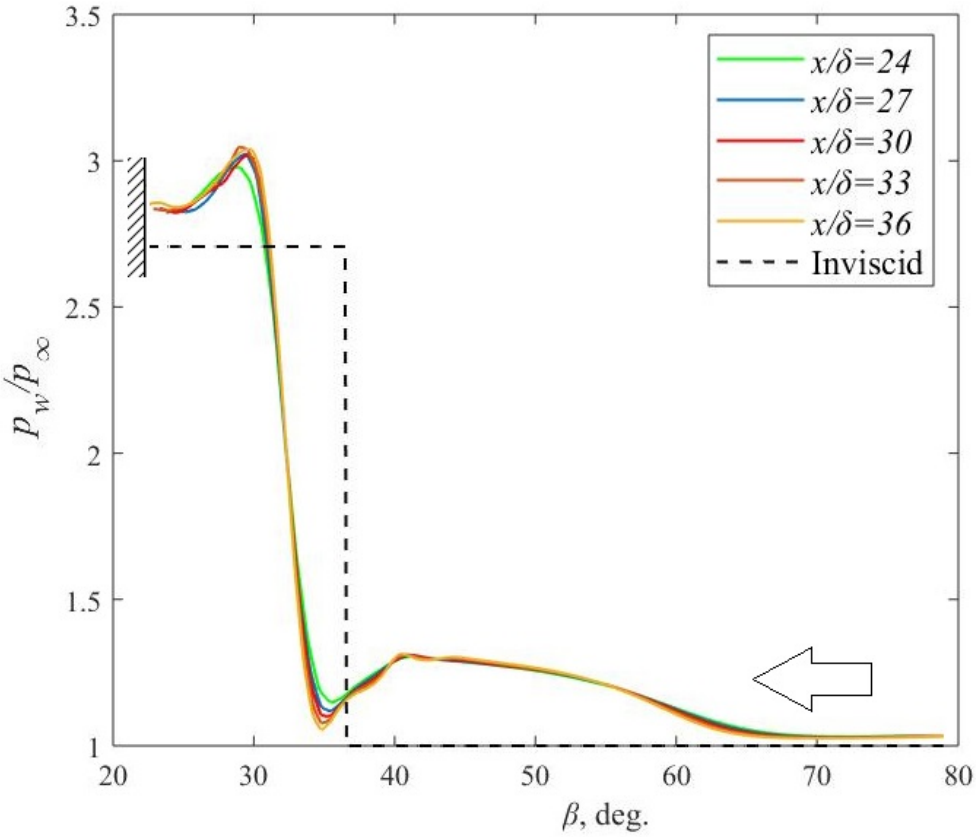

Figure B.3: Surface pressure distribution on a plane normal to the shockwave at $M_\infty = 2.64$, $\alpha_f = 16$ deg, $Re_\delta = 3053$

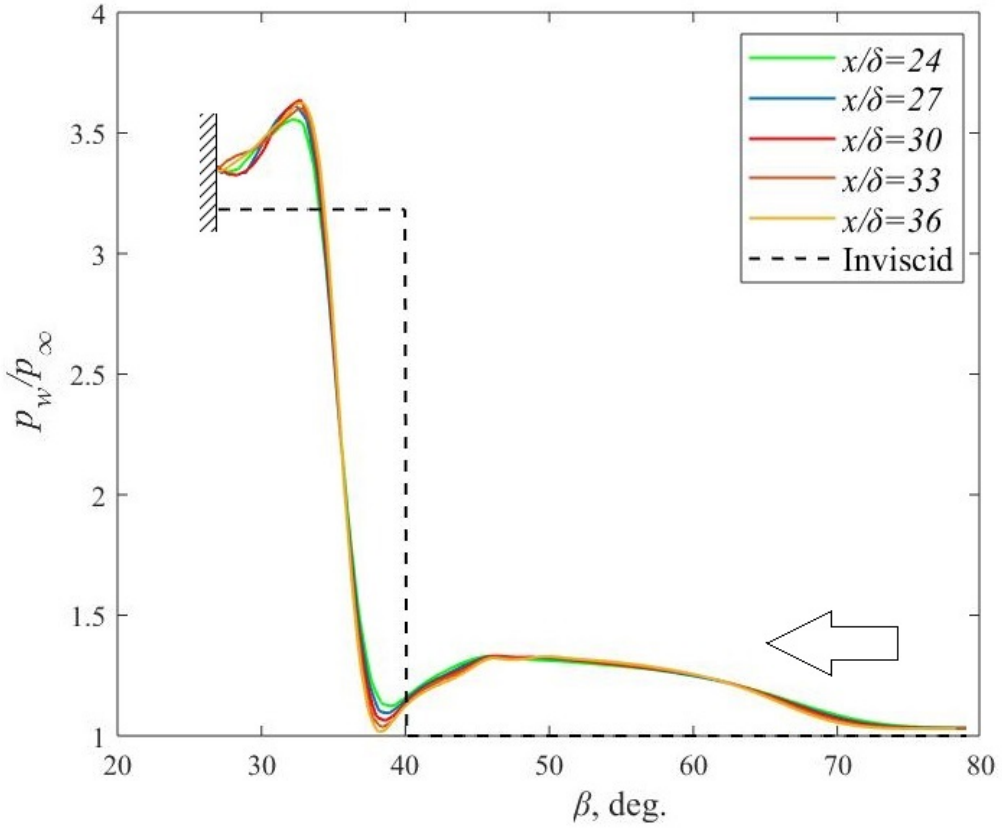

Figure B.4: Surface pressure distribution on a plane normal to the shockwave at $M_\infty = 2.64$, $\alpha_f = 19$ deg

APPENDIX C

Surface-Flow Visualization in Double Fin-Induced Laminar Crossing SBLI at Different Fin Angles

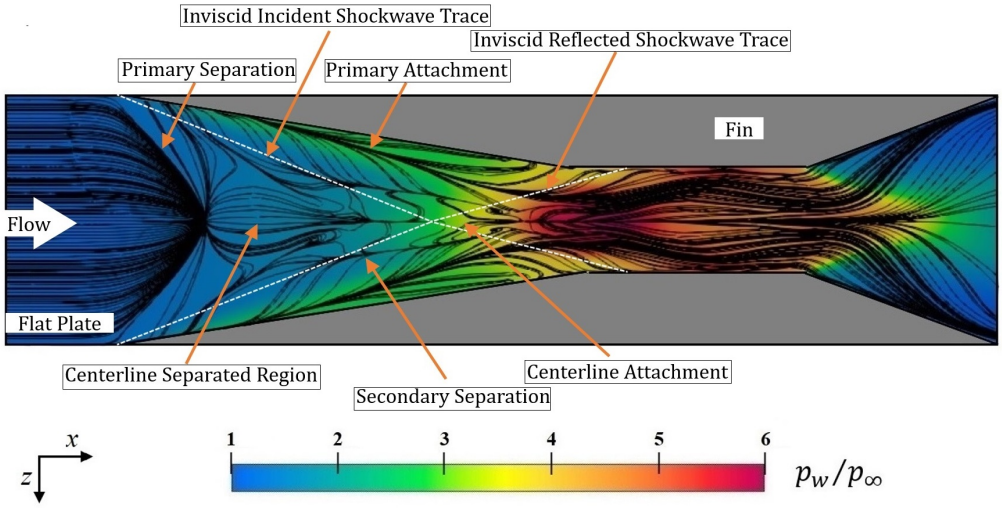

Figure C.1: Surface flow topology with pressure variation for crossing shock interaction at $M_\infty = 4$ and $\alpha_f = 9$ deg

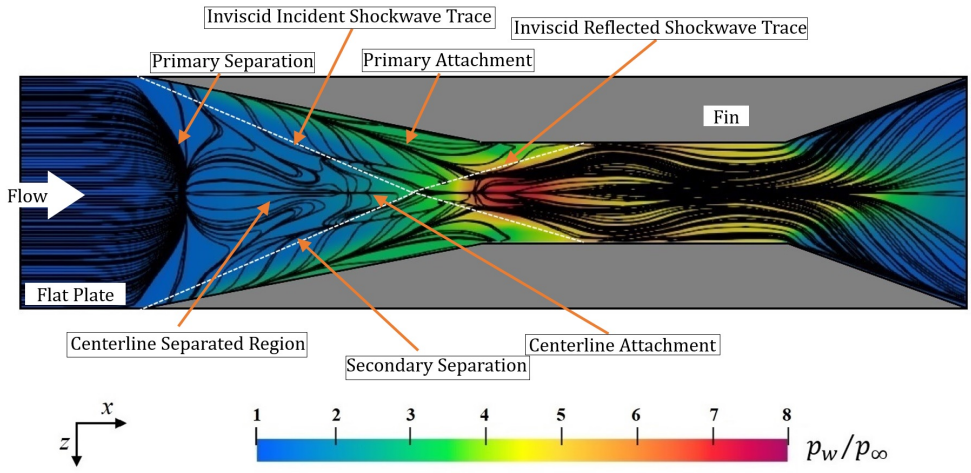

Figure C.2: Surface flow topology with pressure variation for crossing shock interaction at $M_\infty = 4$ and $\alpha_f = 11$ deg

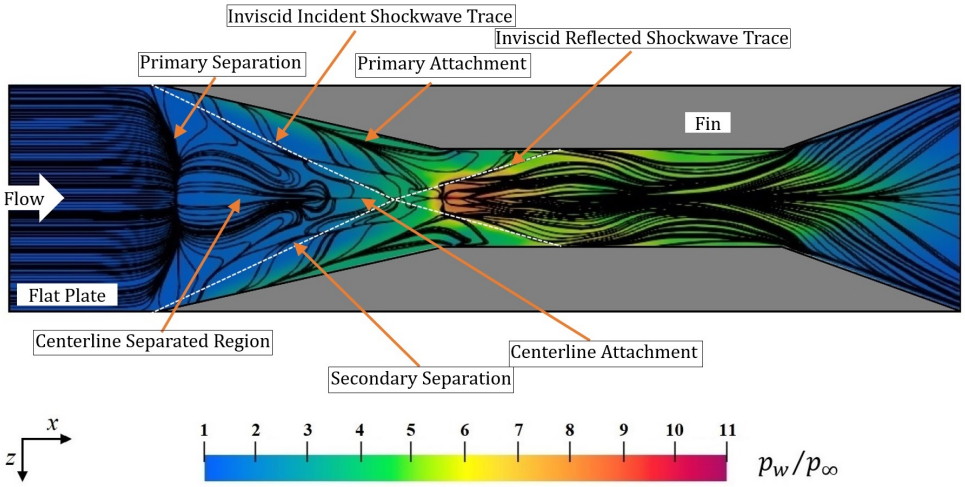

Figure C.3: Surface flow topology with pressure variation for crossing shock interaction at $M_\infty = 4$ and $\alpha_f = 13$ deg

APPENDIX D

Separated Flow Regimes in Cross Fin-Induced Laminar SBLI at Different Fin Angles

The flow regimes were computed for different fin leading-edge angles studied for crossing shock interactions. The separated structures in the case of $\alpha_f = 9$ deg were found to be similar to the 7 deg case already discussed in Chapter 5 (see Fig. D.1). However, it was found that the separated boundary layer merged with the centerline

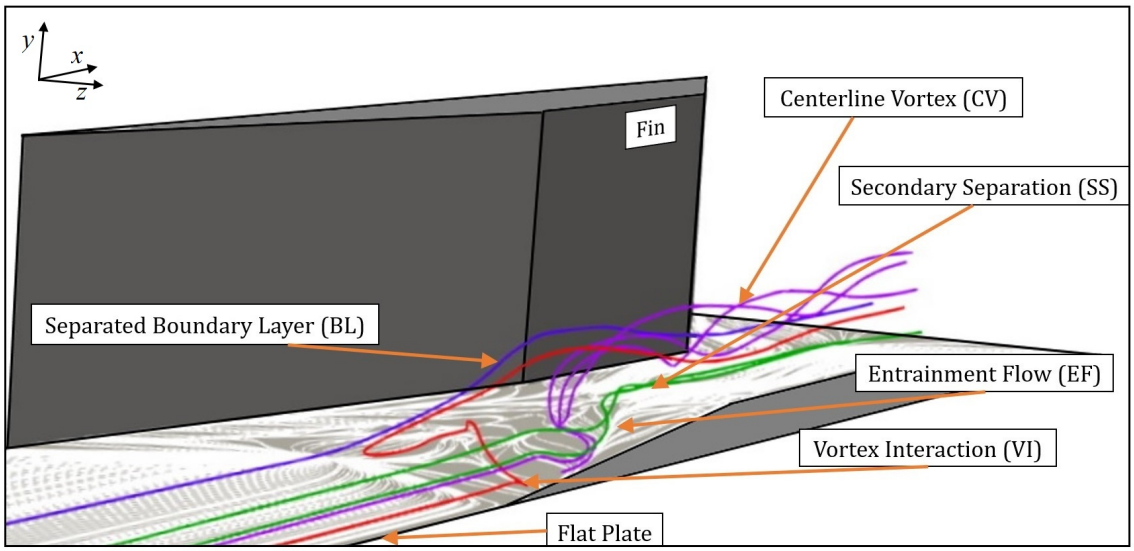

Figure D.1: Separated flow structure of crossing shock interactions at $M_\infty = 4$ and $\alpha_f = 9$ deg. Limiting streamlines are indicated on the flat plate surface. Incoming flow direction is along the x axis

vortical structure far downstream from the fin apex. The vortex interaction regime in the immediate downstream of the primary separation was found to separate at the centerplane separated region. The secondary separated vortical structures were also evident in the figure. Nonetheless, as the shock strength increases, the merging of separated boundary layer with the centerplane separated vortical structures happened earlier than in the case of lower α_f studied (see Figs. D.2, D.3).

The secondary separated vortical structure, however, was found to exist only for an abridged length in the far downstream of the interaction flowfield. This phenomenon can be attributed to the computational geometry considered. Since the

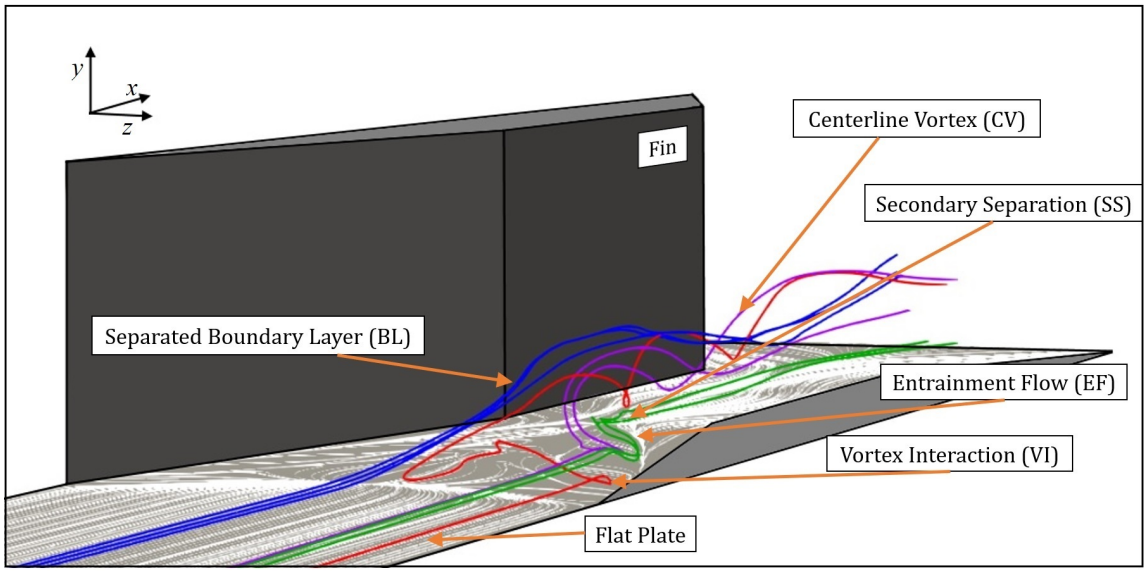

Figure D.2: Separated flow structure of crossing shock interactions at $M_\infty = 4$ and $\alpha_f = 11$ deg. Limiting streamlines are indicated on the flat plate surface. Incoming flow direction is along the x axis

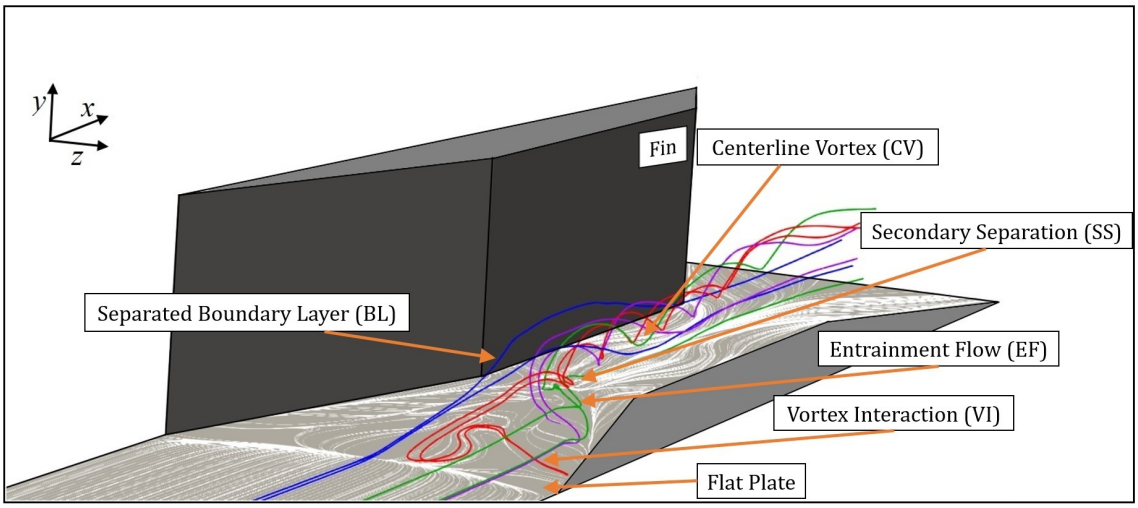

Figure D.3: Separated flow structure of crossing shock interactions at $M_\infty = 4$ and $\alpha_f = 13$ deg. Limiting streamlines are indicated on the flat plate surface. Incoming flow direction is along the x axis

width of the throat was fixed in the present study, the length of the converging section of the fins identified by L_c in Fig. 3.18 decreased with increasing fin leading-edge angle. Hence, the location of secondary separated structures occurred near the exit

of the converging domain where the flow experiences expansion waves and reflected shockwaves. Further studies are required to understand the flowfield far downstream of the primary interaction.

APPENDIX E

Surface-Pressure Distribution in Double Fin-Induced Laminar SBLI at Different Fin Angles

The spanwise pressure distribution at different streamwise locations for $\alpha_f = 9, 11$ and 13 deg are shown here. The locations were selected such that the pressure variation due to the topological features was properly captured. The upstream propagation of the different flow features with the increasing shock strength can be understood from the selected streamwise locations. Further studies are required to study the flow phenomena further downstream of the crossing shock intersection. The key flow features are annotated in the figures.

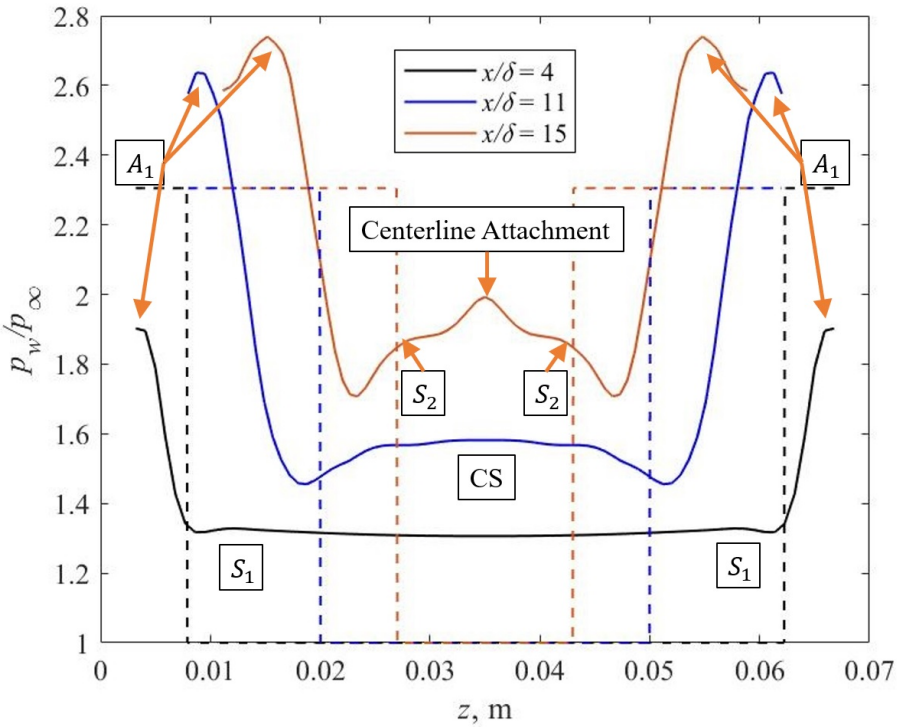

Figure E.1: Surface pressure distribution for different streamwise locations at $M_\infty = 4$, $\alpha_f = 9$ deg. Inviscid pressure variation shown using dashed lines

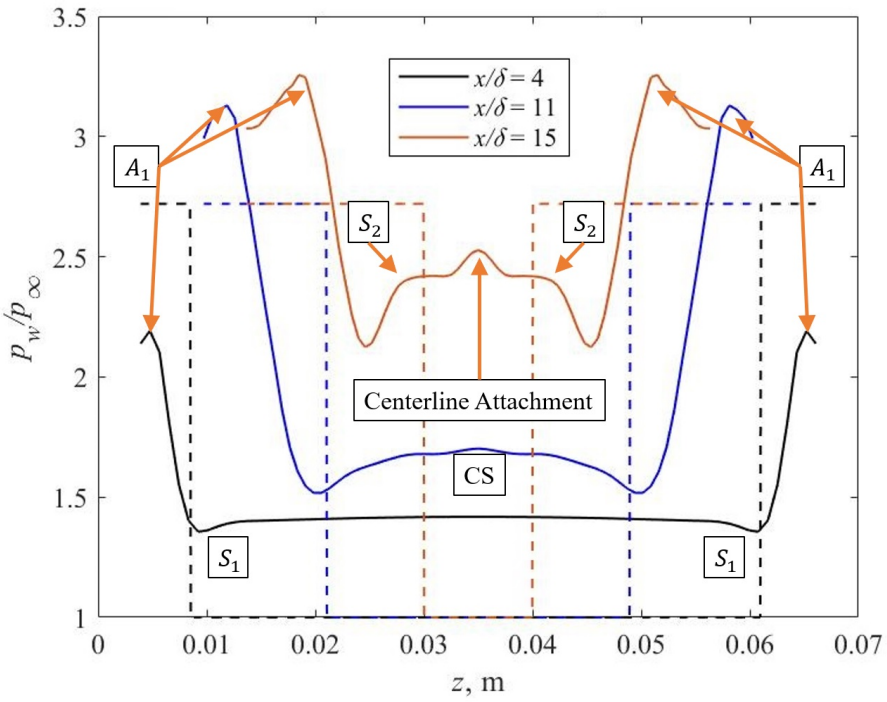

Figure E.2: Surface pressure distribution for different streamwise locations at $M_\infty = 4$, $\alpha_f = 11$ deg. Inviscid pressure variation shown using dashed lines

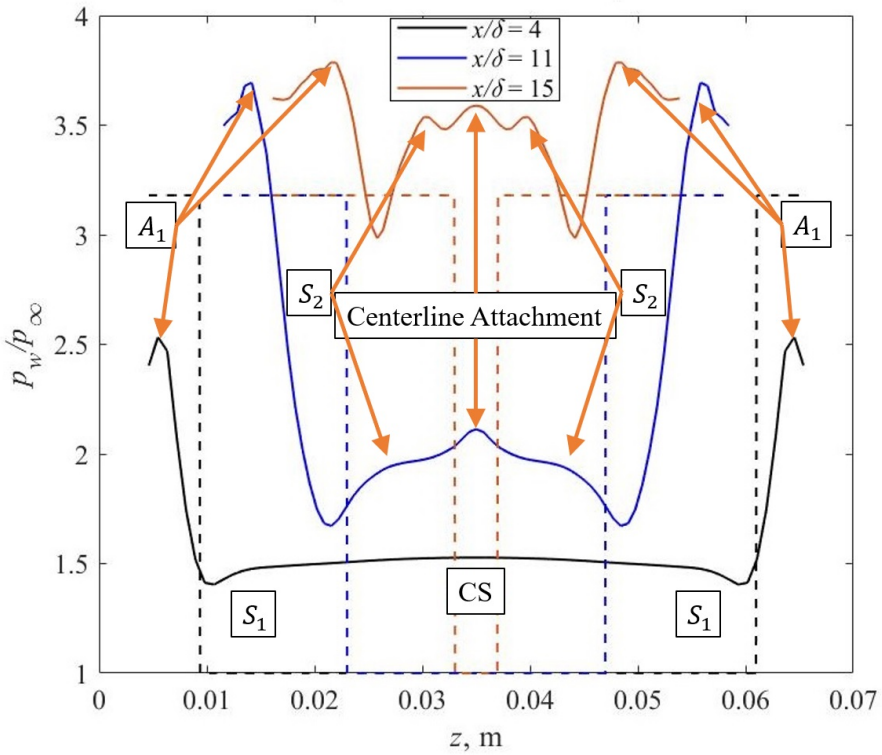

Figure E.3: Surface pressure distribution for different streamwise locations at $M_\infty = 4$, $\alpha_f = 13$ deg. Inviscid pressure variation shown using dashed lines

REFERENCES

[1] D. D. Knight and A. A. Zheltovodov, in *Shock Wave-Boundary-Layer Interactions*, H. Babinsky and J. K. Harvey, Eds. New York: Cambridge, 2011, ch. 4.

[2] N. Narayanswami, C. C. Horstman, and D. D. Knight, "Computation of Crossing Shock/Turbulent Boundary Layer Interaction at Mach 8.3," *AIAA Journal*, vol. 31, no. 8, pp. 1369–1376, 1993.

[3] T. J. Garrison and G. S. Settles, "Flowfield Visualization of Crossing Shockwave/ Boundary Layer Interactions," AIAA Paper 92–0750, 1992.

[4] D. Gaitonde, J. S. Shang, and M. Visbal, "Structure of a Double-Fin Turbulent Interaction at High Speed," *AIAA Journal*, vol. 33, no. 2, pp. 193–200, 1995.

[5] A. Salin, Y. Yao, and A. A. Zheltovodov, "Flow Topology and Secondary Separation Modelling at Crossing Shock Wave/Turbulent Boundary Layer Interaction Conditions," *International Journal of Aerospace Innovations*, vol. 4, pp. 13–27, 2012.

[6] P. J. Lamont and B. L. Hunt, "The Impingement of Underexpanded Axisymmetric Jets on Perpendicular and Inclined Flat Plates," *Journal of Fluid Mechanics*, vol. 100, no. 3, pp. 471–511, 1980.

[7] J. M. Délery and J. G. Marvin, "Shock-Wave Boundary-Layer Interactions," in *AGARD*, no. 280, 1986.

[8] A. Ferri, "Experimental Results With Airfoils Tested in the High-Speed Tunnel at Guidonia," NACA TM-946, 1940.

[9] H. W. Liepmann, "The Interaction Between Boundary Layer and Shock Waves in Transonic Flow," *Journal of the Aeronautical Sciences*, vol. 13, pp. 623–637, 1946.

[10] J. Ackeret, F. Feldmann, and N. Rott, "Investigations of Compression Shocks and Boundary Layers in Gases Moving at High Speed," NACA TM-1113, 1947.

[11] K. Oswatitsch and K. Wieghardt, "Theoretical Analysis of Stationary Potential Flows and Boundary Layers at High Speed," NACA TM-1189, 1948.

[12] R. H. Korkegi, "Survey of Viscous Interactions Associated with High Mach Number Flight," *AIAA Journal*, vol. 9, no. 5, pp. 771–784, 1971.

[13] D. V. Gaitonde, "Progress in Shock Wave/Boundary-Layer Interactions," *Progress in Aerospace Sciences*, vol. 72, pp. 80–99, 2015.

[14] T. C. Adamson and A. F. Messiter, "Analysis of Two-Dimensional Interactions Between Shock Waves and Boundary Layers," *Annual Review of Fluid Mechanics*, vol. 12, pp. 103–138, 1980.

[15] B. Edney, "Anomalous Heat Transfer and Pressure Distributions on Blunt Bodies at Hypersonic Speeds in the Presence of an Impinging Shock," The Aeronautical Research Institute of Sweden, Stockholm, Sweden, FFA Report 115, 1968.

[16] M. J. Lighthill, "On Boundary Layers and Upstream Influence. I. A Comparison between Subsonic and Supersonic Flows," *Proceedings of the Royal Society. A, Mathematical, Physical, and Engineering Sciences*, vol. 217, no. 1130, pp. 344–357, 1953.

[17] ——, "On Boundary Layers and Upstream Influence. II. Supersonic Flows without Separation," *Proceedings of the Royal Society. A, Mathematical, Physical, and Engineering Sciences*, vol. 217, no. 1131, pp. 478–507, 1953.

[18] D. R. Chapman, D. M. Kuehn, and H. K. Larson, "Investigation of Separated Flows in Supersonic and Subsonic Streams with Emphasis on the Effect of Transition," NACA TN-3869, 1957.

[19] M. Tobak and D. J. Peake, "Topology of Three-Dimensional Separated Flows," *Annual Review of Fluid Mechanics*, vol. 14, pp. 61–85, 1982.

[20] J. E. Green, "Interactions Between Shock Waves and Turbulent Boundary Layers," *Progress in Aerospace Sciences*, vol. 11, pp. 235–340, 1970.

[21] A. G. Panaras, "Review of the Physics of Swept-Shock/Boundary-Layer Interactions," *Progress in Aerospace Sciences*, vol. 32, no. 2-3, pp. 173–244, 1996.

[22] W. R. Sears, "The Boundary Layer of Yawed Cylinders," *Journal of the Aeronautical Sciences*, vol. 15, no. 1, pp. 49–52, 1948.

[23] S. N. Brown and L. Howarth, "Singularities Associated with Separating Boundary Layers," *Philosophical Transactions of the Royal Society of London. Series A, Mathematical and Physical Sciences*, vol. 257, no. 1084, pp. 409–444, 1965.

[24] R. Legendre, "Lignes de courant d'un écoulement continu," *La Recherche Aérospatiale*, no. 105, pp. 3–9, 1965.

[25] M. J. Lighthill, "Attachment and Separation in Three-Dimensional Flow," in *Laminar Boundary Layers*, L. Rosenhead, Ed. London: Oxford, 1963, pp. 72–82.

[26] E. Maskell, "Flow Separation in Three-Dimensions," Royal Aeronautical Establishment, Farnborough, U.K., RAE Report 2565, 1955.

[27] F. K. Lu, "Quasiconical Free Interaction Between a Swept Shock and a Turbulent Boundary-Layer," *AIAA Journal*, vol. 31, no. 4, pp. 686–692, 1993.

[28] G. S. Settles and S. M. Bogdonoff, "Scaling of Two- and Three-Dimensional Shock/Turbulent Boundary-Layer Interactions at Compression Corners," *AIAA Journal*, vol. 20, no. 6, pp. 782–789, 1982.

[29] G. S. Settles and R. L. Kimmel, "Similarity of Quasiconical Shock Wave/Turbulent Boundary-Layer Interactions," *AIAA Journal*, vol. 24, no. 1, pp. 47–53, 1986.

[30] G. S. Settles and F. K. Lu, "Conical Similarity of Shock/Boundary-Layer Interactions Generated by Swept and Unswept Fins," *AIAA Journal*, vol. 23, no. 7, pp. 1021–1027, 1985.

[31] G. R. Inger, "Spanwise Propagation of Upstream Influence in Conical Swept Shock/Boundary-Layer Interactions," *AIAA Journal*, vol. 25, no. 2, pp. 287–293, 1987.

[32] F. K. Lu and G. S. Settles, "Inception Length to a Fully Developed, Fin-Generated, Shock-Wave, Boundary-Layer Interaction," *AIAA Journal*, vol. 29, no. 5, pp. 758–762, 1991.

[33] M. C. Adler and D. V. Gaitonde, "Flow Similarity in Strong Swept-Shock/Turbulent-Boundary-Layer Interactions," *AIAA Journal*, vol. 57, no. 4, pp. 1579–1593, 2019.

[34] N. Arora, M. Y. Ali, Y. Zhang, and F. S. Alvi, "Flowfield Measurements in a Mach 2 Fin-Generated Shock/Boundary-Layer Interaction," *AIAA Journal*, vol. 56, no. 10, pp. 3963–3974, 2018.

[35] D. D. Knight, "Numerical Simulation of 3-D Shock Wave Turbulent Boundary Layer Interactions," in *Special Course on Shock Wave/Boundary-Layer Interactions in Supersonic and Hypersonic Flows*. AGARD Report 792, August 1993.

[36] J. D. Schmisseur and D. V. Gaitonde, "Numerical Investigation of Strong Crossing Shock-Wave/ Turbulent Boundary-Layer Interactions," *AIAA Journal*, vol. 39, no. 9, pp. 1742–1749, 2001.

[37] D. Gaitonde and J. S. Shang, "Structure of a Turbulent Double-Fin Interaction at Mach 4," *AIAA Journal*, vol. 33, no. 12, pp. 2250–2258, 1995.

[38] A. A. Zheltovodov, A. Maksimov, D. Gaitonde, M. Visbal, and J. S. Shang, "Experimental and Numerical Study of Symmetric Interaction of Crossing Shocks and Expansion Waves with a Turbulent Boundary Layer," *Thermophysics and Aeromechanics*, vol. 7, no. 2, pp. 155–172, 2000.

[39] N. Narayanswami, D. D. Knight, S. M. Bogdonoff, and C. C. Horstman, "Interaction Between Crossing Oblique Shocks and a Turbulent Boundary Layer," *AIAA Journal*, vol. 30, pp. 1945–1952, 1992.

[40] N. Narayanswami, D. D. Knight, and C. C. Horstman, "Investigation of a Hypersonic Crossing Shock Wave/Turbulent Boundary Layer Interaction," *Shock Waves*, vol. 3, pp. 35–48, 1993.

[41] L. F. Henderson, "The Reflexion of a Shock-Wave at a Rigid Wall in the Presence of a Boundary Layer," *Journal of Fluid Mechanics*, vol. 30, no. 4, pp. 699–722, 1967.

[42] W. B. Sturek and J. E. Danberg, "Supersonic Turbulent Boundary Layer in Adverse Pressure Gradient. Part I: The Experiment," *AIAA Journal*, vol. 10, no. 4, pp. 475–480, 1972.

[43] ——, "Supersonic Turbulent Boundary Layer in Adverse Pressure Gradient. Part II: Data Analysis," *AIAA Journal*, vol. 10, no. 5, pp. 630–635, 1972.

[44] F. W. Spaid and J. C. Frishett, "Incipient Separation of a Supersonic, Turbulent Boundary Layer, Including Effects of Heat Transfer," *AIAA Journal*, vol. 10, no. 7, pp. 915–922, 1972.

[45] T. Cebeci and P. Bradshaw, *Physical and Computational Aspects of Convective Heat Transfer*. New York: Springer, 1984.

[46] G. S. Settles, "An Experimental Study of Compressible Turbulent Boundary-layer Separation at High Reynolds Number." Ph. D. Dissertation, Princeton University, 1975.

[47] J. M. Délery and J. C. Le Balleur, "Boundary Layer Effects in Turbomachines," AGARD 164, 1972.

[48] J. Délery, "ONERA Research on Afterbody Viscous/Inviscid Interactions with Special Emphasis on Base Flow Problems," in *Symposium on Rocket/Plume Fluid Dynamics Interactions*, Huntsville, Alabama, 1983.

[49] K. Stewartson and P. G. Williams, "Self-Induced Separation," vol. 312, pp. 181–206, 1969.

[50] V. Y. Neiland, "Theory of Laminar Boundary Layer Separation in Supersonic Flow," *Fluid Dynamics*, vol. 4, no. 4, pp. 33–35, 1969.

[51] W. L. Hankey and M. S. Holden, "Two-Dimensional Shock Wave-Boundary Layer Interactions in High Speed Flows," AGARD Report 203, 1975.

[52] J. M. Delery, "Shock Wave/Turbulent Boundary Layer Interaction and Its Control," *Progress in Aerospace Sciences*, vol. 22, no. 4, pp. 209–280, 1985.

[53] G. S. Settles and D. S. Dolling, "Swept Shock Wave/Boundary-Layer Interactions," in *Tactical Missile Aerodynamics*, M. J. Hemsch and J. N. Nielsen, Eds. New York: AIAA, 1986, vol. 104, pp. 297–379.

[54] ——, "Swept Shock/Boundary-Layer Interactions- Tutorial and Update," AIAA Paper 90–0375, 1990.

[55] D. S. Dolling, "Comparison of Sharp and Blunt Fin-Induced Shock Wave/Turbulent Boundary-Layer Interaction," *AIAA Journal*, vol. 20, no. 10, pp. 1385–1391, 1982.

[56] G. E. Gadd, "Interactions Between Shock Waves and Boundary Layers," in *Proceedings of the IUTAM Symposium on Boundary Layer Research*, H. Görtler, Ed. Berlin: Springer, 1958, pp. 238–255.

[57] A. McCabe, "The Three-Dimensional Interaction of a Shock Wave with a Turbulent Boundary Layer," *Aeronautical Quarterly*, vol. 17, pp. 231–252, 1966.

[58] R. H. Korkegi, "A Simple Correlation for Incipient-Turbulent Boundary-Layer Separation due to a Skewed Shock Wave," *AIAA Journal*, vol. 11, no. 11, pp. 1578–1579, 1973.

[59] B. W. Lowrie, "Cross-Flows Produced by the Interaction of a Swept Shock Wave with a Turbulent Boundary Layer," Ph.D. dissertation, Cambridge University, 1965.

[60] F. K. Lu, G. S. Settles, and C. C. Horstman, "Mach Number Effects on Conical Surface Features of Swept Shock Boundary-Layer Interactions," *AIAA Journal*, vol. 28, no. 1, pp. 91–97, 1990.

[61] D. S. Miller and E. Redeker, "Three-Dimensional Flow Separation," in *Bumblebee Aerodynamics Panel, minutes of 48th meeting.* The Johns Hopkins University: Applied Physics Lab. Report APL-TG14-43, 1963, pp. 283–308.

[62] M. A. Zubin and N. A. Ostapenko, "Structure of Flow in the Separation Region Resulting from Interaction of a Normal Shock Wave with a Boundary Layer in a Corner," *Fluid Dynamics*, vol. 14, no. 3, pp. 365–371, 1979.

[63] G. S. Settles and H. Y. Teng, "Cylindrical and Conical Flow Regimes of Three-Dimensional Shock/Boundary-Layer Interactions," *AIAA Journal*, vol. 22, no. 2, pp. 194–200, 1984.

[64] A. A. Zheltovodov, "Regimes and Properties of Three-Dimensional Separation Flows Initiated by Skewed Compression Shocks," *Journal of Applied Mechanics and Technical Physics*, vol. 23, no. 3, pp. 413–418, 1982.

[65] T. J. Goldberg, "Three-Dimensional Separation for Interaction of Shock Waves with Turbulent Boundary-Layers," *AIAA Journal*, vol. 11, no. 11, pp. 1573–1575, 1973.

[66] D. S. Dolling and S. M. Bogdonoff, "Upstream Influence in Sharp Fin-Induced Shock Wave Turbulent Boundary-Layer Interaction," *AIAA Journal*, vol. 21, no. 1, pp. 143–145, 1983.

[67] D. S. Dolling and W. B. McClure, "Flowfield Scaling in Sharp Fin-Induced Shock Wave/Turbulent Boundary-Layer Interaction," *AIAA Journal*, vol. 23, no. 2, pp. 201–206, 1985.

[68] G. S. Settles and F. K. Lu, "Conical Similarity of Shock/Boundary-Layer Interactions Generated by Swept and Unswept Fins," *AIAA Journal*, vol. 23, no. 7, pp. 1021–1027, 1985.

[69] D. D. Knight, C. Horstman, S. Bogdonoff, and B. Shapey, "Structure of Supersonic Turbulent Flow Past a Sharp Fin," *AIAA Journal*, vol. 25, no. 10, pp. 1331–1337, 1987.

[70] R. L. Kimmel and S. M. Bogdonoff, "A Comparative Experimental Investigation of Shock/Turbulent Boundary Layer Interactions Produced by Three Shock Generators," AIAA Paper 87–1366, 1987.

[71] K. S. Kim and G. S. Settles, "Skin Friction Measurements by Laser Interferometry in Swept Shock Wave/Turbulent Boundary-Layer Interactions," AIAA Paper 88–0497, 1988.

[72] H. Kubota and J. L. Stollery, "An Experimental Study of the Interaction Between a Glancing Shock Wave and a Turbulent Boundary Layer," *Journal of Fluid Mechanics*, vol. 116, pp. 431–458, 1982.

[73] C. H. Law, "Three-Dimensional Shock Wave-Turbulent Boundary Layer Interactions at Mach 6," Aerospace Research Laboratories, Wright-Patterson Air Force Base, Ohio, ARL TR 75-0191, June 1975.

[74] A. A. Zheltovodov, A. Maksimov, and E. Schülein, "Development of Turbulent Separated Flows in the Vicinity of Swept Shock Waves," in *The Interactions of Complex 3-D Flows*, A. M. Kharitnov, Ed. USSR Academy of Sciences, Institute for Theoretical and Applied Mechanics, Novosobirsk, 1987, pp. 67–91.

[75] C. C. Horstman and C. M. Hung, "Computation of Three-Dimensional Turbulent Separated Flows at Supersonic Speeds," *AIAA Journal*, vol. 17, no. 11, pp. 1155–1156, 1979.

[76] C. C. Horstman, "Prediction of Secondary Separation in Shock Wave Boundary-Layer Interactions," *Computers and Fluids*, vol. 17, no. 4, pp. 611–614, 1989.

[77] D. D. Knight, "Numerical Simulation of a Three-Dimensional Shock Wave-Turbulent Boundary-layer Interaction Generated by a Sharp Fin at Mach 4," *Computing Systems in Engineering*, vol. 1, no. 2-4, pp. 391–399, 1990.

[78] A. G. Panaras, "Numerical Investigation of the High-Speed Conical Flow Past a Sharp Fin," *Journal of Fluid Mechanics*, vol. 236, pp. 607–633, 1992.

[79] D. D. Knight, D. Badekas, C. C. Horstman, B. Shapey, and G. S. Settles, "Quasiconical Flowfield Structure of the Three-Dimensional Sharp Fin Interaction," *AIAA Journal*, vol. 30, no. 12, pp. 2809–2816, 1992.

[80] F. S. Alvi and G. S. Settles, "A Physical Model of the Swept Shock Wave/Boundary-Layer Interaction Flowfield," AIAA Paper 1991–1768, 1991.

[81] A. G. Panaras and E. Stanewsky, "Numerical Study of Secondary Separation in Glancing Shock/Turbulent Boundary Layer Interactions," AIAA Paper 92–3666, 1992.

[82] J. R. Cooper and W. L. Hankey, "Flowfield Measurements in an Asymmetric Axial Corner at M = 12.5," *AIAA Journal*, vol. 12, no. 10, pp. 1353–1357, 1974.

[83] R. Korkegi, "On the Structure of Three-Dimensional Shock-Induced Separated Flow Regions," *AIAA Journal*, vol. 14, no. 5, pp. 597–600, 1976.

[84] G. Degrez and J. J. Ginoux, "Surface Phenomena in a Three-Dimensional Skewed Shock Wave/Laminar Boundary-Layer Interaction," *AIAA Journal*, vol. 22, no. 12, pp. 1764–1769, 1984.

[85] G. Degrez, "Numerical Solution of a 3D Skewed Shock Wave Laminar Boundary-Layer Interaction," in *Proceedings of the IIIrd International Boundary and Interior Layers Conference*, Dublin, 1984.

[86] ——, "Computation of a Three-Dimensional Skewed Shock Wave Laminar Boundary-Layer Interaction," AIAA Paper 85–1565, 1985.

[87] F. Thivet, D. D. Knight, A. A. Zheltovodov, and A. I. Maksimov, "Analysis of Observed and Computed Crossing-Shock-Wave/Turbulent-Boundary-Layer Interactions," *Aerospace Science and Technology*, vol. 6, pp. 3–17, 2002.

[88] D. J. Mee, R. J. Stalker, and J. L. Stollery, "Glancing Interactions Between Single and Intersecting Oblique Shock Waves and a Turbulent Boundary Layer," *Journal of Fluid Mechanics*, vol. 170, pp. 411–433, 1986.

[89] D. Gaitonde and D. D. Knight, "Numerical Investigation of Some Control Methods for 3-D Turbulent Interactions due to Sharp Fins," AIAA Paper 89–0360, 1989.

[90] P. F. Batcho, A. C. Ketchum, S. M. Bogdonoff, and M. Fernando, "Preliminary Investigation of the Interactions Caused by Crossing Shock Waves and a Turbulent Boundary Layer," AIAA Paper 89–0359, 1989.

[91] T. J. Garrison and G. S. Settles, "Interaction Strength and Model Geometry Effects on the Structure of Crossing-Shock Wave/Turbulent Boundary-Layer Interactions," AIAA Paper 93–0780, 1993.

[92] T. J. Garrison, G. S. Settles, N. Narayanswami, and D. D. Knight, "Structure of Crossing Shock-Wave/Turbulent Boundary-Layer Interactions," *AIAA Journal*, vol. 31, no. 12, pp. 2204–2211, 1993.

[93] ——, "Laser Interferometer Skin-Friction Measurements of Crossing Shock-Wave/Turbulent Boundary-Layer Interactions," *AIAA Journal*, vol. 32, no. 6, pp. 1234–1241, 1994.

[94] ——, "Flowfield Surveys and Computations of a Crossing Shock Wave/ Boundary-Layer Interaction," *AIAA Journal*, vol. 34, no. 1, pp. 50–56, 1996.

[95] C. J. Chapman, *High Speed Flow*. New York: Cambridge University Press, 2000, ch. 11.

[96] A. A. Zheltovodov, A. Maksimov, and A. M. Shevchenko, "Topology of Three-Dimensional Separation Under the Conditions of Symmetric Interaction of Crossing Shocks and Expansion Waves with Turbulent Boundary Layer," *Thermophysics and Aeromechanics*, vol. 5, no. 3, pp. 293–312, 1998.

[97] A. A. Zheltovodov, A. Maksimov, A. M. Shevchenko, and D. D. Knight, "Topology of Three-Dimensional Separation Under the Conditions of Asymmetrical Interaction of Crossing Shocks and Expansion Waves with Turbulent Boundary Layer," *Thermophysics and Aeromechanics*, vol. 5, no. 4, pp. 483–503, 1998.

[98] D. D. Knight, T. Garrison, G. Settles, A. A. Zheltovodov, A. Maksimov, A. M. Shevchenko, and Vorontsov, "Asymmetric Crossing-Shock-Wave/Turbulent-Boundary-Layer Interaction," *AIAA Journal*, vol. 33, no. 12, pp. 2241–2249, 1995.

[99] A. A. Zheltovodov, A. I. Maksimov, E. Schülein, D. Gaitonde, and J. D. Schmisseur, "Verification of Crossing-Shock-Wave/ Boundary Layer Interaction Computations with the k–ϵ Turbulence Model," in *Proceedings of International Conference on the Methods of Aerophysical Research, Part I*, 2000, pp. 231–241.

[100] A. Salin, Y. Yao, and A. A. Zheltovodov, "Comparison and Improvement of Wall Heat Transfer Prediction in Crossing-Shock-Wave/Turbulent-Boundary-Layer Interaction Conditions," AIAA Paper 2013–0666, 2013.

[101] V. A. Bhagwandin, "Numerical Prediction of Shock-Boundary Layer Interaction Between a Pair of Fins in Hypersonic Flow," AIAA Paper 2014–3337, 2014.

[102] D. Knight, H. Yan, A. G. Panaras, and A. Zheltovodov, "Advances in CFD Prediction of Shock Wave Turbulent Boundary Layer Interactions," *Progress in Aerospace Sciences*, vol. 39, pp. 121–184, 2003.

[103] M. E. Zuber, W. Dieudonne, and J. M. Charbonnier, "Flowfield Structure for Crossing Shocks Intersecting a Mach 6 Laminar Boundary Layer," AIAA Paper 2000–4515, 2000.

[104] A. A. Sfeir, "Supersonic Laminar Boundary-layer Separation Near a Compression Corner." Berkeley: Dissertation, University of California, 1969.

[105] P. Colella and P. Woodward, "The Piecewise Parabolic Method (PPM) for Gas-Dynamical Simulations," *Journal of Computational Physics*, vol. 54, no. 1, pp. 174–201, 1984.

[106] A. Harten, B. Engquist, S. Osher, and S. R. Chakravarthy, "Uniformly High Order Accuracy Essentially Non-Oscillatory Schemes III," *Journal of Computational Physics*, vol. 71, no. 2, pp. 231–303, 1987.

[107] X. D. Liu, S. Osher, and T. Chan, "Weighted Essentially Non-Oscillatory Schemes," *Journal of Computational Physics*, vol. 115, no. 1, pp. 200–212, 1994.

[108] C. J. Greenshields, H. G. Weller, L. Gasparini, and J. M. Reese, "Implementation of Semi-Discrete, Non-Staggered Central Schemes in a Collocated, Polyhedral, Finite Volume Framework, for High-Speed Viscous Flows," *International Journal for Numerical Methods in Fluids*, vol. 63, no. 1, pp. 1–21, 2010.

[109] A. Kurganov and E. Tadmor, "New High-Resolution Central Schemes for Nonlinear Conservation Laws and Convection–Diffusion Equations," *Journal of Computational Physics*, vol. 160, no. 1, pp. 241–282, 2001.

[110] H. Nessyahu and E. Tadmor, "Non-Oscillatory Central Differencing for Hyperbolic Conservation Laws," *Journal of Computational Physics*, vol. 87, no. 2, pp. 408–463, 1990.

[111] A. Kurganov, S. Noelle, and G. Petrova, "Semi-Discrete Central-Upwind Schemes for Hyperbolic Conservation Laws and Hamilton-Jacobi Equations," *SIAM Journal of Scientific Computing*, vol. 23, no. 3, pp. 707–740, 2001.

[112] H. G. Weller, G. Tabor, H. Jasak, and C. Fureby, "A Tensorial Approach to Computational Continuum Mechanics Using Object-Oriented Techniques," *Computers in Physics*, vol. 12, no. 6, pp. 620–631, 1998.

[113] J. C. Robinet, "Bifurcations in Shock-Wave/Laminar-Boundary-Layer Interactions: Global Instability Approach," *Journal of Fluid Mechanics*, vol. 579, pp. 85–112, 2007.

[114] C. Ariza, C. Casado, R. Q. Wang, E. Adams, and J. Marugan, "Comparative Evaluation of OpenFOAM and ANSYS Fluent for the Modeling of Annular Reactors," *Chemical Engineering and Technology*, vol. 41, no. 7, pp. 1473–1483, 2018.

[115] R. Kumar and A. Dewan, "Partially-Averaged Navier-Stokes Method for Turbulent Thermal Plume," *Heat and Mass Transfer*, vol. 51, pp. 1655–1667, 2015.

[116] J. V. Becker, "Results in Recent Hypersonic and Unsteady Flow Research at the Langley Aeronautical Laboratory," *Journal of Applied Physics*, vol. 21, no. 7, pp. 622–624, 1950.

[117] W. D. Hayes and R. F. Probstein, *Hypersonic Flow Theory.* New York: Academic Press, 1959.

[118] J. D. Anderson Jr., *Hypersonic and High-Temperature Gas Dynamics.* Reston, Virginia, USA: AIAA, 2006, p. 387.

[119] J. R. Grisham, B. H. Dennis, and F. K. Lu, "Incipient Separation in Laminar Ramp-Induced Shock-Wave/Boundary-Layer Interactions," *AIAA Journal*, vol. 56, no. 2, pp. 524–531, 2018.

[120] L. Howarth, "Concerning the Effect of Compressibility on Laminar Boundary Layers and their Separation," *Proceedings of the Royal Society of London. Series A, Mathematical and Physical Sciences*, vol. 194, no. 1036, pp. 16–42, 1948.

[121] F. K. Lu and G. S. Settles, "Upstream-Influence Scaling of Sharp Fin Interactions," *AIAA Journal*, vol. 29, no. 7, pp. 1180–1181, 1991.

[122] J. R. Debonis, W. L. Oberkampf, R. T. Wolf, P. D. Orkwis, M. G. Turner, H. Babinsky, and J. A. Benek, "Assessment of Computational Fluid Dynamics and Experimental Data for Shock Boundary-Layer Interactions," *AIAA Journal*, vol. 50, no. 4, pp. 891–903, 2012.

[123] B. Eisfeld, H. Barnewitz, W. Fritz, and F. Thiele, Eds., *Management and Minimisation of Uncertainties and Errors in Numerical Aerodynamics: Results of the German Collaborative Project MUNA*, ser. Notes on Numerical Fluid Mechanics and Multidisciplinary Design. Berlin: Springer, 2013, ch. 4.

[124] P. J. Roache, "Quantification of Uncertainty in Computational Fluid Dynamics," *Annual Review of Fluid Mechanics*, vol. 29, pp. 123–160, 1997.

[125] ——, "Perspective: A Method for Uniform Reporting of Grid Refinement Studies," *Journal of Fluids Engineering*, vol. 116, no. 3, pp. 405–413, 1994.

[126] L. F. Richardson and J. A. Gaunt, "The Deferred Approach to the Limit," *Philosophical Transactions of the Royal Society A*, vol. 226, pp. 299–361, 1927.

[127] W. L. Oberkampf and C. J. Roy, *Verification and Validation in Scientific Computing*. New York: Cambridge, 2010, ch. 8.

[128] L. C. Squire, "The Motion of a Thin Oil Sheet Under the Steady Boundary Layer on a Body," *Journal of Fluid Mechanics*, vol. 11, no. 2, p. 161–179, 1961.

[129] A. A. Zheltovodov and D. D. Knight, in *Shock Wave-Boundary-Layer Interactions*, H. Babinsky and J. K. Harvey, Eds. New York: Cambridge, 2011, ch. 5.

[130] J. Délery and J. P. Dussauge, "Some Physical Aspects of Shock Wave/Boundary-Layer Interactions," *Shock Waves*, vol. 19, pp. 453–468, 2009.

[131] J. M. Délery, "Physics of Vortical Flows," *Journal of Aircraft*, vol. 29, no. 5, pp. 856–876, 1992.

[132] J. Stollery and L. Bates, "Turbulent Hypersonic Viscous Interaction," *Journal of Fluid Mechanics*, vol. 63, no. 1, p. 145–156, 1974.

[133] L. F. Henderson, "Experiments on the Impingement of a Supersonic Jet on a Flat Plate," *Journal of Applied Mathematics and Physics*, vol. 17, pp. 553–569, 1966.

[134] P. J. Lamont and B. L. Hunt, "The Impingement of Underexpanded Axisymmetric Jets on Wedges," *Journal of Fluid Mechanics*, vol. 76, no. 2, pp. 307–336, 1976.

[135] L. F. Henderson, "The Three Shock Confluence on a Simple Wedge Intake," *Aeronautical Quarterly*, vol. 16, no. 1, pp. 42–54, 1965.

[136] J. J. Sebastian and F. K. Lu, "Upstream-Influence Scaling of Fin-Induced Laminar Shockwave/Boundary-Layer Interactions," *AIAA Journal*, vol. 59, no. 5, p. 1861–1864, 2021.

[137] ——, "Upstream-Influence Scaling of Fin-Generated Shockwave/Laminar Boundary-Layer Interactions," AIAA Paper 2020–3009, 2020.

[138] ——, "Free Interaction in Three-Dimensional, Laminar Shockwave/Boundary-Layer Interaction," AIAA Paper 2020-0490, 2021.

[139] G. Degrez, "Swept Shock Wave/Laminar Boundary-Layer Interactions, Experimental and Numerical Results," in *Special Course on Shock Wave/Boundary-Layer Interactions in Supersonic and Hypersonic Flows.* AGARD Report 792, August 1993.

[140] R. Legendre, "Lignes de courant d'un écoulement permanent: Décollement et séparation," *La Recherche Aérospatiale*, vol. 1977-6, pp. 327–335, 1977.

[141] J. J. Sebastian and F. K. Lu, "Quasiconical Free Interaction in Fin-Induced Shockwave/Laminar Boundary-Layer Interactions," AIAA Journal (Accepted), 2021.

BIOGRAPHICAL STATEMENT

Jiss J. Sebastian was born in Kerala, India, in 1990. He received his Bachelors degree in Mechanical Engineering from Mahatma Gandhi University, Kerala, India, in 2012, his Masters degree in Mechanical Engineering (Propulsion) from the University of Kerala, India in 2015 and Ph.D. degree in Aerospace Engineering from the University of Texas at Arlington in 2021. His current research interest is in the area of high-speed gas dynamics and shockwave/boundary-layer interactions. He is a student member of AIAA.